DYNAMICS OF MICROCAPSULES AND RED BLOOD CELLS IN TIME-DEPENDENT SHEAR FLOW

BY

MENGYE ZHAO

A thesis submitted to the

Graduate School—New Brunswick

Rutgers, The State University of New Jersey

in partial fulfillment of the requirements

for the degree of

Master of Science

Graduate Program in Mechanical and Aerospace Engineering

Written under the direction of

Professor Prosenjit Bagchi

and approved by

_____

_____

_____

New Brunswick, New Jersey

OCTOBER, 2011

ABSTRACT OF THE THESIS

Dynamics of Microcapsules and Red Blood Cells in Time-dependent Shear Flow

by

Mengye Zhao

Thesis Director: Professor Prosenjit Bagchi

This thesis presents a three-dimensional numerical study on the dynamics of deformable capsules in sinusoidally oscillating shear flow. For this study, we consider capsules of spherical and oblate spheroid resting shapes. For spherical resting shapes, we find identical deformation response during positive and negative vorticity. However, the deformation response becomes unequal and shows complex behavior for nonspherical resting shapes. The average elongation is higher in the retarding phase of the shear flow than in the accelerating phase. Primarily two types of dynamics are observed for nonspherical shapes: a clockwise/counter-clockwise swinging motion in response to the altering flow

direction that occurs at both high and low values of shear rate amplitudes, and a continuous/unidirectional tumbling motion that occurs at intermediate values. The unidirectional tumbling motion occurs despite the fact that the time-average vorticity is zero. Such a tumbling motion is accompanied by a continuous tank-treading motion of the membrane in the opposite direction. We obtain phase diagram that shows existence of two critical shear rates and two oscillation frequencies. The unidirectional tumbling motion occurs in the intermediate range, and the clockwise/counter-clockwise swinging motion occurs otherwise. We also find that the dynamics is highly sensitive to the initial condition. A swinging is generally observed when the capsule is released aligned with the extensional or compressional axis of the shear flow, and a tumbling is observed otherwise. These results suggest the possibility of chaotic behavior of cells in time-dependent flows. We provide explanations of such complex dynamics by analyzing the coupling between the shape and angular oscillation and the imposed flow oscillation.

Acknowledgements

This research is partly funded by National Science Foundation. Computational supports from the NSF-funded Teragrid resources at TACC and NCSA are acknowledged.

Table of Contents

List of Figures

Chapter 1

Introduction

1.1 Red Blood Cell: Structure and Geometry

Blood is a multiphase suspension that is primarily consist of microscopic cellular particles like red blood cells or erythrocytes, white blood cells or leukocytes, and platelets. The cells are suspended in a liquid called plasma which is mostly made of water and other submicron elements such as proteins, glucose, mineral ions, hormones and gas. The red blood cells or erythrocytes consititute the major pariticulate component of the blood which is $40-45\%$ by volume. The primary function of the red blood cells is to carry oxygen. The cells are filled with a liquid called hemoglobin which facilitates the transport of oxygen to the tissues. In absence of any external fluid flow and force, a normal healthy human red blood cell assumes a biconcave disk shape that is flattenned at the center (see Fig. 1.1). The physical dimensions of the cell are about 8μm in end-to-end length and about 2μm in thickness. The cell volume is about 94 μm^3, and the surface area is about $134\mu\text{m}^2$. The hemoglobin is enclosed by a *membrane* that is made of a lipid bilayer and a two-dimensional network of spectrin filaments [2,3]. The membrane is generally permeable to gas molecules to facillitate their diffusion in and out of

the cell. The membrane is also permeable to water molecules. The permeability to water is necessary to maintain the osmotic balance, and hence, the resting biconcave shape which is obtained under the normal tonicity condition of the human blood. The cell shape can change if the tonicity of the suspensind medium is changed. At a significantly reduced tonicity, the biconcave shape disappears, and a nearly spherical shape is attained. Under the osmolarity-induced swelling, the cell volume increases while the surface area remains constant.

The red blood cells are extremely deformable cells. The deformability arised due to the fluidic nature of the hemoglobin, and the elastic nature of the cell membrane. The hemoglobin and plasma behave as Newtonian fluids. For normal cells, the typical values of hemoglobin and plasma viscosities are 6 and 1.2 cP, respectively. The cell membrane exhibits a strong resistance against area dilatation, but a very week resistance against shear deformation. The cells flow in the blood in a highly deformed shape that rarely resembles the resting biconcave shape. The deformation occurs due to the hydrodynamic shear, cell-cell interaction, and cell-wall interaction. The extreme deformability allows the cells to squeeze without any damage through the blood vessels that are much smaller than the cell size.

1.2 Capsules and Vesicles

Understanding the behavior of red blood cells in flow is fundamental to understanding the complex motion of blood. On a continuum scale, the detailed

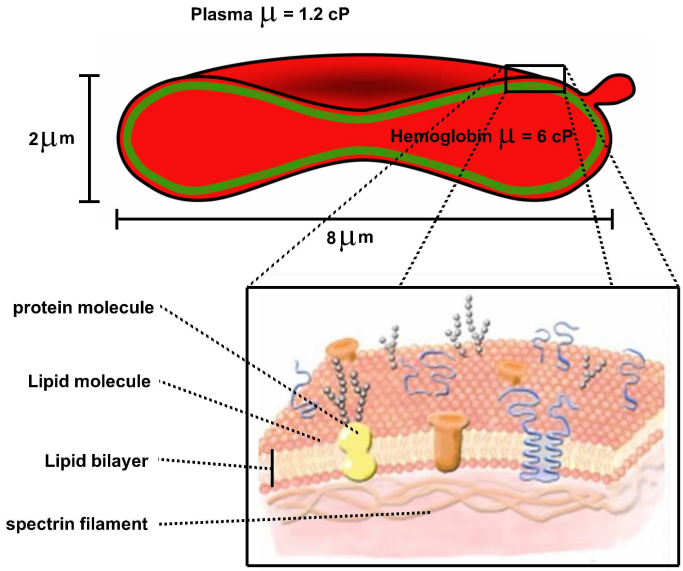

Figure 1.1: Schematic of an RBC showing its dimensions and the typical values of hemoglobin and plasma viscosities. Part of the RBC is magnified to show the lipid bilayer composition of the RBC membrane.

molecular structure of the cell membrane can be neglected. The entire cell is then modeled as a viscous liquid drop of Newtonian fluid surrounded by a zero-thickness elastic membrane. For the red blood cell, the mechanical properties of the membrane includes a resistance against shear deformation, area dilatation, and bending. The associated elastic modulus are 0.005 dyn/cm, 500 dyn/cm, and 10^{-12} dyn/cm. Due to the high value of the area dilatation modulus, the surface area of the red blood cell remains nearly constant while the cell can undergo a large deformation. In addition, the cell membrane, which is a 2D sheet of incompressible fluid, can also have a viscosity (hereafter, called membrane viscosity).

In vitro experiments often use alternative artificial microparticles called *capsules* and *vesicles* that are structurally similar to the red blood cells, and exhibit similar dynamics. Such microparticles are also highly deformable, but can be easily made in the laboratory. Artificial capsules and vesicles are also used as potential drug carriers. Some differences however exist between a red blood cell membrane and the membrane of a vesicle or capsule. A vesicle membrane behaves like a two-dimensional sheet of incompressible fluid. In other words, a vesicle membrane is strongly area preserving. In addition, the vesicle membrane also exhibits a resistance against bending, but no resistance against shear deformation. In contrast, a capsule membrane exhibits a resistance against shear deformation. It can be shown that the time scale of the deformation response associated with the shear deformation is much shorter than that associated with the bending resistance. Thus, the dynamics of the red blood cell is, in a major way, determined by the shear elasticity. Further, the resting shape of the artificially made capsules and vesicles usually are spherical or non-spherical, and do not have the biconcave shape of the red blood cells. Further, artificial capsules often do not exhibit a strong resistance against area dilatation and bending. Hence, in many theoretical and computational studies of capsules, often the resistance against area dilatation and bending has been neglected. The membrane viscosity of the artificial capsules have been rarely measured, and hence, also ignored in the theoretical models and computational studies. Nevertheless, these microparticles are also extremely deformable due to the fluidic nature of the inner liquid and elastic nature of the membrane, and hence, are widely used to model the red

blood cell behaviors in flow.

1.3 Dynamics of Red Blood Cells, Capsules and Vesicles in Steady Shear Flow

In a steady linear shear flow, an isolated red blood cell exhibits complex unsteady dynamics [4–9]. Primarily, a freely suspended red blood cell makes two types of dynamical motion: a tank-treading motion (TT) in which the cell membrane and the interior liquid make a rotational motion, while the cell aligns at an angle with the flow direction, and a tumbling motion (TU) that is characterized by the flipping of the cell resembling a rigid-body motion. These two types of motion are illustrated in Fig. 1.2. Qualitatively similar dynamics has been observed for capsules and vesicles as well [10–18]. A significant shape deformation may occur during either type of motion. For a given shape, the occurrence of the TT or TU motion depends on two parameters: λ, the ratio of the internal to suspending fluid viscosities, and $\dot{\gamma}$, the shear rate of the imposed flow. Qualitatively, the tank-treading motion is typically observed at high shear rates, and at low values of the interior to exterior fluid viscosity ratio. In contrast, the tumbling motion is observed at lower shear rates, and at higher values of the viscosity ratio.

1.4 Theory of Shape-preserving Cells

The tank-treading and tumbling dynamics can be predicted to some degree of accuracy by analytical models. One of the biggest foundation of such models is

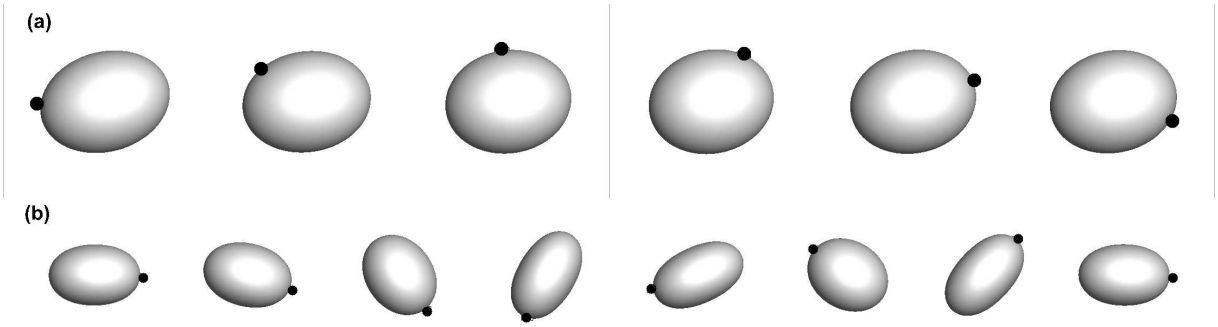

Figure 1.2: Schematic of tank-treading motion (a) and tumbling motion (b), represented by a marker surface point.

that they assume a shape-preserving cell. In other words, the deformation of the cell is neglected. These theories are based on the celebrated work of Keller and Skalak [19]. In the following section we briefly review some of these works starting with the theory of Keller and Skalak. It may be mentioned that inertia does not play any role in cell dynamics due to the small size.

1.4.1 Keller and Skalak model

The Keller-Skalak model assumes that a shape-preserving cell that is made of a viscous liquid drop surrounded by an in-extensible membrane. Since the membrane is inextensible, and the cell is non-deformable, the mechanical properties of the membrane does not appear in the problem. Then, the dynamics is entirely determined by the geometry of the cell which remains unchanged, the ratio of the internal to external fluid viscosity, and the shear rate of the imposed flow. Consider a neutrally buoyant ellipsoidal particle of half-major and minor axes lengths L and B, that is immersed in a linear shear flow $\mathbf{u} = \{\dot{\gamma}y, 0, 0\}$, where

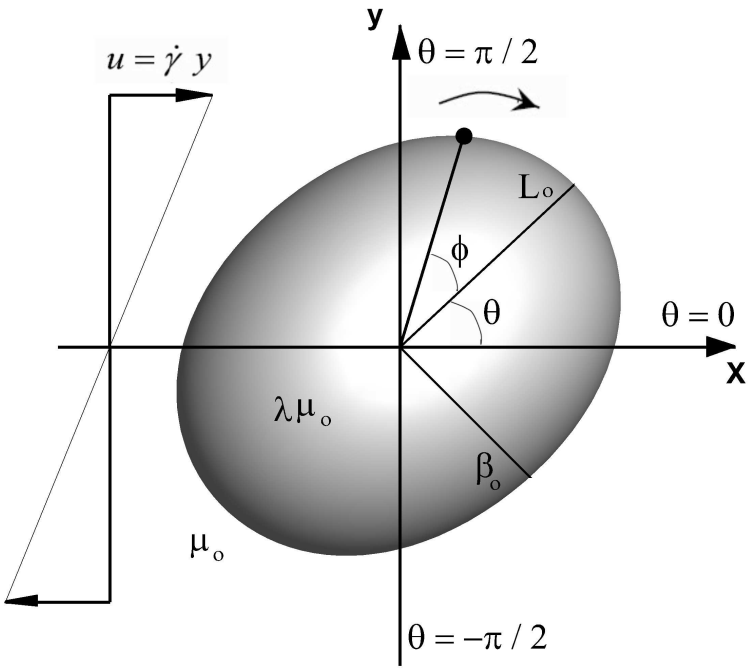

Figure 1.3: Schematic showing a capsule in shear flow. Here θ is the inclination angle of the major axis with the flow direction (x), and ϕ is the phase angle of a surface Lagrangian point. $0 < \theta < \pi/2$ is the extensional quadrant, and $-\pi/2 < \theta < 0$ is the compressional quadrant of the shear flow $\mathbf{u} = \{\dot{\gamma}y, 0, 0\}$.

$\dot{\gamma}$ is the shear rate [19]. The internal and suspending fluid to the particle are all assumed to be incompressible Newtonian fluid with viscosities $\lambda\mu_o$, and μ_o respectively (Fig. 1.3). The membrane is assumed to have zero viscosity. Under equilibrium condition, the net torque acting on the particle is zero. Further, the work done by the external fluid on the particle is equal to the energy dissipation in the internal fluid. These two conditions led to the following set of ordinary differential equations governing the particle dynamics within the Keller-Skalak model:

$$\dot{\theta} = -\frac{\dot{\gamma}}{2} - \frac{2LB}{L^2 + B^2}\dot{\phi} + \frac{\dot{\gamma}}{2}\frac{L^2 - B^2}{L^2 + B^2}\cos 2\theta\,, \tag{1.1}$$

$$\dot{\phi} = -\frac{\dot{\gamma} f_3}{f_2 - \lambda f_1}\cos 2\theta \tag{1.2}$$

where θ is the angle that the major axis of the ellipsoid makes with the flow direction x, ϕ is the angular location of a point on the particle surface, and f_1, f_2 and f_3 are dimensionless quantities, which depend on the particle geometry [19, 20]. The above system of equations yields two possible solution. A steady solution (i.e. $\dot{\theta} = 0$) is obtained when the viscosity ratio λ is less than a critical value λ_c. Under the steady solution, the particle's major axis is inclined at a steady angle θ^* with the flow direction, while the particle surface and the interior fluid make a continuous rotation. Thus, the steady solution correspond to the

tank-treading motion. The rate of rotation of the particle surface, known as the tank-treading frequency, can be found directly from the expression of $\dot{\phi}$ above.

The second possibility is an unsteady solution in which θ changes continuously, and $\dot{\phi}$ oscillates, meaning that the particle flips constantly like a rigid body in flow. This solution corresponds to the tumbling dynamics, and occurs when the viscosity ratio is higher than the critical value. The rate of tumbling, and the instantaneous orientation of the particle can be found using the expression of $\dot{\theta}$ above.

The critical viscosity ratio λ_c for the transition between tank-treading and tumbling motion can be obtained by setting θ^* equals zero,

$$\lambda_c = \frac{1}{f_1}\left[f_2 - \frac{2f_3}{\frac{1}{2}\left(r_2 + \frac{1}{r_2}\right) - z_1}\right] \tag{1.3}$$

Despite its apparent success in predicting the tank-treading and tumbling dynamics, there are several limitations of the Keller-Skalak theory. First, as already mentioned before, the theory assumes a shape-preserving particle, while red blood cells, capsule and vesicles depart significantly from their resting shape under the action of the hydrodynamic shear. Further, the deformation could also be unsteady. While small deformation of capsules and vesicles has been addressed by the analytical theories [21–23], one needs to resort to the numerical simulations when large deformations are considered.

Second, the theory predicts that dynamics is independent of the imposed

shear rate. Recent experiments and full-scale computational simulations [8, 24] have shown that the dynamics is shear-rate dependent as well. Specifically, for a given shape and viscosity ratio, the tank-treading motion occurs at a shear rate above a critical shear rate, and the tumbling motion occurs below the critical shear rate. Very recently, analytical theories are being developed to account for the shear rate dependence dynamics.

Third, recent experiments, computer simulations, and theoretical works have demonstrated that in addition to the TT and TU motion, erythrocytes, capsules and vesicles can exhibit an unsteady swinging or oscillatory dynamics (TT/OS) that is characterized by a time-dependent variation of the inclination angle with the flow direction, but without a complete tumbling motion [8,14,15,18,20,24–27]. Experiments by Abkarian *et al.* carried out on a red blood cell (RBC) show that for high shear values, RBC exhibits a quasi-steady tank-treading motion. With the decrease in shear rate, the RBC inclination oscillates about a mean angle. With further decrease in the shear rate, the RBC begins to tumble which is a departure from the KS theory.

The shear dependent transition and the oscillatory behavior of the RBCs were modeled by Skotheim and Secomb (SS) [20] as an extension to the Keller-Skalak theory.

1.4.2 Skotheim and Secomb's model

Skotheim and Secomb's [20] theory seeks to predict the shear-rate dependence by introducing an additional elastic energy term of the form $E = E_o \sin^2 \phi$ into the equations 1.1 and 1.2. As a result, the conservation of energy requires the work done by the suspending liquid on the capsule is equal to the sum of the dissipation inside the capsule and the change in capsule membrane elastic energy. This leads to the following energy conservation equation

$$V\mu_0 \left(f_2 \partial_t \phi^2 + f_3 \dot{\gamma} \partial_t \phi \cos 2\theta \right) = V\mu f_1 \partial_t \phi^2 + E_0 \sin(2\phi) \partial_t \phi \tag{1.4}$$

Solving for $\dot{\phi}$ gives the following modified form of equation 1.2

$$\dot{\phi} = \frac{f_3 \dot{\gamma}}{(f_2 - \lambda f_1)} \left(U_e \sin 2\phi - \cos 2\theta \right) \tag{1.5}$$

where, $U_e = E_o / V\mu_o \dot{\gamma} f_3$, and V is the volume of the particle. U_e can be interpreted as the ratio of the change in the elastic energy to the work done by the external fluid during the rotation. It also denotes the stiffness of the capsule relative to the external shear flow. The dynamics is now dependent on the dimensionless value of U_e, and hence, on the shear rate and the *ad hoc* membrane elastic modulus E_o. There are several advantages of the SS model over the KS model. First, the SS model predicts the shear-rate dependent dynamics. Second,

it also predicts the swinging motion which often occurs for the red blood cell in the tank-treading mode. Third, additionally, the SS model predicts an intermittent dynamics which is characterized by a combination of the swinging motion and the tumbling motion. Experimental verification of the intermittent dynamics is rather scarce except the experimental work by Abkarian et al. [8] for isolated red blood cells. Despite its apparent success, however, the SS model still neglects shape deformation.

1.5 Analysis of Capsule Deformation

Deformation dynamics of single capsule has been a subject of investigation for several decades. Deformation of a capsule suspended in a shear flow was measured by Chang & Olbright (1993) [28]. Recently, Risso et al. (2006) [29] experimentally investigated single-file motion of artificial capsules flowing through narrow tubes. Barthes-Biesel and co-workers (Barthes-Biesel 1980; Barthes-Biesel & Rallison 1981; Barthes-Biesel & Sgaier 1985; Barthes-Biesel 1991) [21, 30–32] developed the theory of small deformation for a capsule suspended in a shear (or, a general linear) flow. Li et al. (1988) [33] computed axisymmetric large deformation of capsules in a pure straining flow, and Leyrat-Maurin & Barthes-Biesel (1994) [34] studied axisymmetric large deformation of a capsule during its passage through a hyperbolic constriction. Queguiner & Barthes-Biesel (1997) [35] studied the axisymmetric motion of capsules through cylindrical tubes. Pozrikidis (1995) [36] and Ramanujan & Pozrikidis (1998) [11] used boundary integral simulation to

consider large deformation of capsules in shear flow. Pozrikidis (2001) [37] and Kwak & Pozrikidis (2001) [38] have also studied the effect of membrane bending resistance on the deformation of a capsule suspended in shear flow and in axisymmetric straining flow. Effect of membrane viscosity on the dynamic response of a capsule was studied by Diaz et al. (2000, 2001) [39, 40]. Capsule deformation under various constitutive laws for the membrane material was studied by Barthes-Biesel et al. (2002) [41] and Lac et al. (2004) [42]. Effect of membrane pre-stress was studied by Lac & Barthes-Biesel (2005) [43]. Eggleton & Popel (1998) [44] studied the large deformation of red blood cell ghosts using immersed boundary method. They have used both the neo-Hookean and Evans-Skalak model to study the deformation of initially spherical and biconcave capsules in shear flow.

1.6 Dynamics of Capsules and Red Blood Cells in Unsteady Shear Flow

The tank-treading/swinging and tumbling dynamics of capsules and red blood cells in a *steady* shear flow have been a subject of intense research for many years. In contrast, the red blood cells in circulation are subject to an *unsteady* flow, and recoil of smaller arteries regulating local circulation [45]. There have been a few studies that address the effect of the pulsatile flow on the cell dynamics. Nakajima et al. [46] studied the red cell deformation response in a sinusoidally varying shear flow generated in a cone-and-plate viscometer. A major finding

of their experiment is that the deformation response is not identical during the accelerating and retarding phases of the shear flow; the deformation is higher during the retarding phase, and lower during the accelerating phase. Nakajima et al. [46] noted that such an unequal response was not due to the viscoelastic nature of the cell membrane, but probably due to the rheological property of the intracellular fluid and its interaction with the membrane. Using the Skotheim-Secomb model [20] for shape-preserving capsules, Kessler et al. [47] obtained analytical solutions for quasi-spherical shapes in time-dependent shear flow. Their analysis reveals a resonant behavior under harmonically varying shear rate: For some frequencies and phase, it is possible to observe a tumbling motion of the capsule, which otherwise would swing under a steady shear flow corresponding to the time-averaged shear rate. Using a similar model for shape-preserving capsules [8], and supported by experiments, Dupire et al. [1] showed that the red blood cells can present either a stable motion or a chaotic motion under a sinusoidally varying shear flow. A stable tumbling motion is observed for shear rate amplitudes less than the critical shear rate for the tank-treading-to-tumbling transition in a steady flow. For higher shear rate amplitudes, the cell swings when the instantaneous shear rate is greater than the critical shear rate, and tumbles when it is less. In this range, an unstable nonperiodic motion that is highly sensitive to the initial condition is predicted by the theory, and also observed in the experiments. Using a phenomenological model that included cell deformation and constructed within the general framework of the Keller-Skalak theory [19], Noguchi [48] found that at a low shear frequency the cell swings at a high or low shear amplitude; the

former is termed as a tank-treading (TT)-based swing while the latter is termed as a tumbling (TB)-based swing. At the intermediate shear amplitude, a non-periodic motionis predicted. At higher frequencies, multiple stable solutions are found that depend on the initial inclination.

1.7 Scope of the Thesis

As evident from the above discussion, the cells/capsules exhibit interesting and complex dynamics in time-dependent shear flow. However, several aspects of the cell dynamics were not addressed or considered in the above studies. The analytical models used by Kessler et al. [47] and Dupire et al. [1] are for shape-preserving cells (though local deformation is permitted), while the large deformation of cells and capsules are well known. The experimental work of Nakajima et al. [46] did not mention the swinging motion, while such a motion is always observed for red blood cells and nonspherical capsules in moderate values of shear rate and viscosity ratio [8, 18, 20, 24–26, 49]. The swinging motion is always accompanied with periodic shape oscillation, and the angular and shape oscillations are highly synchronized. A recent review by Finken et al. [50] finds that shape changes play a dominant role in capsule dynamics. It is not clear how this synchronized shape and angular oscillation is affected when the imposed shear flow also oscillates with time. It is not clear also if the cells would exhibit chaotic dynamics when they are allowed to deform.

The overall objective of this thesis is, therefore, to study cell/capsule dynamics in a sinusoidally oscillating shear flow in presence of deformation. While the real flow oscillation is expected to be more complex than a harmonic one, this study serves as the first step towards understanding the complex cell dynamics in more realistic unsteady environment. Towards that end, we use a previously-developed in-house immersed-boundary/front-tracking methodology to study unsteady three-dimensional cell dynamics in the oscillating shear flow. We address four sub-problems in the thesis as follows:

First, we consider the capsule dynamics in a zero-mean oscillating shear flow under the condition of identical internal and external fluid viscosity. We consider both the initially spherical and non-spherical capsule shapes. The majority of the thesis is devoted to this work.

Second, we briefly address the role of internal fluid viscosity for both initially spherical and oblate capsules.

Third, we study the dynamics in finite-mean oscillating shear flow for initially non-spherical capsules.

And, finally, the dynamics of red blood cells in a zero-mean oscillating shear is also briefly addressed.

The numerical method is outlined in the next chapter. Since the code development is not a part of this thesis, we present only the salient features. This is followed by the detail presentation and analysis of the computational results in Chapter 3. The summary and conclusion are presented in Chapter 4.

Chapter 2

Problem Description and Simulation Methodology

2.1 Background flow and capsule model

Three-dimensional numerical simulations using front-tracking methods [51] are considered for capsules immersed in a time-dependent shear flow, and undergoing large deformation. The problem setup is depicted in Fig. 2.1. The imposed flow is a zero-mean sinusoidally oscillating linear shear flow given by $\mathbf{u}^{\infty} = [y\dot{\gamma}(t), 0, 0]$, where $\dot{\gamma}(t)$ is the instantaneous shear rate specified as

$$\dot{\gamma}(t) = \dot{\gamma}_a \sin\left[2\pi \frac{t}{T_{sh}}\right] , \tag{2.1}$$

where $\dot{\gamma}_a$ is the shear rate amplitude and T_{sh} is the oscillation period. Flow direction changes at every $T_{sh}/2$ interval. We consider two different initial (resting) shapes of capsules: a spherical shape, and an oblate spheroid of initial aspect ratio $\alpha = B_0/L_0$ where B_0 and L_0 are the semi-minor and major axes of the spheroid. The axis of symmetry of the initial shape lies in the shear plane. The capsule

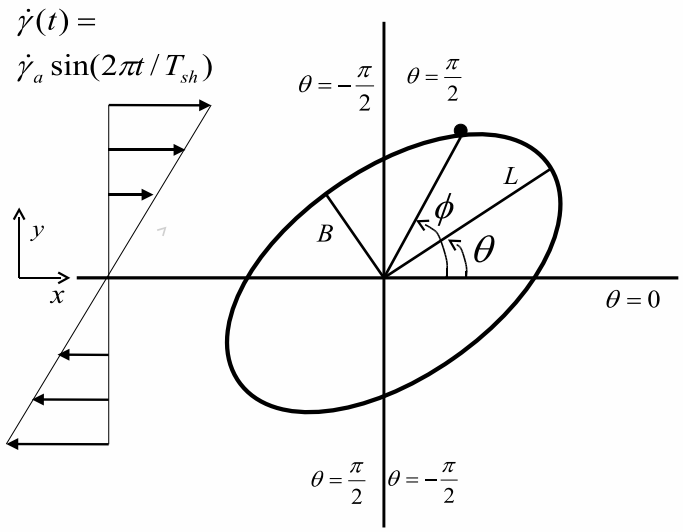

Figure 2.1: Schematic of a capsule in oscillating shear flow $\mathbf{u}^\infty = \{\dot{\gamma}y, 0, 0\}$, where $\dot{\gamma}(t) = \dot{\gamma}_a \sin(2\pi t/T_{sh})$ is the instantaneous shear rate, $\dot{\gamma}_a$ is the shear rate amplitude, and T_{sh} is the oscillation period.

is represented as a liquid drop surrounded by a zero-thickness elastic membrane. The interior and suspending fluids are assumed to be incompressible and Newtonian with viscosities $\lambda\mu_o$ and μ_o, respectively; here, λ is the viscosity ratio. The membrane is assumed to possess the resistance against shear deformation, area dilatation, and bending. The shear deformation and area dilatation are modeled using the strain energy function developed by Skalak et al. [52] as

$$W = \frac{E_s}{4}\left[(\epsilon_1^2 + \epsilon_2^2 - 2)^2 + 2(\epsilon_1^2 + \epsilon_2^2 - \epsilon_1^2\epsilon_2^2 - 1) + C\left(\epsilon_1^2\epsilon_2^2 - 1\right)^2\right] \tag{2.2}$$

where ϵ_1 and ϵ_2 are the principal stretch ratios, and E_s and $E_s(1 + 2C)$ are

the surface shear modulus, and the area dilatation modulus, respectively. The bending resistance is modeled using the Helfrich formulation [53] as

$$\mathbf{f}_b = E_b \left[(2\kappa + c_o) \left(2\kappa^2 - 2\kappa_g - c_o\kappa \right) + 2\,\Delta_s\,\kappa \right] \mathbf{n}\,, \tag{2.3}$$

where f_b is the force arising due to the bending resistance, E_b is the membrane bending modulus, κ is the mean curvature, κ_g is the Gaussian curvature, c_o is the spontaneous curvature of the membrane, $\mathbf{n}$ is the unit outward normal vector to the membrane, and Δ_s is the Laplace-Beltrami operator. We note that the constitutive law chosen for the in-plane elasticity is highly nonlinear, but that for the bending resistance is linear as Eq. (2.3) was derived by considering the first variation of the bending energy. Our choice of the Helfrich force is based on its earlier success in the study of vesicle dynamics, as well as its straightforward implementation within the framework of the front-tracking method. The Helfrich model has been used extensively to model bending resistance of vesicle membrane and in the study of complex (non-linear) vesicle dynamics (e.g., Danker et al. [22]) It is not known if the bilayer would behave differently in the present context.

2.2 Simulation Methodology

2.2.1 Fluid-sturcture interaction

For the multiple fluids with different properties considered for this problem, the simulation technique applied here is the front-tracking/immersed boundary method (Peskin *et al.* [54]; Unverdi & Tryggvason [55]; Tryggvason *et al.* [51]) The main idea of the front-tracking method is to use a single set of equations for both the internal and the suspending fluids of the capsule. The fluid equations are solved on a fixed Eulerian grid, and the interface is tracked in a Lagrangian manner by a set of marker points as shown in Fig. 2.2.

Since both the internal and the suspending fluid are considered to be imcompressible, the fluid motion interior and exterior to the capsule is governed by the continuity and Navier-Stokes equations

$$\nabla \cdot \mathbf{u} = 0\,, \tag{2.4}$$

$$\rho \left[\frac{\partial \mathbf{u}}{\partial t} + \mathbf{u} \cdot \nabla \mathbf{u} \right] = -\nabla p + \nabla \cdot \mu \left[\nabla \mathbf{u} + (\nabla \mathbf{u})^T \right] . \tag{2.5}$$

where $\mathbf{u}(\mathbf{x}, t)$ is the fluid velocity, ρ is density, p is pressure, and μ is the viscosity. Here $\mu(\mathbf{x}, t)$ is a single variable used to denote the viscosity of the entire fluid. Therefore, $\mu = \mu_c$ for the inner fluid and $\mu = \mu_0$ for the outer fluid

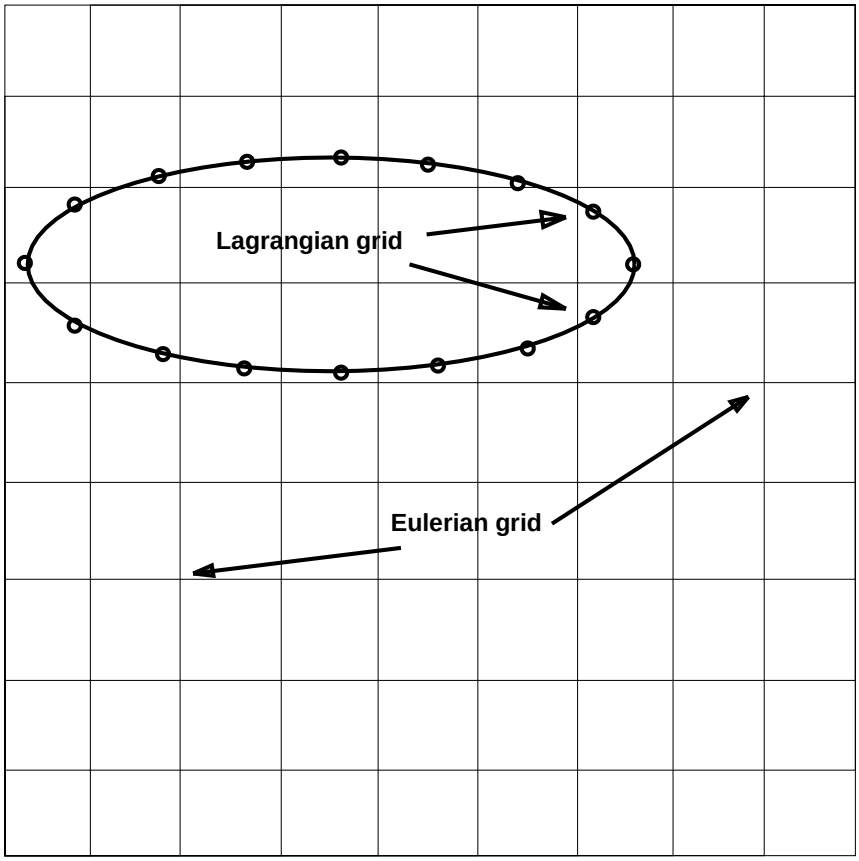

Figure 2.2: The Eulerian and Lagrangian grids

of the capsule. An indicator function $I(x)$ is mathematically defined which is unity inside the capsule and zero everywhere outside. Thus, μ is given by a single expression for every point in the fluid as

$$\mu(x) = \mu_0 + (\mu_c - \mu_0) I(\mathbf{x}). \tag{2.6}$$

The coupling between the membrane forces and the bulk flow is achieved by adding a source term $\int_S (\mathbf{f}_e + \mathbf{f}_b)\, \delta(\mathbf{x} - \mathbf{x}') d\mathbf{x}'$ to (2.5) where δ is the three-dimensional Dirac-Delta function, $\mathbf{f}_e$ is the membrane force due to shear deformation and area dilatation obtained from (2.2), $\mathbf{x}$ is a fixed (Eulerian) location in the flow, and $\mathbf{x}'$ is a Lagrangian location on the capsule surface S. The membrane is advected as $d\mathbf{x}/dt = \mathbf{u}_m$ where the membrane velocity $\mathbf{u}_m$ at a Lagrangian location is obtained by interpolating the local fluid velocity $\mathbf{u}$ using the Delta function. As a result, the membrane force varies smoothly over four Eulerian grid points surrounding the interface. For numerical implementation, the 3D δ function used in the source term is constructed by multiplying three 1D δ functions as

$$\begin{aligned} D(\mathbf{x} - \mathbf{x}') &= \frac{1}{64\,\Delta^3} \prod_{i=1}^{3} \left(1 + \cos \frac{\pi}{2\Delta}(x_i - x_i')\right) \quad \text{for} \quad |x_i - x_i'| \le 2\Delta, \quad i = 1, 2, 3, \\ D(\mathbf{x} - \mathbf{x}') &= 0 \qquad \text{otherwise,} \end{aligned} \tag{2.7}$$

where Δ is the Eulerian grid size (Unverdi & Tryggvason [55]).

2.2.2 Numerical treatment of membrane deformation

The capsule membrance govern by the constitutive law is described by a strain energy funcion W due to Skalak *et al.* . The elastic forces acting on the vertices of a triangular element is obtained from the strain energy function W using the principal of virtual work given as: $\mathbf{f}(\mathbf{x}', t) = -\partial W/\partial \mathbf{x}'$.

The elastic force $\mathbf{f}_e$ is computed using a finite-element method [56]. The membrae is discretized using 2D triangular elements. The major advantage of this idea is that it reduces a general 3D deformation of the membrane to a 2D problem by using the assumption that individual triangular element on the membrane remains flat during and after the deformation. The forces acting of the vertices of the element are therefore obtained by computing the displacements of the vertices of those deformed elements with respect to those undeformed elements.

The curvatures κ and κ_g are calculated by fitting a quadratic surface locally on the capsule surface, and using a least-square method to find the coefficients. Iterations are performed until a satisfactory convergence to the estimated normal vector is obtained. The curvatures are then found in terms of the fitted coefficients. By considering prescribed shapes, such as, spheres, spheroids, and biconcave discoids, we verified that the numerically estimated curvatures are satisfactory in comparison with their analytical counterparts. The computation of the Laplace-Beltrami operator on a triangulated surface follows the technique given in Reuter et al. [57].

2.2.3 Flow solver

The Navier-Stokes equations are solved on a fixed rectangular grid. A combined second-order finite difference scheme and Fourier transform is used for the spatial discretization, and a second-order time-split scheme is used for the temporal discretization of the Navier-Stokes equations. In this method, we split the momentum equation into an advection-diffusion equation and a Poisson equation for solving the pressure. The body-force term is included in the advection-diffusion equation. For numerical treatments, a second-order Adams-Bashforth scheme is used for the nonlinear terms, and a semi-implicit second-order Crank-Nicholson scheme is used for viscous terms. The resulting linear equations are inverted using ADI (alternating direction implicit) scheme to obtain a predicted velocity field. The pressure field of next time step is then obtained by solving the Poisson equation. Using the new pressure to correct the predicted velocity field, so that it satisfies the divergence-free condition.

2.2.4 Interface tracking

After obtained velocity and pressure fields by solving the Navier-Stokes equations, Lagrangian manner is used to track the capsule membrane. No-slip condition on the capsule surface is imposed by extracting the surface velocity from the suspending fluid at each time step as

$$\mathbf{u}_S(\mathbf{x}', t) = \int_S \mathbf{u}(\mathbf{x}, t)\delta(\mathbf{x} - \mathbf{x}')d\mathbf{x}, \tag{2.8}$$

where, S indicates the entire flow domain. Though the summation is over all fixed Eulerian nodes in the computational domain, only the 'local' nodes contribute to the membrane velocity. The discrete form of the delta function used here is the same as that given in equation 2.7. The Lagrangian points on the capsule membrane are then advected as

$$\frac{d\mathbf{x}'}{dt} = \mathbf{u}_S(\mathbf{x}', t). \tag{2.9}$$

Numerical treatment for the above equation is explicit second-order Adams-Bashforth scheme.

As the capsule moves and deforms, μ needs to be updated by solving a Poisson equation for the indicator function $I(x, t)$ as

$$\nabla^2 I = \nabla \cdot \mathbf{G}, \tag{2.10}$$

where, $\mathbf{G} = \int_S \delta(\mathbf{x} - \mathbf{x}')\mathbf{n}d\mathbf{x}$, and $\mathbf{n}$ is the unit vector normal to the capsule surface.

2.2.5 Dimensionless parameters

To cast the equations in dimensionless form, we use the radius a of the initial spherical shape (or, the radius of a sphere having the same volume of the spheroid) as the length scale, and the inverse shear rate amplitude $\dot{\gamma}_a^{-1}$ as the time scale. Then, the relevant dimensionless parameters are: the viscosity ratio

λ, the aspect ratio α, the capillary number $\mathrm{Ca} = \mu_o a\dot{\gamma}_a/E_s$, dimensionless period of flow oscillation $T^*_{sh} = \dot{\gamma}_a T_{sh}$, the dimensionless bending rigidity $E^*_b = E_b/a^2E_s$, and the parameter C associated with area dilation. We study capsule dynamics under varying α, Ca and T^*_{sh}, and keep λ, E^*_b, and C constant at 1, 0.01, and 1, respectively. The choice of $E^*_b = 0.01$ is based on the experimentally measured values for erythrocytes as $E_b = 1 - 9 \times 10^{-19}$ J [58–62], $E_s = 2 - 6$ μN/m [3, 63], and $a = 2.82$ μm [64]. However, unlike an erythrocyte membrane for which the surface is nearly incompressible, the capsule surface in the present case is allowed to dilate since we are using $C = 1$. Similar to many previous studies on vesicles of nonspherical shapes (e.g., [22]), we take the spontaneous curvature to be spatially-independent, as in the Helfrich formulation [53], and set it equal to $c_o = 0$, although it should be recognized that the reference curvature is space-dependent for the nonspherical resting shape. The Reynolds number $\mathrm{Re} = \rho a^2\dot{\gamma}_a/\mu_o = 0.01$. The flow domain is a cubic box of length $2\pi a$, and is periodic in the x and z directions, and wall-bounded in the y direction. We use 80^3 Eulerian points to discretize the box, and 5120 triangular elements to discretize the capsule surface.

2.3 Quantifying capsule dynamics

The capsule dynamics will be quantified in terms of the Taylor deformation parameter $D(t) = (L - B)/(L + B)$ where L and B are the instantaneous lengths of the major and minor axes in the shear plane, and the instantaneous angle $\theta(t)$

that the major axis makes with the positive x direction (Fig. 2.1). The numerical methodology has been presented in greater details and well tested in [65, 66] for capsules with neo-Hookean membranes without considering the bending rigidity. We have further verified that when using Skalak et al.'s formula, we obtain results that are in agreement with the previously published ones; for example, for initially spherical capsules with $C = 1$, and in absence of the bending rigidity, we get steady deformation $D = 0.186, 0.33, 0.42, 0.49$ at Ca = 0.1, 0.3, 0.6, and 1.2, respectively, which agree with the results of Lac et al. [42] and Li & Sarkar [67].

The tumbling and swinging motion will be identified here by the major axis inclination angle θ. As shown in Chapter 3, two types of dynamics are observed. In one case, the capsule makes clockwise and counter-clockwise swing in response to the altering flow directions, and θ remains bounded within 0 and 2π; such a motion is termed here as 'clockwise/counter-clockwise (CW/CCW) swing'. It can occur at high or low shear rates: Following Noguchi [48], the first one will be termed as the tank-treading (TT)-based swing as a material point on the capsule surface shows a significant oscillation (shown later in Fig. 3.10); the second one will be termed as the tumbling (TB)-based swing as a material point shows no significant oscillation. For other cases, the capsule makes a continuous and unidirectional rotating motion, so that θ continuously changes in only one direction beyond 2π. Such a motion is termed here as a 'continuous/unidirectional tumbling'.

Chapter 3

Dynamics of Microcapsules in Oscillating Shear Flow

3.1 Introduction

Before presenting the results on the capsule dynamics in oscillating shear flow, first we briefly present some salient results on the capsule dynamics in a steady linear shear flow as obtained from the present simulations. We consider two initial shapes: a spherical shape, and an oblate spheroid. At time $t^* = 0$, the capsule is released in the flow. It gradually deforms under the action of the hydrodynamic force, and eventually attains a steady or a quasi-steady dynamics. When the spherical initial shape is considered, the capsule deforms in to an obtale shape, and attains a steady deformation and an inclination angle with the flow direction. The steady shape of the capsule is shown in Fig. 3.1 for Ca = 0.05 and 1.0. In the former case deformation away from the initial spherical shape is evident, though not severe. In the latter case, severe deformation occurs, and the capsule attains highly oblate disc shape with high curvatures at the tips. The membrane and the interior fluid make a continous rotation. Thus, only a steady tank-treading motion is observed for the initially spherical shape. The

time history of the deformation response is also shown in the figure by plotting the instantansous Taylor deformation parameter D and the inclination angle θ. Clearly, the deformation increases with increasing capillary number. Note that when the steady state value of D versus Ca is considered, it appears that D reaches a saturation with increasing Ca. This is because the membrane is behaving as strain-hardening as we are using the constitutive law of Skalak et al. (Section. 2.2.2). Also note that the inclination angle decreases with increasing Ca as the capsule aligns more with the flow direction.

Next, we present some salient features of the dynamics of an initially nonspherical capsule. As discussed in the Introduction, there are primarily two types of motion that occur for a nonspherical capsule: an oscillatory motion combined with the tank-treading (usually, called the 'swinging' motion), and a tumbling motion. Significant deformation can exist in both modes. The former type of motion is observed for high capillary number, low viscosity ratio, and moderate oblate shapes. The latter type of motion is observed for low capillary number, high viscosity ratio, and highly nonspherical shapes. In this example we consider three cases for which λ is kept constant at 5, but Ca is varied as 0.1, 0.05 and 0.02. The capsule shapes at different time instants are shown in Fig. 3.2, and the instantaneous deformation D and inclination angle θ are shown in Fig. 3.3.

Consider first the $\mathrm{Ca} = 0.1$ case (Fig. 3.2a). For this, an oscillatory or swinging motion (TT/OS) is observed during which the capsule orientation varies periodically in time with the major axis remaining in the extensional quadrant of the

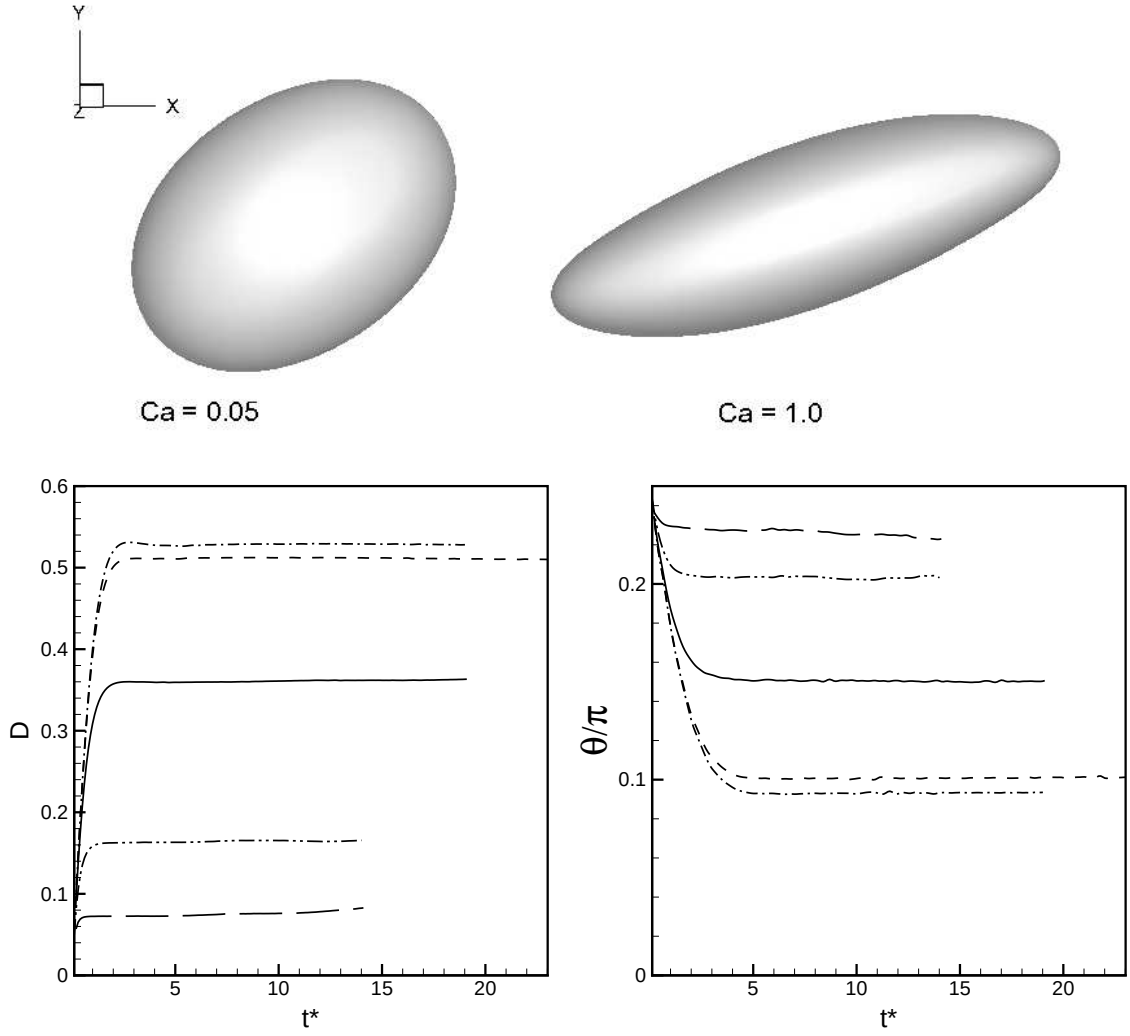

Figure 3.1: Dynamics of an initially spherical capsule in a steady shear flow. The steady shapes are shown for Ca = 0.05 and 1.0. The time history of the Taylor deformation parameter D and the inclination angle θ is shown for Ca = 0.02 (−− −− −−), 0.05 (− · ·−), 0.2 (——), 0.8 (- - - - -), 1.0 (-·-·-).

flow, while the membrane and the internal fluid make a tank-treading motion. As Fig. 3.3 shows, the inclination angle for this case oscillates in time between $\theta_{\min}$ and $\theta_{\max}$, but always remains positive. The oscillatory motion is accompanied by a periodic shape deformation, and as Fig. 3.3 shows, the deformation parameter D varies between $D_{\max}$ and $D_{\min}$ with $D_{\max} > D_0$ and $D_{\min} < D_0$, where $D_0 = D(t = 0)$. We also find that high tensile stresses develop in the membrane when $D > D_0$, and compressive stresses develop when $D < D_0$ (shown later). We do not observe membrane wrinkling within the span of our simulation ($t^* < 25$). Perhaps longer simulations will magnify such instabilities.

For Ca = 0.05 (Fig. 3.2b), a large amplitude swinging motion occurs during which θ periodically becomes positive and negative, but a full tumbling motion does not happen. A large-amplitude shape oscillation is present in this case in which the capsule instantly reaches a nearly circular shape in the shear plane, and hence, D momentarily approaches zero. A sharp increase in θ occurs while going from $\theta_{\min}$ to $\theta_{\max}$ due to the large shape oscillation (Fig. 3.3). We identify this case as a vacillating-breathing (VB) capsule. It appears that the amplitude of shape oscillation, defined as $D_{\max} - D_{\min}$, is the maximum for the VB motion.

For Ca = 0.02 (Fig. 3.2c), the tank-treading ceases, and a full tumbling motion (TU) is observed in which θ varies between $\pm\pi/2$. Even for this case, the deformation parameter D oscillates in time implying that a shape oscillation can co-exist with the tumbling motion. The time-averaged deformation decreases with decreasing Ca as evident from Fig. 3.3.

In summary, our numerical results suggest three types of unsteady dynamics: (i) an oscillatory motion (TT/OS) co-existing with the tank-treading motion at higher values of Ca, (ii) a vacillating-breathing motion (VB) at intermediate values of Ca for which the inclination angle periodically becomes positive and negative but a full tumbling does not happen, and (iii) a full tumbling motion at sufficiently lower values of Ca. Periodic shape oscillation co-exists in all cases, with the maximum shape oscillation occurring for the VB motion. The membrane stresses also vary periodically and are synchronized with the capsule elongation or compression. Similar observations are made when the transition triggered by increasing λ is considered: the TT/OS occurs at relatively low values of λ, followed by VB and TU motions at higher values.

3.2 Dynamics at Identical Internal and External Fluid Viscosity

First we present the results of capsules of initial spherical shape, followed by those of oblate spheroid shape. It should be mentioned that an initially spherical capsule, when subject to a steady shear flow, usually attains a steady deformed shape and inclination after an initial transience, while the membrane and interior fluid undergo a steady tank-treading motion. In contrast, a nonspherical capsule in a steady shear flow is observed to exhibit the swinging or tumbling motion with simultaneous periodic shape oscillation. A steady motion of a nonspherical capsule is often not observed.

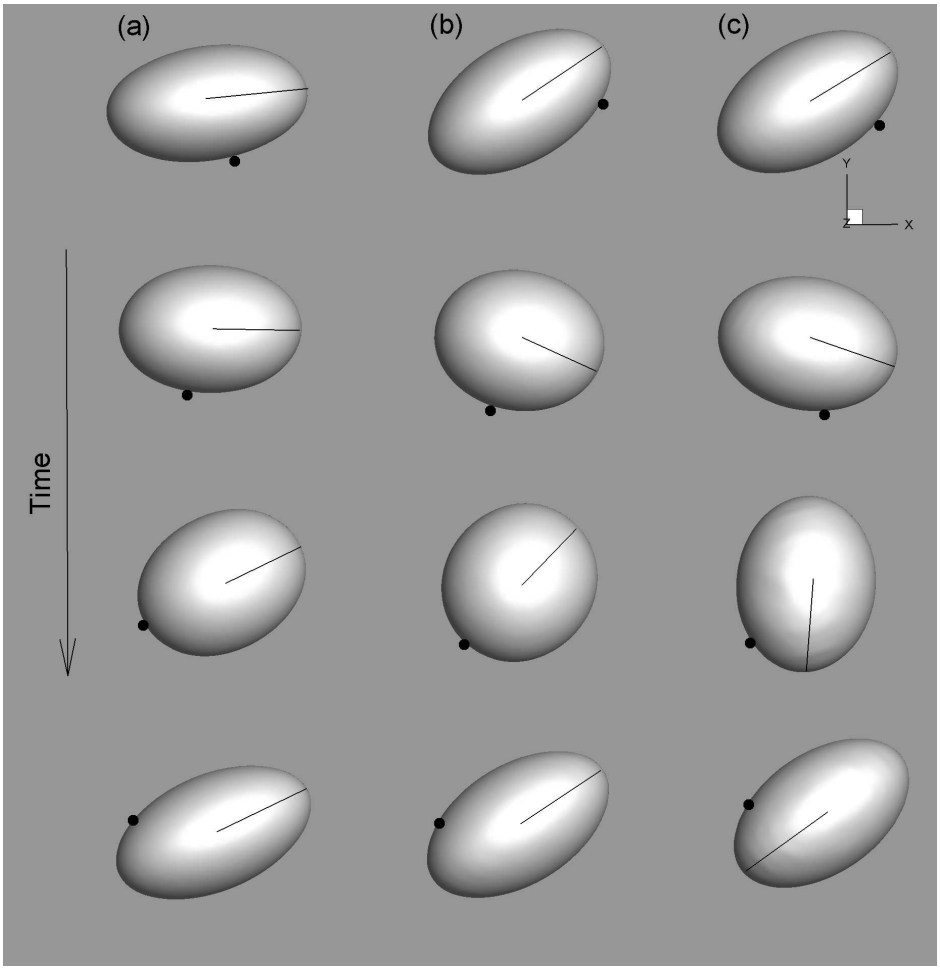

Figure 3.2: Transition from tank-treading/oscillatory (TT/OS) motion to vacillating-breathing motion (VB) to tumbling motion (TU) under varying capillary numbers at a constant $\lambda = 5$ and $\alpha = 0.7$: (a) TT/OS (Ca = 0.1), (b) VB (Ca = 0.05), and (c) TU (Ca = 0.02). Time increases from top to bottom. A marker point on the membrane is shown to illustrate the tank-treading. Time instants are $t^* = 12$, 14, 16, 18 in (a), $t^* = 8$, 13, 14, 16 in (b), and $t^* = 8$, 11, 13, 15 in (c).

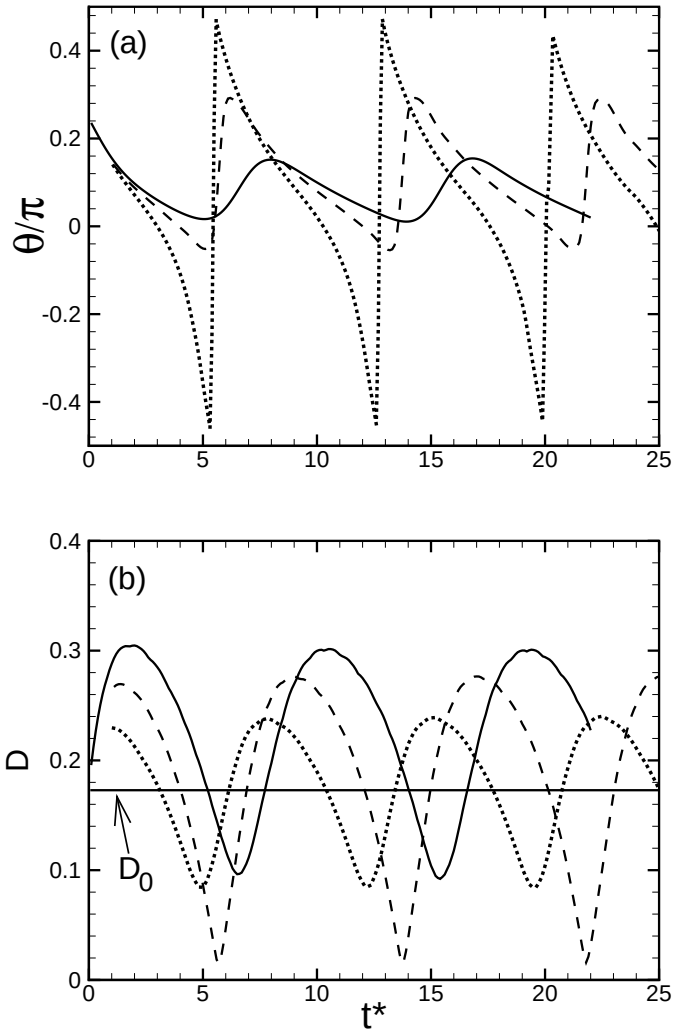

Figure 3.3: (a) Instantaneous orientation θ, and (b) deformation parameter D for the three cases shown in Fig. 3.2: Ca = 0.1 (solid line), 0.05 (dash line), 0.02 (dotted line) correspond to the tank-treading/oscillatory mode (TT/OS), vacillating-breathing mode (VB), and tumbling mode (TU), respectively. In (b) we indicate $D_0 = D(t = 0)$.

3.2.1 Spherical capsule

Fig. 3.4 describes the dynamics of an initially spherical capsule in an oscillating shear flow for Ca = 0.2 and $T^*_{sh} = 15$. The capsule undergoes a swinging motion between $\theta \approx \pm\pi/4$ in response to the sinusoidal shear. Periodic shape deformation accompanies the swinging motion. In any general shear flow, a capsule always seeks to align with the extensional quadrant. As a result,for $0 < t^* < T^*_{sh}/2$, the capsule aligns in the positive quadrant ($0 < \theta < \pi/2$). Elongation occurs during the accelerating phase ($0 < t^* < T^*_{sh}/4$), and the deformation approaches a maximum when $\dot{\gamma} \approx |\dot{\gamma}_a|$. Contraction occurs during the retardation phase, and the spherical shape is recovered at flow reversal ($t^* = T^*_{sh}/2$). After the flow reversal ($t^* > T^*_{sh}/2$), the capsule aligns in the negative quadrant ($-\pi/2 < \theta < 0$), and the elongation and contraction cycle is repeated.

The time-dependent deformation parameter $D(t)$ is shown in Fig. 3.4(b). It is important to note in the figure that the deformation response is identical during accelerating and retarding phases of the shear flow. The accelerating phase refers to the time window (e.g., $3T^*_{sh}/4 < t^* < 5T^*_{sh}/4$) during which $\dot{\gamma}$ changes from $-\dot{\gamma}_a$ to $\dot{\gamma}_a$, and the retarding phase refers to the time window (e.g., $T^*_{sh}/4 < t^* < 3T^*_{sh}/4$) during which $\dot{\gamma}$ changes from $\dot{\gamma}_a$ to $-\dot{\gamma}_a$. For the present case, we can compare the deformation responses during the positive and negative values of the vorticity. Note that the vorticity is negative during $0 < t^* < T^*_{sh}/2$, and positive during $T^*_{sh}/2 < t^* < T^*_{sh}$. From Fig. 3.4(b) we see that the deformation responses are identical during positive and negative vorticity. We have verified

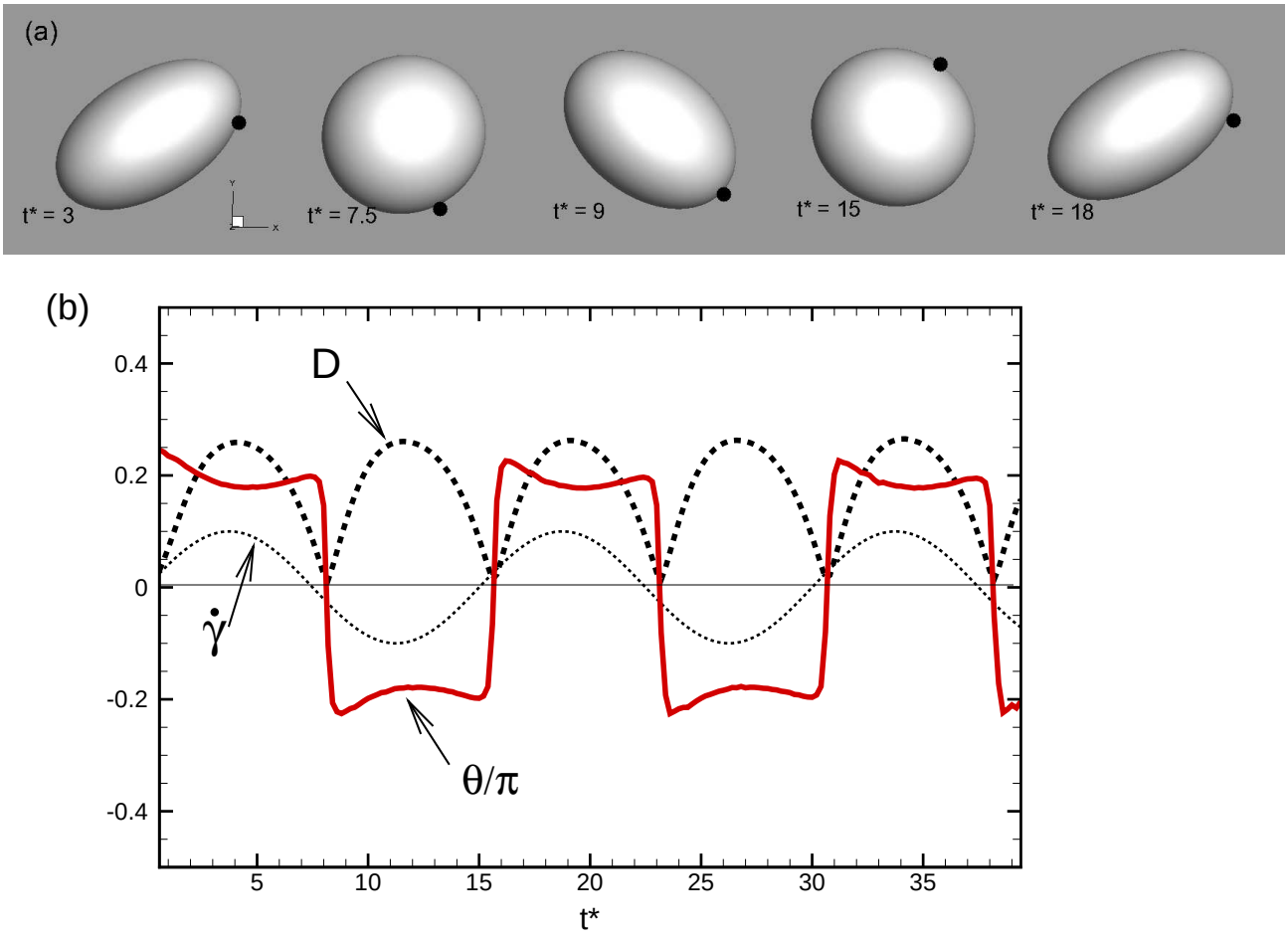

Figure 3.4: Color online. Dynamics of initially spherical capsules ($\alpha = 1$) in oscillating shear flow at Ca $= 0.2$, $T^*_{sh} = 15$. (a) Capsule shapes at successive times. A marker point on the surface is shown. (b) Instantaneous shear rate (in arbitrary scale), deformation parameter D, and angle θ for Ca $= 0.2$, $T^*_{sh} = 15$.

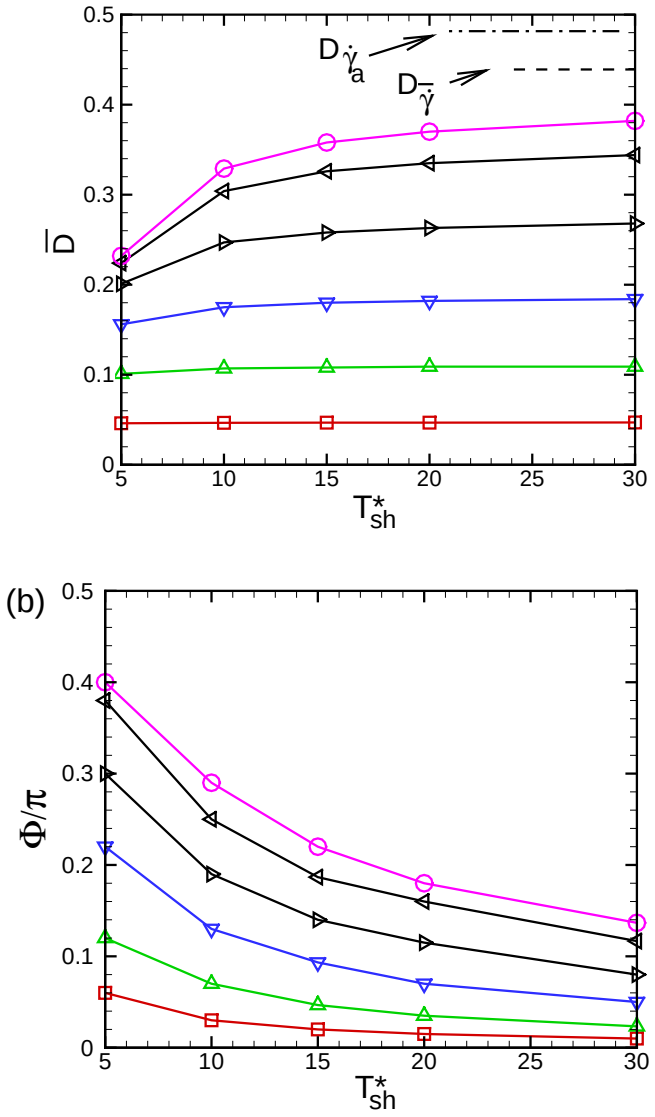

Figure 3.5: Color online. (a) Time-averaged deformation $\overline{D}$, and (b) phase-lag between deformation response and applied shear for initially spherical capsule as a function of T^*_{sh} for different values of Ca as 0.04($\square$), 0.1 (Δ), 0.2 (∇), 0.4 ($\triangleright$), 0.8 ($\triangleleft$), 1.2 ($\circ$). The dash-dotted line in (a) represents the deformation ($D_{\dot{\gamma}_a}$) in a steady shear flow for Ca $=\mu_o a\dot{\gamma}_a/E_s = 1.2$. The dashed line represents the deformation ($D_{\bar{\dot{\gamma}}}$) in a steady shear flow at $\overline{\text{Ca}} = \mu_o a\bar{\dot{\gamma}}/E_s = 2\text{Ca}/\pi$ where $\bar{\dot{\gamma}} = \int_0^{T_{sh}/2} \dot{\gamma}\mathrm{d}t/(T_{sh}/2) = 2\dot{\gamma}_a/\pi$.

that the identical deformation occurs for spherical capsules over a wide range: $0.04 \leq \text{Ca} \leq 1.2$, and $5 \leq T^*_{sh} \leq 30$. Hence, the results for spherical capsule differ from the experimental finding of Nakajima et al. [46] who observed unequal deformation response of the red blood cells. However, as we will show later, unequal deformation response is observed for nonspherical capsules. The role of shape oscillation becomes more important in case of nonspherical capsules, as will be seen later.

Fig. 3.5(a) shows the time-averaged deformation parameter $\overline{D} = \int_0^{T^*_{sh}} D \, \mathrm{d}t^* / T^*_{sh}$. For low values of Ca, the capsule responds fast, and hence $\overline{D}$ is independent of T^*_{sh} over the range considered. For higher Ca values, the response is slow. Hence $\overline{D}$ increases with increasing T^*_{sh} and approaches an asymptotic value for larger oscillating periods. As Fig. 3.5 shows, this asymptotic $\overline{D}$ is less than the deformation (indicated by $D_{\overline{\dot{\gamma}}}$ in Fig. 3.5(a)) that would occur in a steady shear flow corresponding to the mean shear rate $\overline{\dot{\gamma}} = \int_0^{T_{sh}/2} \dot{\gamma} \mathrm{d}t / (T_{sh}/2) = 2\dot{\gamma}_a/\pi$, and also less than the deformation (indicated by $D_{\dot{\gamma}_a}$ in Fig. 3.5(a)) that would occur in a steady shear flow corresponding to the shear rate amplitude $\dot{\gamma}_a$. Fig. 3.5(b) shows the phase-lag between the deformation response and the applied shear. At a given value of T^*_{sh}, the phase-lag increases with increasing Ca, since the response time increases. For a given Ca, the phase-lag also increases with increasing oscillating frequency since the capsule has less time to respond to the flow. This result is consistent with the prediction made by Noguchi [48].

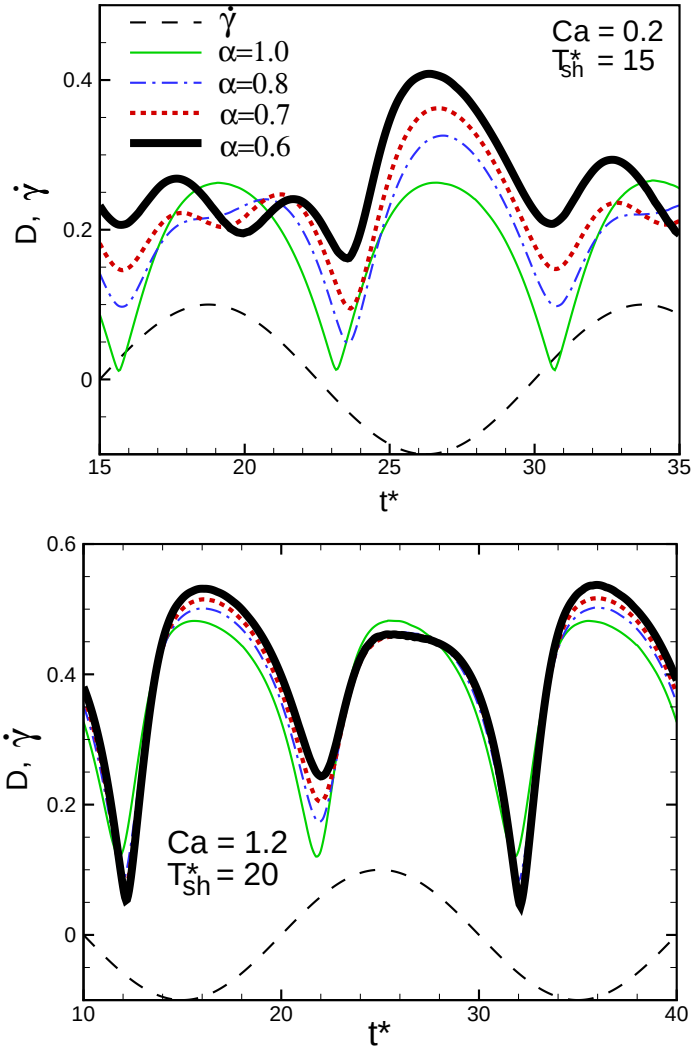

Figure 3.6: Color online. Effect of increasing non-sphericity on deformation response. The shear rate is shown in arbitrary scale.

3.2.2 Oblate spheroid

In time-dependent flows, one important parameter for the nonspherical capsules, unlike for the spherical capsules, is the initial inclination angle θ_o between the major axis and the positive x direction. First, we will study the effect of non-sphericity, capillary number and oscillating period while keeping $\theta_o = 0$ fixed. Later, we will consider the effect of θ_o. The effect of non-sphericity on the deformation response is shown in Fig. 3.6. Unlike the spherical capsules, the deformation responses of the nonspherical capsules are not identical during the positive and negative vorticity. Also, the deformation responses are not identical during the accelerating and retarding phases of the shear flow. The asymmetry in the deformation response increases with increasing non-sphericity (i.e., with decreasing α). The average deformation during the retarding phase is higher than that during the accelerating phase. Hence, our results agree qualitatively with the experimental results of Nakajima et al. [46] for non-spherical capsules. Since our model does not include membrane viscosity, the results suggest that the membrane viscosity is not essential to account for the unequal deformation response. However, based on our results it cannot be concluded if the asymmetry in deformation response increases or decreases with changing Ca and T^*_{sh} when α is kept constant (see also Fig. 3.11). Also interesting to note that for lower values of α and T^*_{sh} as in Fig. 3.6(a), unequal number of peaks of D are observed during positive and negative values of vorticity. Hence, the deformation response can be quite complex, and is due to the coupling between the imposed flow oscillation

and the natural swinging/tumbling of the capsule. In the following, we illustrate this coupling in greater details.

First we consider the effect of the capillary number on capsule dynamics which is shown in Fig. 3.7, 3.8, 3.9 where Ca is varied as 1.2, 0.2, and 0.04, respectively, while the oscillation period is held constant at $T^*_{sh} = 15$. As evidence in the figures, a CW/CCW swinging motion (see definition in Section. 2.3) occurs at Ca = 1.2 and 0.04 in which the capsule rotates both clockwise and counter-clockwise in response to the altering flow directions, but does not make a full 2π rotation. In contrast, a continuous/unidirectional tumbling motion occurs at Ca = 0.2. This result is remarkably different from that observed in a steady shear flow in which the tumbling motion would occur at Ca = 0.04 and swinging motion would occur at Ca = 0.2 and 1.2. Hence, unlike in a steady shear flow in which the tumbling motion occurs at low values of Ca and the swinging motion occurs at higher values, in an oscillating shear, a continuous/unidirectional tumbling motion is observed to appear in the intermediate values of Ca, and a CW/CCW swinging motion occurs at both high and low values of Ca. Further, the tumbling motion occurs continuously in the counter-clockwise direction for the case shown. This is also surprising since the time-averaged vorticity of the imposed shear flow is zero.

Several interesting features about the coupling between the shape and angular oscillation, and time-dependent shear-rate are revealed by examining D and θ as presented in Fig. 3.7, 3.8, 3.9. Consider Fig. 3.7 which corresponds to a swinging

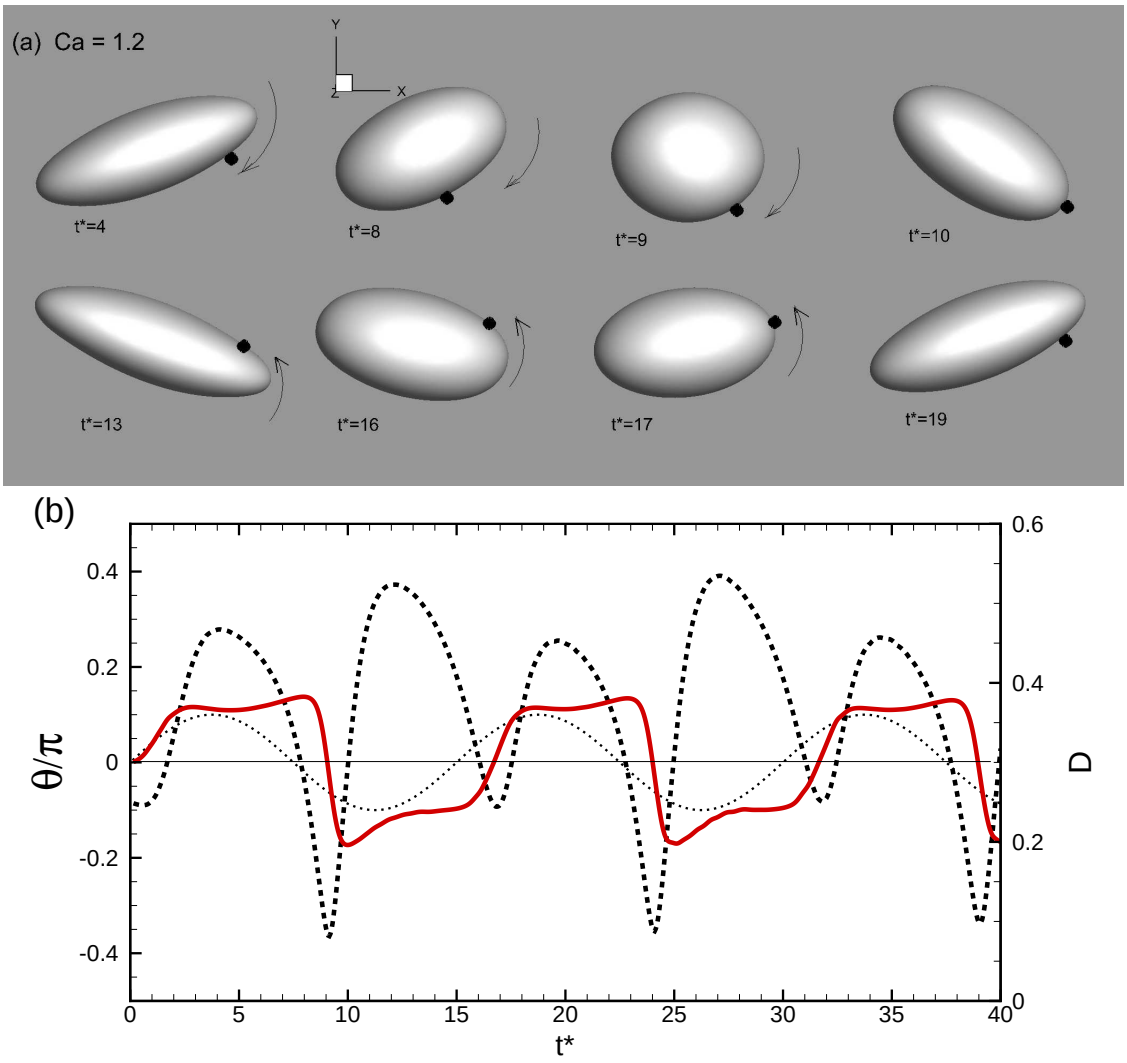

Figure 3.7: Color online. Effect of Ca on capsule dynamics. (a) Time-dependent snapshots. Arrows indicate the direction of capsule rotation. (b) Instantaneous inclination angle (θ/π, left scale, solid red line)and deformation parameter (D, right scale, dashed black line) for a capsule at Ca = 1.2. Other parameters are: $\dot{\gamma}_a T_{sh} = 15, \alpha = 0.6, \theta_o = 0, \lambda = 1$. The dotted line shows the instantaneous shear rate in arbitrary scale. A CW/CCW swinging motion (see definition in Section. 2.3) is observed here that is characterized by the capsule rotating both clockwise and counter-clockwise in response to the altering flow directions, without making a full 2π rotation.

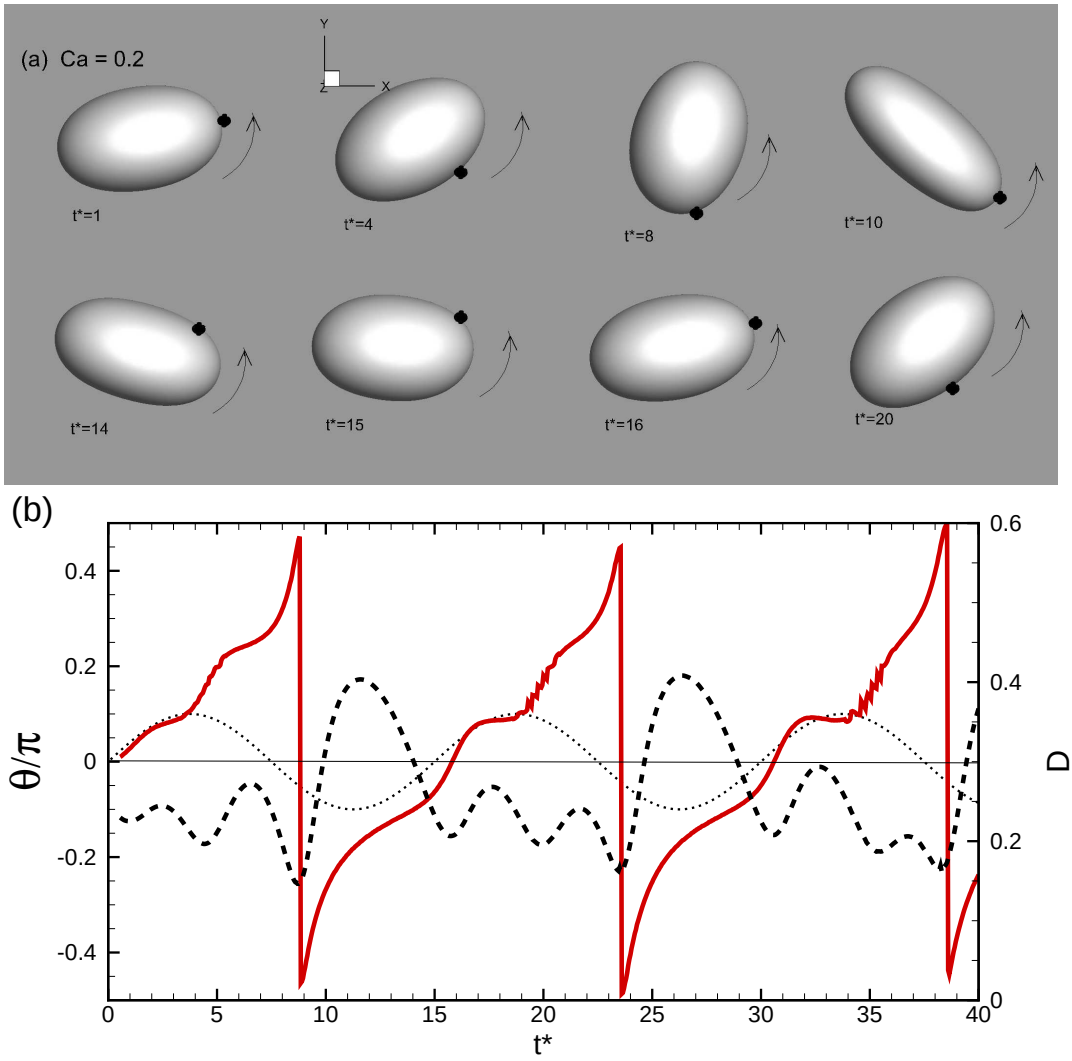

Figure 3.8: Color online. Same as in Fig. 3.7 except that Ca = 0.2. A continuous/unidirectional tumbling is observed here although the time-averaged vorticity is zero.

motion at Ca = 1.2. Between $t^* = 0$, and $T^*_{sh}/4$, the instantaneous shear rate increases, and D and θ increase continually till the shear rate becomes maximum. The inclination appears to attain a steady value as $\dot{\gamma} \longrightarrow \dot{\gamma}_a$. For $T^*_{sh}/4 < t^* < T^*_{sh}/2$, $\dot{\gamma}$ decreases, and hence D decreases but θ increases to its maximum value $\theta_{\max}/\pi = 0.25$. For $t^* < T^*_{sh}/2$, the capsule major axis remains in the positive quadrant ($0 < \theta < \pi/2$). The flow reversal occurs at $t^* = T^*_{sh}/2$, and the capsule orientation is now along the compressional quadrant of the reversed flow. For $3T^*_{sh}/8 < t^* < 5T^*_{sh}/8$, a rapid compression of the capsule occurs. For $t^* > 5T^*_{sh}/8$, an elongation starts in the negative quadrant $-\pi/2 < \theta < 0$ which is the extensional quadrant of the reversed flow. As $\dot{\gamma} \longrightarrow -\dot{\gamma}_a$, elongation of the capsule continues, and the inclination angle approaches a plateau in the negative quadrant at around $t^* = 7T^*_{sh}/8$. Another maximum in D is reached near $t^* \approx 3T^*_{sh}/4$. For $3T^*_{sh}/4 < t^* < T^*_{sh}$, capsule deformation decreases due to decreasing magnitude of the shear rate. The next flow reversal occurs at $t^* = T^*_{sh}$. For $T^*_{sh} < t^* < 9T^*_{sh}/8$, the capsule orientation is along the compressional quadrant of the shear which trigger the compression of the capsule during which it swings back to the positive quadrant($0 < \theta < \pi/2$).

For Ca = 0.04 in Fig. 3.9, the shape deformation is relatively small, and so the dynamics is similar to that of a rigid ellipsoid. The capsule swings clockwise for $0 < t^* < T^*_{sh}/2$, and counter-clockwise for $T^*_{sh}/2 < t^* < T^*_{sh}$, in accordance with the vorticity direction. For Ca = 0.2 in Fig. 3.8, a continuous/unidirectional (counter-clockwise) tumbling motion is observed. Between $0 < t^* < T^*_{sh}/4$, the

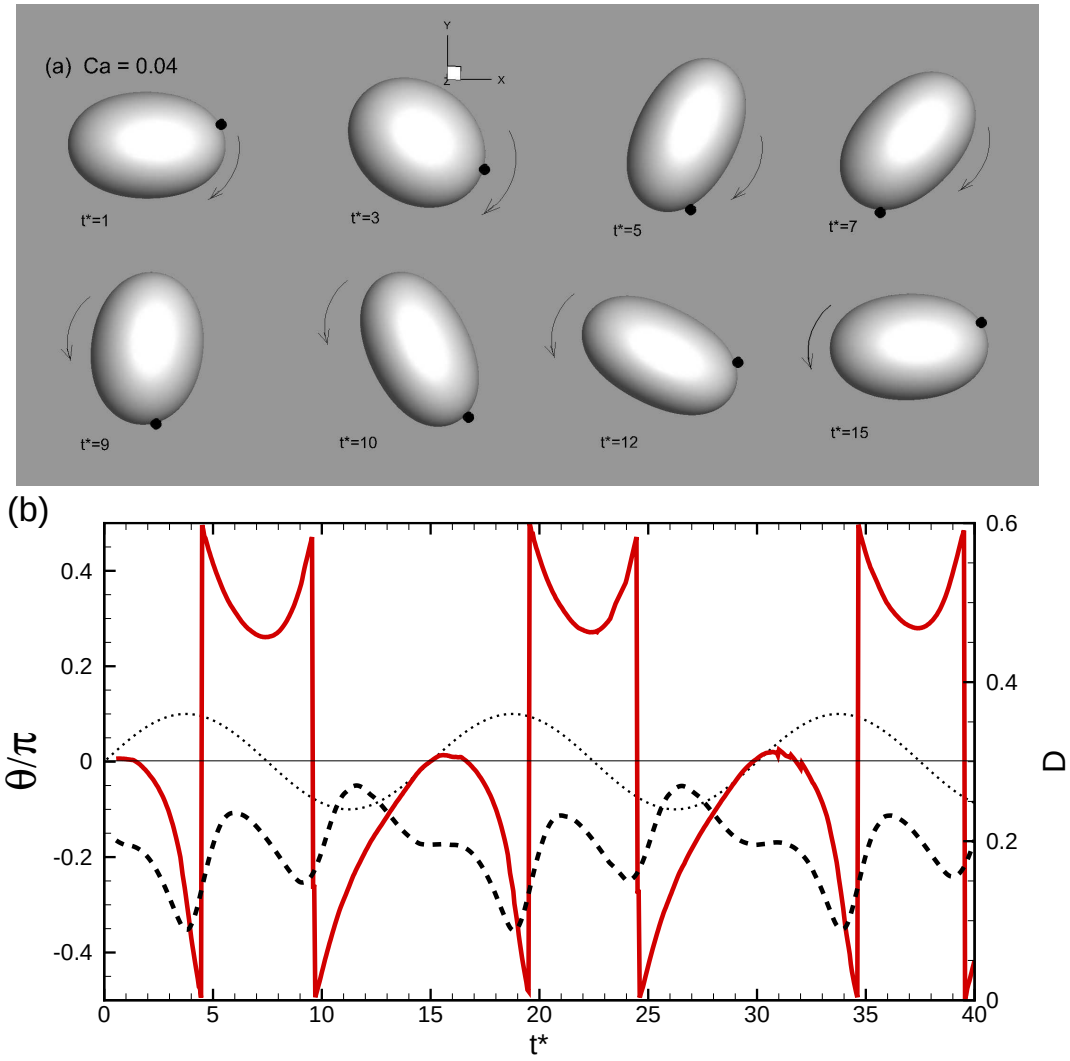

Figure 3.9: Color online. Same as in Fig. 3.7 except that Ca is reduced to 0.04. A CW/CCW swinging motion similar to that in Fig. 3.7 occurs here.

capsule elongates and rotates counter-clockwise as it tries to align with the extension direction of the shear flow. For $T^*_{sh}/4 < t^* < T^*_{sh}/2$, it slowly relaxes, while the inclination approaches $\pi/4$ as $\dot{\gamma} \longrightarrow 0$. This is because in the limit of small deformation, the inclination angle is $\pi/4$. The flow reversal occurs at $t^* = T^*_{sh}/2$. The reverse hydrodynamic torque then rotates the capsule counter-clockwise and in to the negative quadrant $-\pi/2 < \theta < 0$. The capsule continues to elongate, and the inclination angle decreases until the maximum shear rate is reached at $3T^*_{sh}/4$. For $3T^*_{sh}/4 < t^* < T^*_{sh}$, a shape contraction occurs due to decreasing $\dot{\gamma}$, and the capsule seeks to align with the compressional direction of the shear flow which causes further counter-clockwise rotation. The major axis aligns with the flow direction at $t^* \approx T^*_{sh}$ at which time the next flow reversal occurs, and the cycle is repeated. Some insight can be gained by following a Lagrangian marker point over time on the capsule surface as shown in Fig. 3.7, 3.8, 3.9. The phase angle of a marker point with respect to the capsule inclination angle ($\phi - \theta$, see Fig. 2.1) is plotted in Fig. 3.10. As seen in this figure, for Ca = 1.2, the phase angle oscillates with relatively large amplitude about a mean. In a steady shear flow at this value of Ca, the capsule would exhibit a tank-treading motion with the phase angle making a full 2π rotation while θ oscillates. In the oscillating shear flow, the phase angle can not make a full rotation due to faster change in the flow direction although a large oscillation of the phase angle occurs. This implies that a large relative motion between a material point on the capsule surface and any axis is occurring as in case of a tank-treading capsule in a steady shear flow. Following Noguchi [48], we further specify this dynamics as tank-treading

(TT)-based swing. In contrast, for Ca = 0.04, the oscillation of the phase angle is very small which implies that the capsule membrane is 'solidified' as in case of a tumbling capsule in a steady shear flow. Following Noguchi [48] again, we term this dynamics as tumbling (TB)-based swing. The dynamics at Ca = 0.04 and 1.2 is qualitatively similar to that predicted by Noguchi [48] at low and high shear amplitudes, respectively, at low shear frequency.

For intermediate capillary numbers (Ca = 0.1, 0.2, 0.4 as in Fig. 3.10), the phase angle decreases continuously. This is surprising, because a continuous change in the phase angle cannot occur in a tumbling motion in a steady shear. Hence, the characteristics of the tumbling motion seen in Fig. 3.8 in oscillating shear is different from that in a steady shear. Here, the membrane tank-treads continuously in the clockwise direction, while the capsule makes a continuous tumbling motion in the counter-clockwise direction.

The effect of the oscillation period T^*_{sh} is shown in Fig. 3.11 by varying T^*_{sh} as 5, 15, and 30, while the capillary number Ca is fixed at 0.2. Here also non-intuitive behavior is observed: a tank-treading-based swing occurs for high and low frequency oscillations (e.g., $T^*_{sh} = 5$ and 30 in the figure) in which the capsules rotate clockwise and counter-clockwise in response to the altering flow direction without making a full 360^o rotation. In contrast, a tumbling motion that is characterized by a continuous and unidirectional (counter-clockwise) rotation occurs for intermediate periods ($T^*_{sh} = 15$ in the figure).

In Fig. 3.12 we present the results from the analytical model of Dupire et

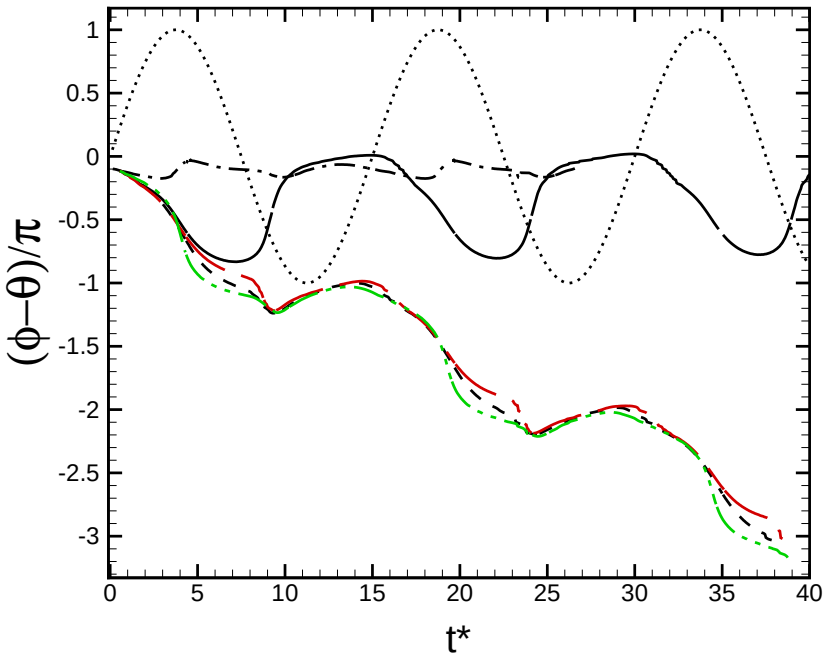

Figure 3.10: Color online. Angular location of a Lagrangian marker point on capsule surface relative to the capsule major axis inclination angle versus time. Here Ca is varied while $\alpha = 0.6$ and $T^*_{sh} = 15$ are held constant. $\cdots\cdots$ $\dot{\gamma}$; —— Ca = 1.2 (in black); – · – Ca = 0.04 (in black);— ·· — Ca = 0.1 (in green); - - - - Ca = 0.2 (in black); — — — Ca = 0.4 (in red).

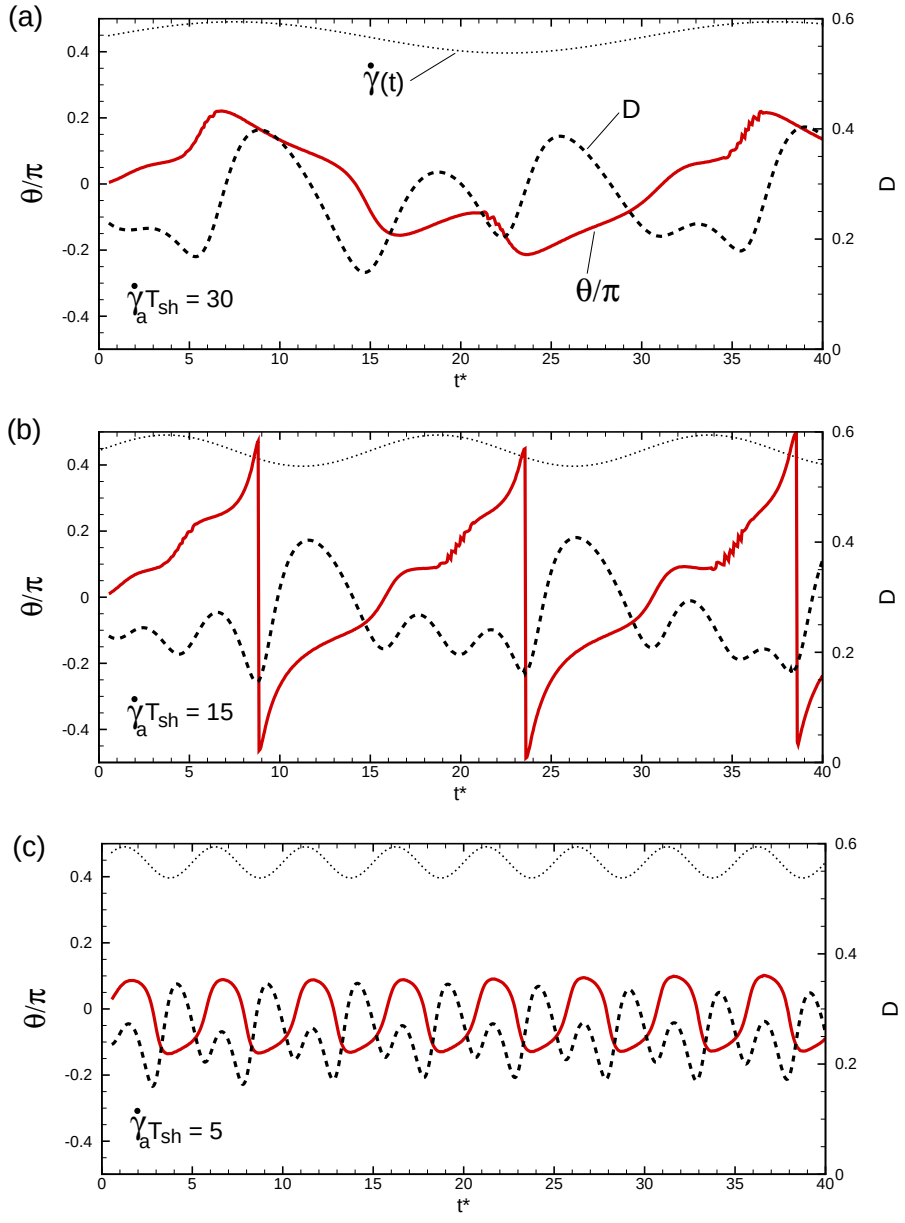

Figure 3.11: Color online. Effect of T_{sh} on capsule dynamics. $\dot{\gamma}_a T_{sh}$ is varied as 30, 15, and 5 in (a), (b), (c), respectively, while Ca is held constant at 0.2. A CW/CCW swing occurs in (a) and (c) which is characterized by the capsule oscillating both in clockwise and counter-clockwise directions without making a full 2π rotation. A tumbling motion occurs in (b) that is characterized by a continuous and unidirectional (counter-clockwise) rotation of the capsule and θ goes beyond 2π. Other parameters are: $\alpha = 0.6, \theta_o = 0, \lambda = 1$.—— θ/π (left scale, red line), - - - - - D (right scale, black line), ····· $\dot{\gamma}(t)$(arbitrary scale).

al. [1] for shape-preserving capsules. The capsule dynamics is described in terms of two coupled equations for the inclination angle θ and the Lagrangian angular location ω as

$$\frac{d\theta}{dt} = \dot{\gamma}_a \sin(2\pi t/T_{sh}) \left[-\frac{1}{2} + \frac{1}{2}\frac{1-\alpha^2}{1+\alpha^2}\cos(2\theta) \right] - \frac{2\alpha}{1+\alpha^2}\frac{d\omega}{dt} \tag{3.1}$$

$$\frac{d\omega}{dt} = \frac{\dot{\gamma}_a f_3}{f_2 - \lambda f_1} \left[\frac{f_1}{2f_3}\frac{1}{\widehat{\mathrm{Ca}}}\sin(2\omega) - \cos(2\theta) \right] \sin(2\pi t/T_{sh}) \tag{3.2}$$

where f_1, f_2 and f_3 are dimensionless functions of α, $\widehat{\mathrm{Ca}} = \mu_o \dot{\gamma}_a V/\eta\Omega$, V is the cell volume, Ω is the membrane volume, and η is membrane shear modulus. Here we have assumed that the membrane viscosity is zero, as in our numerical model. Using the values given in [1] ($\Omega/V = 7.48\times10^{-2}$, $\mu_o = 34\times10^{-3}$ Pa·s and $\eta = 1.6$ Pa) we get $\widehat{\mathrm{Ca}} \approx 28$ for $\dot{\gamma}_a = 100$ 1/s. We choose $\widehat{\mathrm{Ca}} = 0.1$, 1, and 100, and $T^*_{sh} = 5$, 15, 30. For $\widehat{\mathrm{Ca}} = 0.1$, only CW/CCW oscillation is observed for all three values of T^*_{sh}. This result is qualitatively similar to our conclusion that a periodic CW/CCW oscillation occurs at low shear rates (Fig. 3.9). For $\widehat{\mathrm{Ca}} = 1$ and 100, the model predicts different dynamics depending on T^*_{sh}. For $T^*_{sh} = 5$ and 30, the CW/CCW oscillationis predicted, which is in agreement with our conclusion that such an oscillatory motion occurs at high or low period as was seen in Fig. 3.11a and c. At an intermediate period, as $T^*_{sh} = 15$, the model predicts a nonperiodic motion in which tumbling and swinging occur intermittently. In contrast, our

simulation predicts only a continuous/unidirectional tumbling motion within the length of simulation; beyond $t^* \approx 100$, capsule shapes become distorted and the simulations are discontinued. Hence we are unable to confirm the nonperiodic behavior. It is possible that large deformation that occurs at high shear rates would prevent the nonperiodic motion [68].

We have simulated a large number of cases by varying Ca and T^*_{sh} to generate a phase diagram of swinging/tumbling dynamics in oscillating shear flow which is shown in Fig. 3.13. Clearly, the continuous/unidirectional tumbling motion (similar to Fig. 3.8) occurs for intermediate values of Ca and T^*_{sh}. The phase diagram suggests that at a fixed T^*_{sh}, there exists two critical capillary numbers Ca^u_{cr} and Ca^l_{cr}, and hence, two critical shear rate amplitudes, $\dot{\gamma}^u_{cr}$, and $\dot{\gamma}^l_{cr}$. The CW/CCW swinging motion (similar to Fig. 3.7 and 3.9) occurs for any capillary number above Ca^u_{cr} and belowCa^l_{cr}, and the continuous/unidirectional tumbling motion occurs in between. For $\mathrm{Ca} > \mathrm{Ca}^u_{cr}$, the swinging motion is TT-based [48] and accompanied by a significant back-and-forth oscillation of a membrane point. For $\mathrm{Ca} < \mathrm{Ca}^l_{cr}$, the swinging motion is TB-based [48], and a membrane point shows negligible oscillation. The existence of two critical shear rates in an oscillating shear flow is remarkable since in a steady shear the transition is determined by one critical shear rate. Fig. 3.13 also suggests that at a fixed value of Ca, there exists two critical oscillation periods T^{*u}_{sh} and T^{*l}_{sh}. The continuous/unidirectional tumbling motion occurs for $T^{*l}_{sh} < T^*_{sh} < T^{*u}_{sh}$, and the CW/CCW swinging motion occurs otherwise.

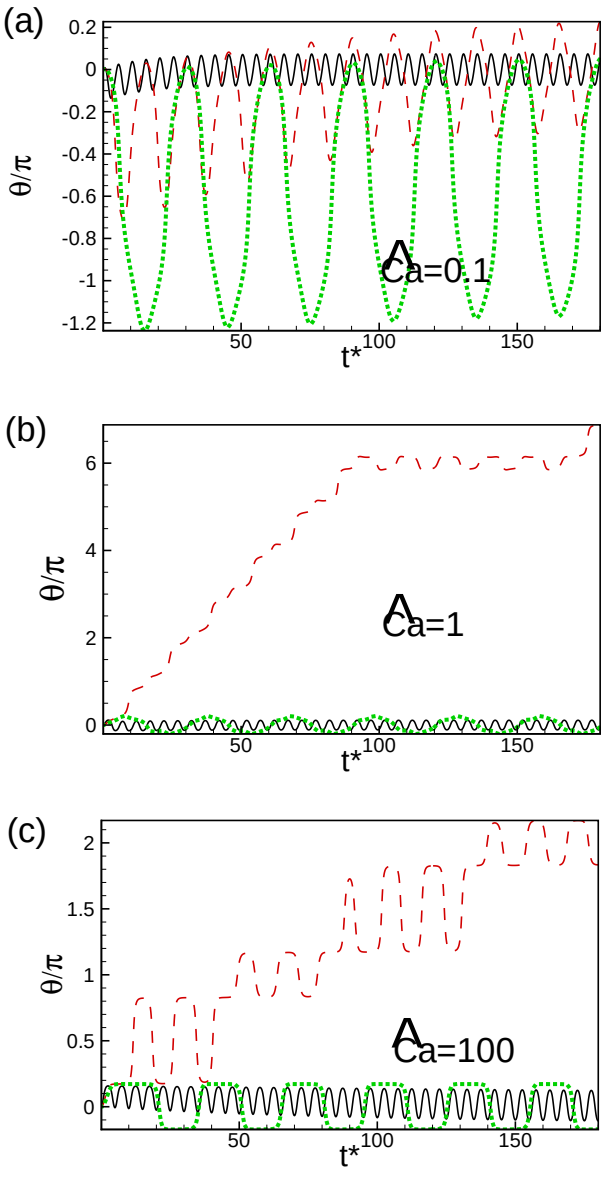

Figure 3.12: Color online. Results from the theory of shape-preserving capsules in oscillating shear flow [1] for $\alpha = 0.6$, and $\theta_o = 0$.(a), (b), and (c) are for $\widehat{\mathrm{Ca}} = \mu_o \dot{\gamma}_a V/\eta\Omega = 0.1, 1$ and 100, respectively. $T^*_{sh} = 5$ (black solid line), 15 (red dashed line), 30 (green dotted line).

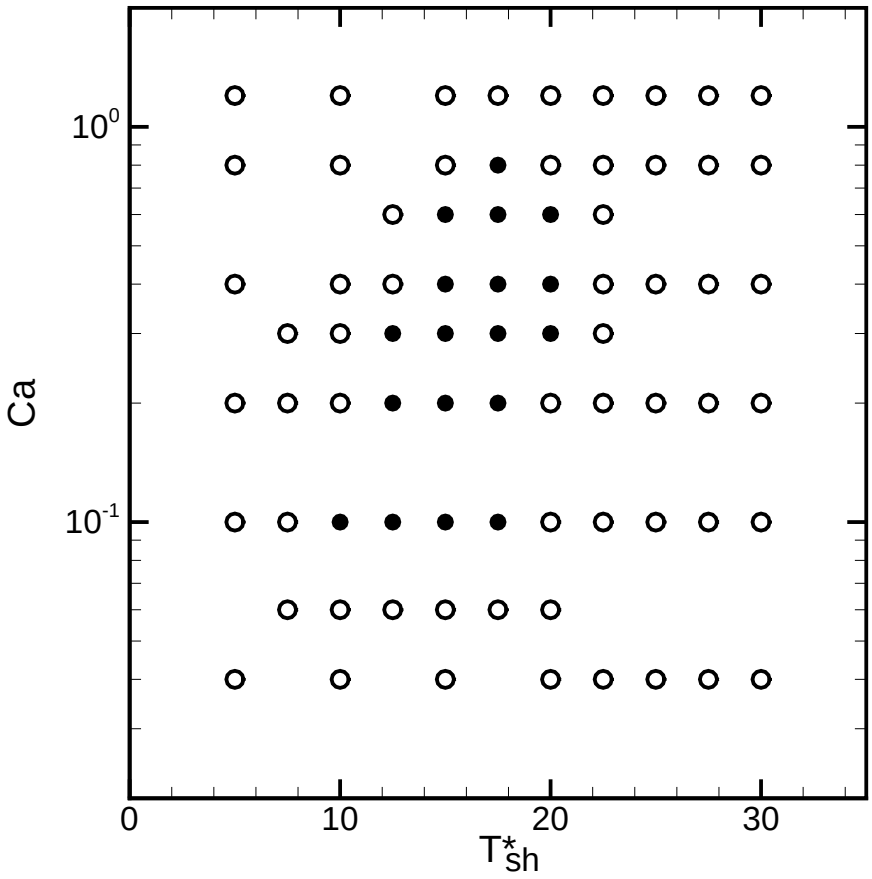

Figure 3.13: Phase diagram for $\alpha = 0.6$, $\theta_o = 0$. Open circles represent the CW/CCW swinging motion characterized by clockwise/counter-clockwise oscillation of the capsule without making a full 2π rotation (similar to Fig. 3.7 and 3.9), and filled circles represent a continuous/unidirectional tumbling motion(similar to Fig. 3.8).

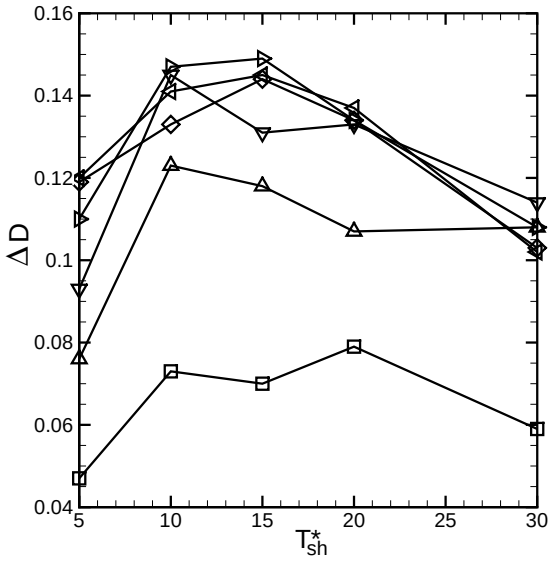

Figure 3.14: Amplitude of shape oscillation ΔD as a function of T^*_{sh} for different Ca.$\square$ Ca= 0.04; Δ Ca = 0.1; ∇ Ca = 0.2; $\triangleright$ Ca = 0.4; $\triangleleft$ Ca = 0.8; $\diamond$ Ca = 1.2.Here $\alpha = 0.6, \theta_o = 0$.

Fig. 3.14 shows the amplitude of shape oscillation, $\Delta D = D_{\max} - D_{\min}$. In the context of steady shear flows, it has been shown in recent studies that ΔD is non-monotonic with respect to varying Ca, and attains a maximum at intermediate values of Ca when the capsule is about make the transition from tank-treading to tumbling [24–26]. In oscillating shear flow, as shown in Fig. 3.14, our simulations show a non-monotonic behavior of ΔD with respect to T^*_{sh}; ΔD first increases with increasing T^*_{sh} reaching a maximum and then drops again. This result suggests a resonance between the natural frequency of the capsule and the frequency of imposed flow.

We now consider the effect of the aspect ratio α on the tumbling/swinging dynamics. It is well known that in a steady shear flow, the transition to tumbling

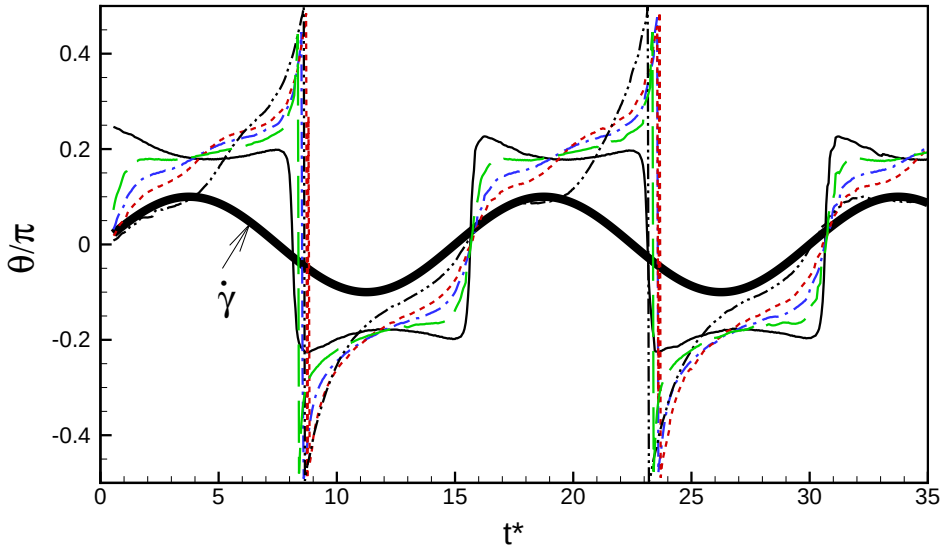

Figure 3.15: Color online. Effect of the aspect ratio α on capsule dynamics. —— $\alpha = 1$; — — — $\alpha = 0.9$; – · – $\alpha = 0.8$; - - - - - $\alpha = 0.7$; – ·· – $\alpha = 0.5$; thick solid line is $\dot{\gamma}$. Here Ca $= 0.2$, $\theta_o = 0$, and $T^*_{sh} = 15$.

occurs at progressively higher values of Ca [20, 25, 26], and lower values of λ [19, 20, 25], as the non-sphericity increases. Hence, it is of interest to see if the tumbling dynamics shown in Fig. 3.8 for $\alpha = 0.6$ will change to a swinging dynamics as α increases. This is illustrated in Fig. 3.15 where θ versus time is plotted for different values of α. As evidence, the continuous/unidirectional tumbling motion is observed even for $\alpha = 0.9$. Hence, we conclude that even a slight non-spherical initial shape leads to the tumbling motion in oscillating shear. For all values of $\alpha \leq 0.9$, a counter-clockwise tumbling is observed, while the membrane makes clockwise tank-treading motion.

The effect of the aspect ratio on the phase diagram is shown in Fig. 3.16 by considering $\alpha = 0.7$ and 0.8. The overall nature of the diagram remains the same

as observed before for $\alpha = 0.6$. The continuous/unidirectional tumbling motion is observed for intermediate values of Ca and T^*_{sh}, and the clockwise/counter-clockwise swinging motion is observed otherwise. The critical capillary numbers shift towards lower values of Ca with increasing α, as expected [19, 20].

3.2.3 Effect of initial condition: evidence of chaotic motion

As mentioned in the Introduction, Dupire et al. [1] found that the motion of the red blood cells in oscillating shear flow is highly sensitive to the initial condition. As discussed by them, chaos can be predicted by the Skotheim-Secomb's model [20] due to the coupled nature of the ordinary differential equations describing the capsule dynamics. Noguchi [48] also observed that at high shear frequency, multiple stable solutions exist that depend on the initial condition. Since our simulations are deterministic, it is of interest to see if the dynamics described above depends on the initial capsule orientation θ_o. Note that the results presented so far are for $\theta_o = 0$. Fig. 3.17 shows the capsule dynamics for six representative cases by varying θ_o from $\pi/12$ to $-\pi/4$ while the capillary number and oscillation period are held fixed at 0.2 and 15, respectively. Note that for this Ca and T^*_{sh}, a continuous/unidirectional tumbling motion was seen when $\theta_o = 0$ (refer to Fig. 3.8). As evident in Fig. 3.17 a similar tumbling motion is also observed for $\theta_o = \pi/12, \pi/2, -\pi/12$ and $-\pi/4$, but a clockwise/counter-clockwise

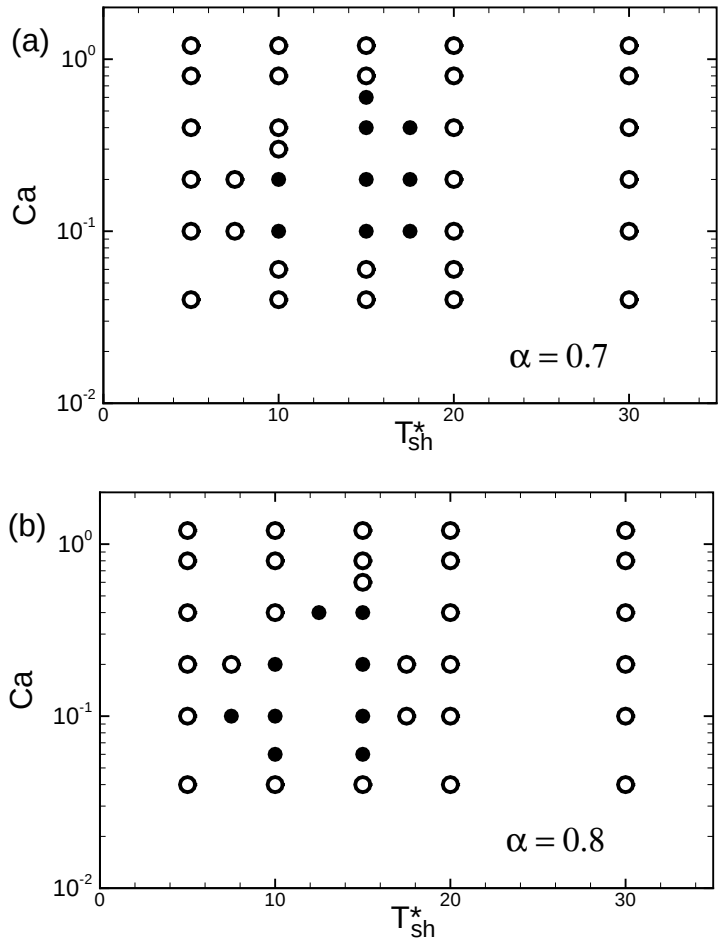

Figure 3.16: Phase diagram for $\alpha = 0.7$ and 0.8. Here $\theta_o = 0$. Symbols have the same meaning as in Fig. 3.13.

swinging motion is observed for $\theta_o = \pi/4$ and $-\pi/6$. The direction of the tumbling motion is also sensitive to θ_o: it is counter-clockwise for $\theta_o = \pm\pi/12$, but clockwise for $\pi/2$ and $-\pi/4$. The deformation response is also sensitive to θ_o. For example, identical deformation response during positive and negative vorticity is observed for $\theta_o = \pi/4$, but not for other values of θ_o. The dependence on θ_o is further illustrated using a phase diagram in Fig. 3.18 for $\alpha = 0.6$, Ca $= 0.2$, and $T^*_{sh} = 15$. In general, a clockwise/counter-clockwise swing is observed when the initial inclination is close to either the extensional or compressional axis of the shear flow; otherwise a continuous/unidirectional tumbling motion is observed. A counter-clockwise tumbling occurs when the capsule is released with its major axis aligned with the flow direction, and a clockwise tumbling occurs when it is perpendicular. The figure shows that a slight change in the initial condition near the extensional or compressional axis can lead to different dynamics.

Fig. 3.18 can also be used to explain why swinging or tumbling motion is observed for different θ_o, and also the clockwise and counter-clockwise direction of tumbling. In doing so, we keep in mind that a deformable capsule always 'prefers' to align with the extensional direction of the shear flow, and has its own natural timescale of shape oscillation. If the capsule is released nearly horizontally, it first elongates and seeks to align with $\theta = \pi/4$, and hence rotates counter-clockwise. The rotation rate is rather slow as it is in the direction opposite to the vorticity. By the time it reaches $\theta = \pi/4$, the flow reversal occurs, and the counter-clockwise rotation continues. In contrast, if the capsule is released nearly vertical, it has to

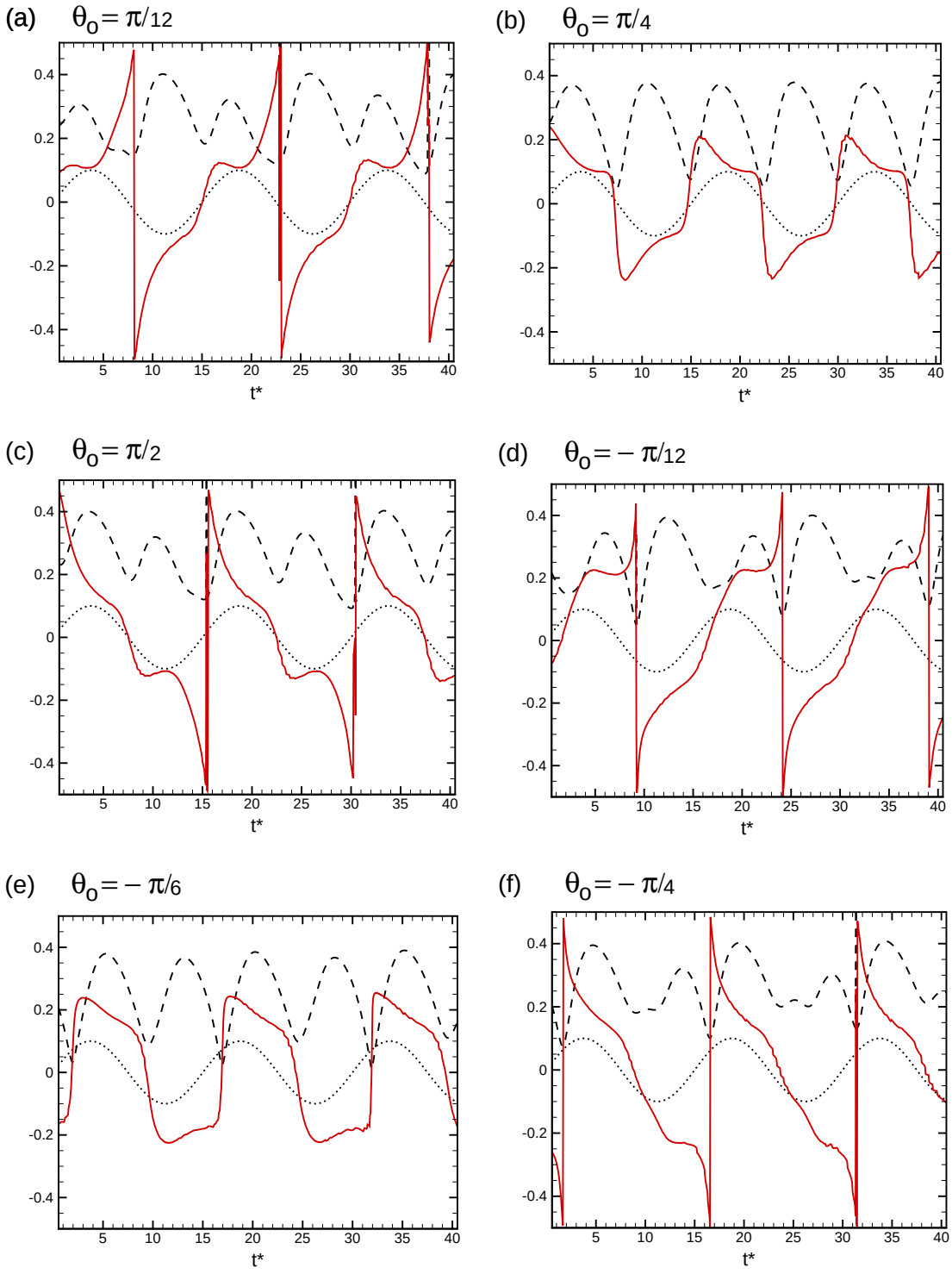

Figure 3.17: Color online. Effect of initial inclination θ_o. (a) to (f) correspond to $\theta_o = \pi/12, \pi/4, \pi/2, -\pi/12, -\pi/6, -\pi/4$, respectively. The aspect ratio $\alpha = 0.6$ and oscillation period $T^*_{sh} = 15$ are held fixed. —— θ/π, - - - - - D, $\cdots$ $\cdots$ $\dot{\gamma}$.

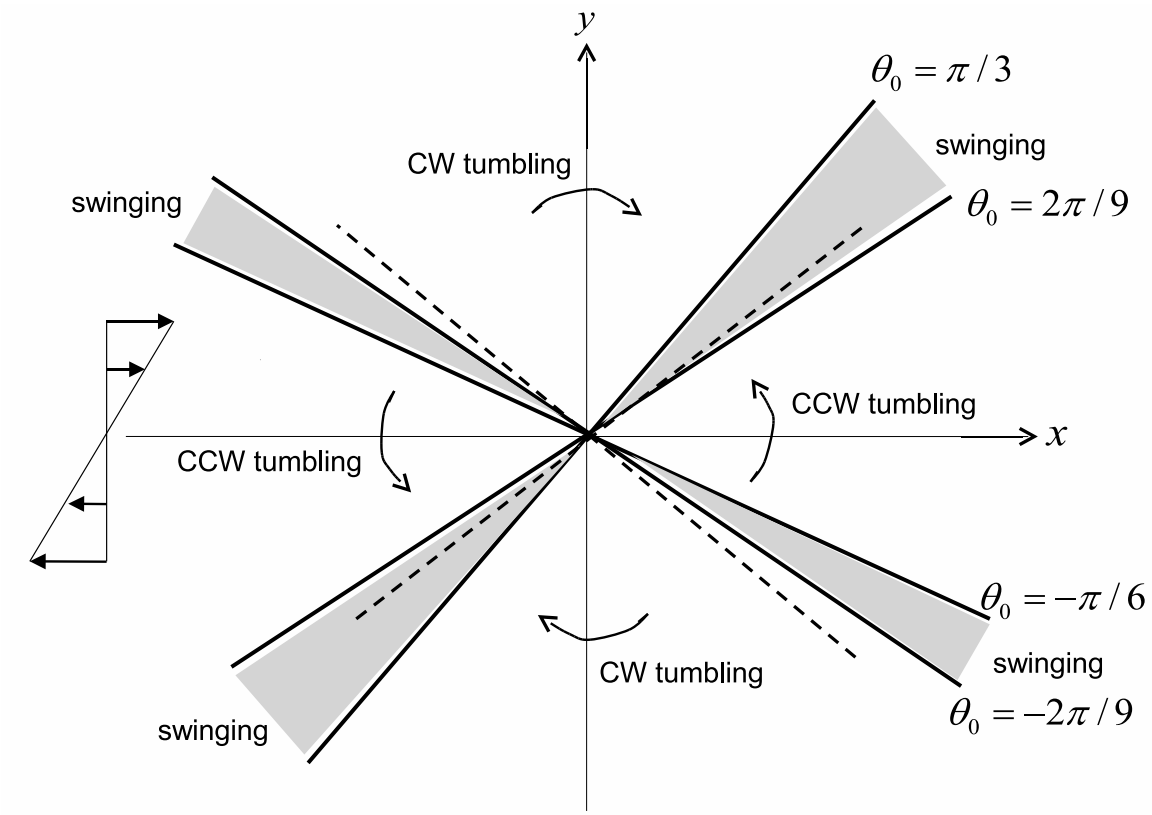

Figure 3.18: Dependence of swinging/tumbling motion on θ_o for $\alpha = 0.6$, Ca $= 0.2$, and $T^*_{sh} = 15$. The white areas represent the range of θ_o that yields the continuous and unidirectional tumbling motion, and the gray areas represent the clockwise/counter-clockwise swinging. The dashed lines are the extensional and compressional axes ($\pm\pi/4$).

rotate clockwise to align with $\theta = \pi/4$. This rotation occurs relatively faster due to a higher hydrodynamic torque acting on the vertically aligned capsule. After it reaches close to $\theta = \pi/4$, the natural shape compression starts before the flow reversal can occur. As a result, the capsule continues to rotate clockwise, and the major axis drops below $\theta = 0$. At this time flow reversal occurs, and the capsule seeks to align with the extension direction of this reversed flow causing further clockwise rotation. Evidently, the tumbling dynamics here is due to the strong shape oscillation, and would not occur if deformation was inhibited.

3.3 Dynamics at Unequal Internal and External Fluid Viscosity

In the previous section, we considered the internal to external viscosity ratio $\lambda = 1$. In this section, we will consider the effect of the viscosity ratio on the capsule dynamics under oscillating shear.

3.3.1 Dynamics under steady shear flow: effect of varying viscosity ratio

Before considering the oscillating shear, we review the capsule dynamics in steady shear under varying viscosity ratio. Fig. 3.19 shows the effect of increasing viscosity ratio on the capsule dynamics for an initially spherical resting shape. As before, the initially spherical capsule attains a steady deformed shape in the form of an oblate spheroid, and a fixed inclination angle with the flow direction, while

the membrane and the internal fluid make a tank-treading motion. Thus, for a spherical capsule, a steady tank-treading motion is observed even when the viscosity ratio is increased to a very high value. The time history of deformation and inclination angle is also shown in the figure. We see that both deformation and inclination angle decreases with increasing viscosity raito since capsule is increasingly solidified.

Next, we show some sample results for a nonspherical capsule in a steady shear flow and under varying internal to external fluid viscosity ratio in Fig. 3.20. As mentioned before, the nonspherical capsule undergoes unsteady dynamics even in a steady shear flow. Here we consider the initial aspect ratio $\alpha = 0.7$, and $\mathrm{Ca} = 0.05$, and vary the viscosity ratio as $\lambda = 2$ and 10. For $\lambda = 2$, a swinging dynamics is observed, where as for $\lambda = 10$ a tumbling motion is observed. In both cases, a significant shape oscillation is evident which suggests that deformation plays an important role in capsule dynamics. These results depict that a swinging dynamics occurs at a low viscosity ratio, but a tumbling dynamics occurs at a high viscosity ratio, as predicted by the Keller-Skalak theory for a shape-preserving capsule.

3.3.2 Dynamics under oscillating shear flow: effect of varying viscosity ratio

Now we present some results on the dynamics in oscillating shear flow under varying viscosity ratio. Here we take the initial shape corresponding to $\alpha = 0.6$.

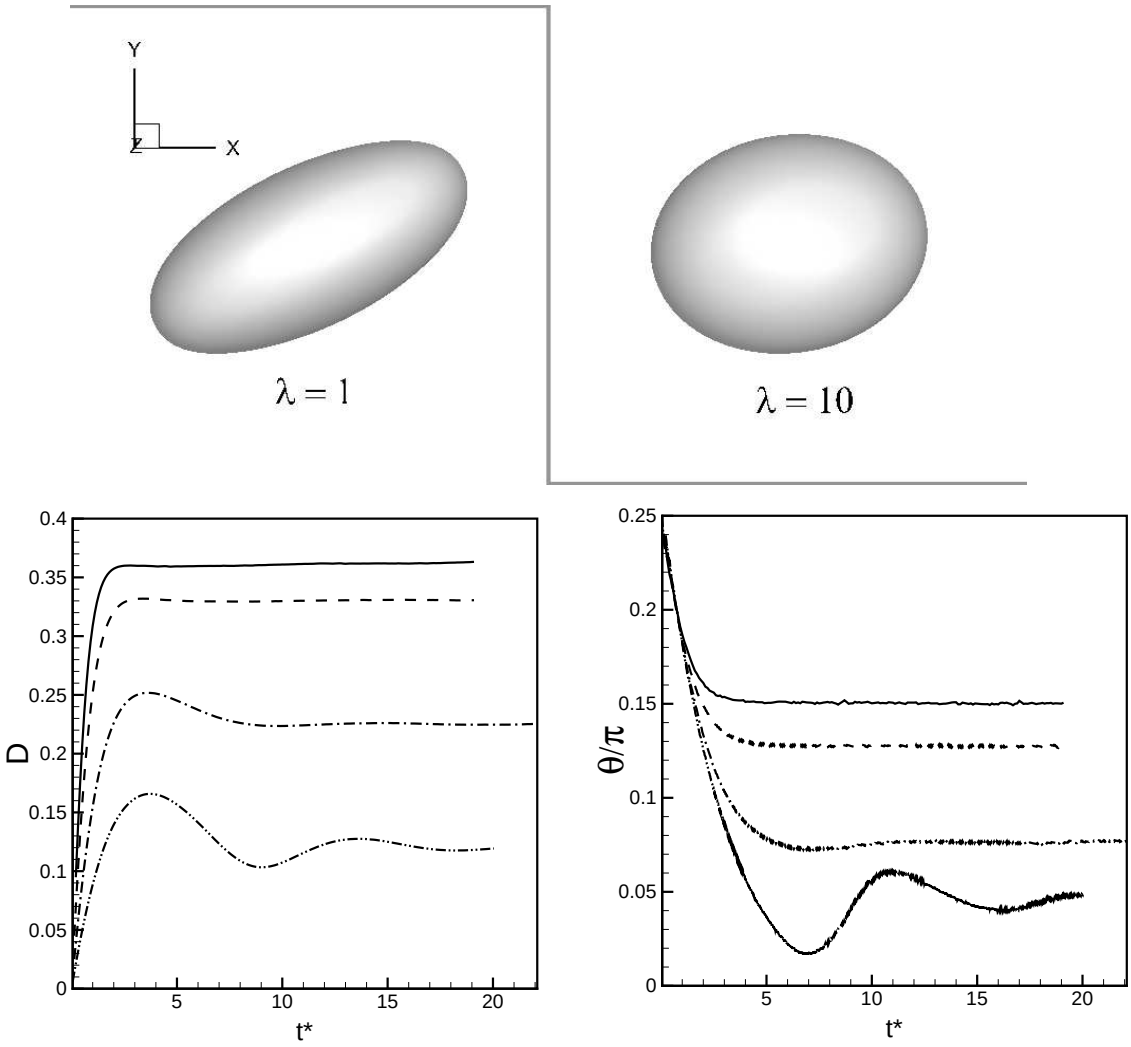

Figure 3.19: Dynamics of an initially spherical capsule in a steady shear flow: effect of the internal to external viscosity ratio λ is shown. Here Ca = 0.2. The steady shapes are shown for $\lambda = 1$ and 10. The time history of the Taylor deformation parameter D and the inclination angle θ is shown for $\lambda = 1$ (——), 2 (- - - - -), 5 (-·-·-), and 10 (-·-·-·-).

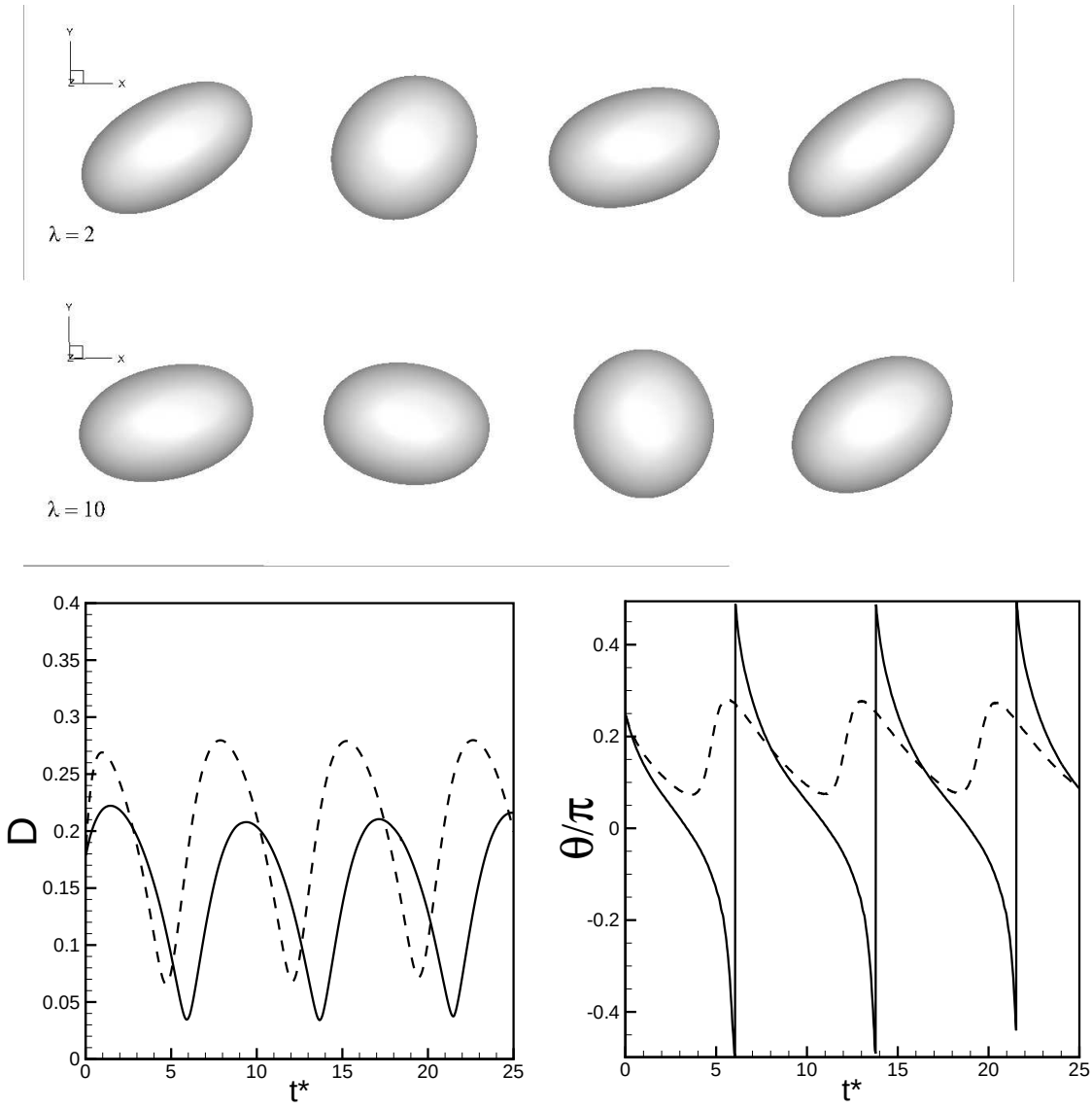

Figure 3.20: Dynamics of an initially nonspherical capsule in a steady shear flow: effect of the internal to external viscosity ratio λ is shown. Here $\alpha = 0.7$, and Ca $= 0.05$. The top figure is for $\lambda = 2$, and the next for $\lambda = 10$. The shapes are shown at $t^* = 1$, 5, 10, 15 for $\lambda = 2$, and 2, 6, 8, 10 for $\lambda = 10$. The time history of the Taylor deformation parameter D and the inclination angle θ is shown for $\lambda = 2$ (- - - - -), and 10 (——).

The results for Ca = 0.1 and 0.4 are shown in Figs. 3.21 and 3.22, respectively. The viscosity ratio λ is varied as 1, 5, and 10. In general we see that the dynamics at $\lambda = 1$ and 5 are similar, although the detailed time-dependence is different. In contrast, the dynamics at $\lambda = 10$ is different. Specifically, we see that at $T^*_{sh} = 15$, and Ca = 0.1, a continuous and unidirectional tumbling motion occurs for both $\lambda = 1$ and 5. In contrast, a large amplitude swinging motion occurs for $\lambda = 10$. This is bacause the capsule is 'rigidified' at thi high viscosity ratio, and the dynamics is similar to that of a rigid ellipsoid which undergoes only a swinging motion. When we increase the capillary number to 0.4, a swinging motion is observed for all viscosity ratios. However, the capsule with $\lambda = 10$ again behaves like a nearly rigid body, and hence shows a large-amplitude swinging.

The time dependence of the Taylor deformation parameter is shown in Figs. 3.23 and 3.24 for Ca = 0.1 and 0.4, respectively. In general we see that the deformation response is smoother for $\lambda = 10$, but more complex for the lower viscosity ratios with subharmonic variations appearing. This is because at the lower viscosity raitos, the natural shape oscillation dominates. In contrast, at $\lambda = 10$, the natural shape oscillation is rather small, and the capsule deformation is primarily dictated by the altering shear flow.

Thus, we can conclude that the complex dynamics that was observed in the earlier section, that is, the unidirectional tumbling motion at intermediate oscillation period and shear rate amplitudes, is absent at higher viscosity ratio due to the reduction of deformability.

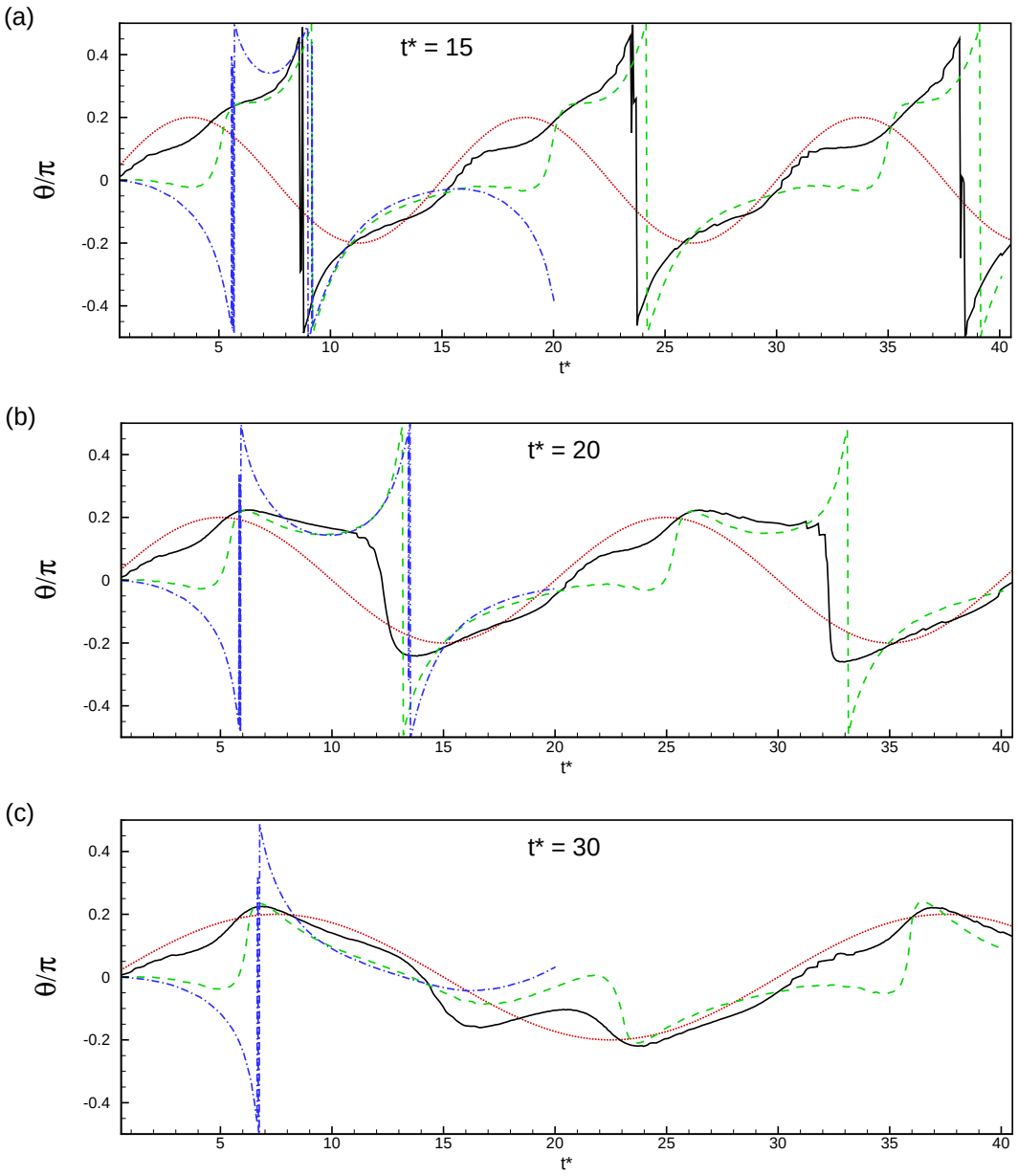

Figure 3.21: Dynamics of nonspherical capsule in oscillating shear flow: effect of the internal to external viscosity ratio λ is shown on the instantaneous inclination angle. Here $\alpha = 0.6$, and $\mathrm{Ca} = 0.1$ are kept constant, and λ is varied as 1 (——), 5 (- - - - -), and 10 (-·-·-). Three different oscillation periods are considered. The instantaneous shear rate is shown by the dotted line in arbitrary scale.

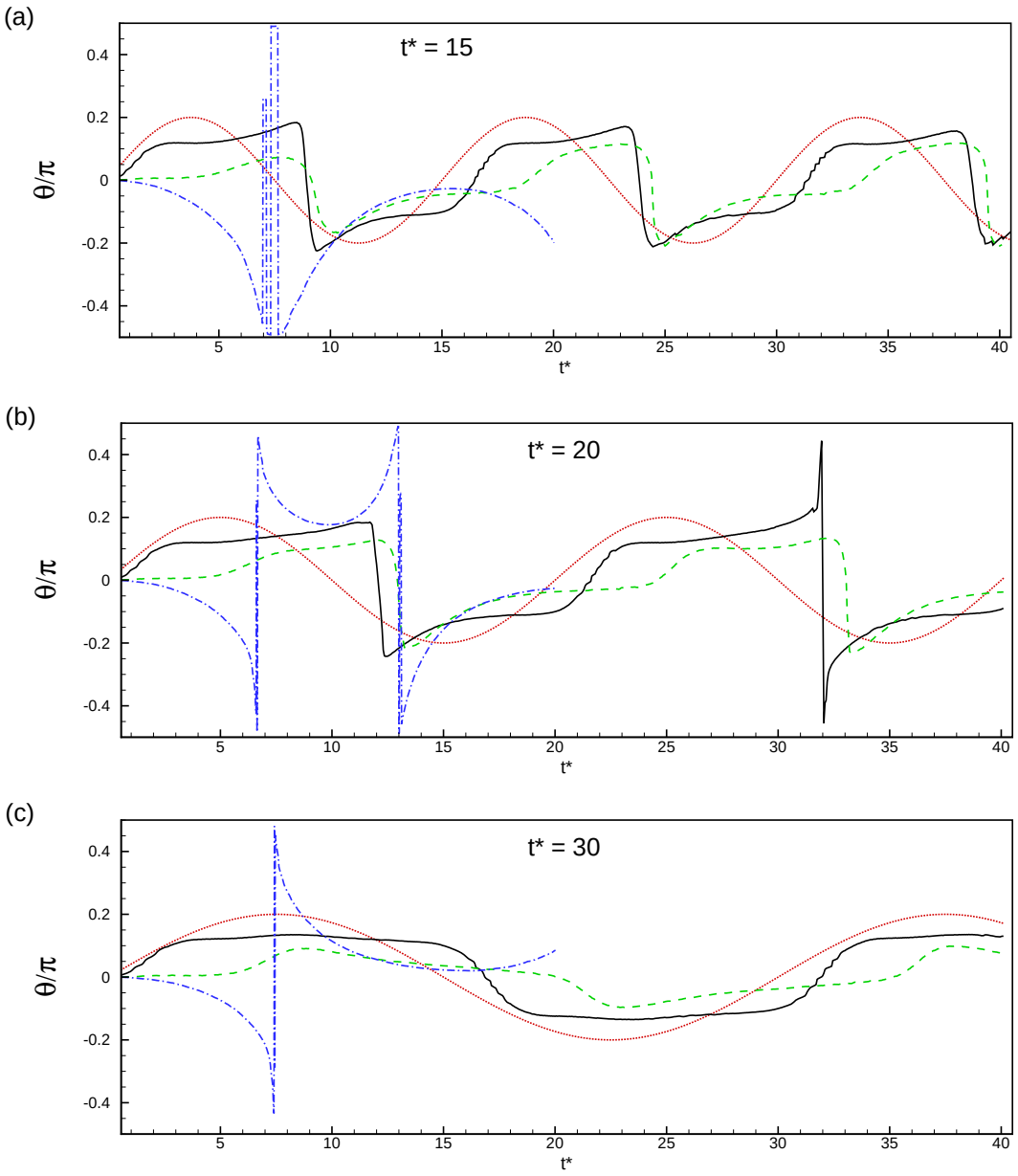

Figure 3.22: Dynamics of nonspherical capsule in oscillating shear flow: effect of the internal to external viscosity ratio λ is shown on the instantaneous inclination angle. Here $\alpha = 0.6$, and $\mathrm{Ca} = 0.4$ are kept constant, and λ is varied as 1 (——), 5 (- - - - -), and 10 (-·-·-). Three different oscillation periods are considered. The instantaneous shear rate is shown by the dotted line in arbitrary scale.

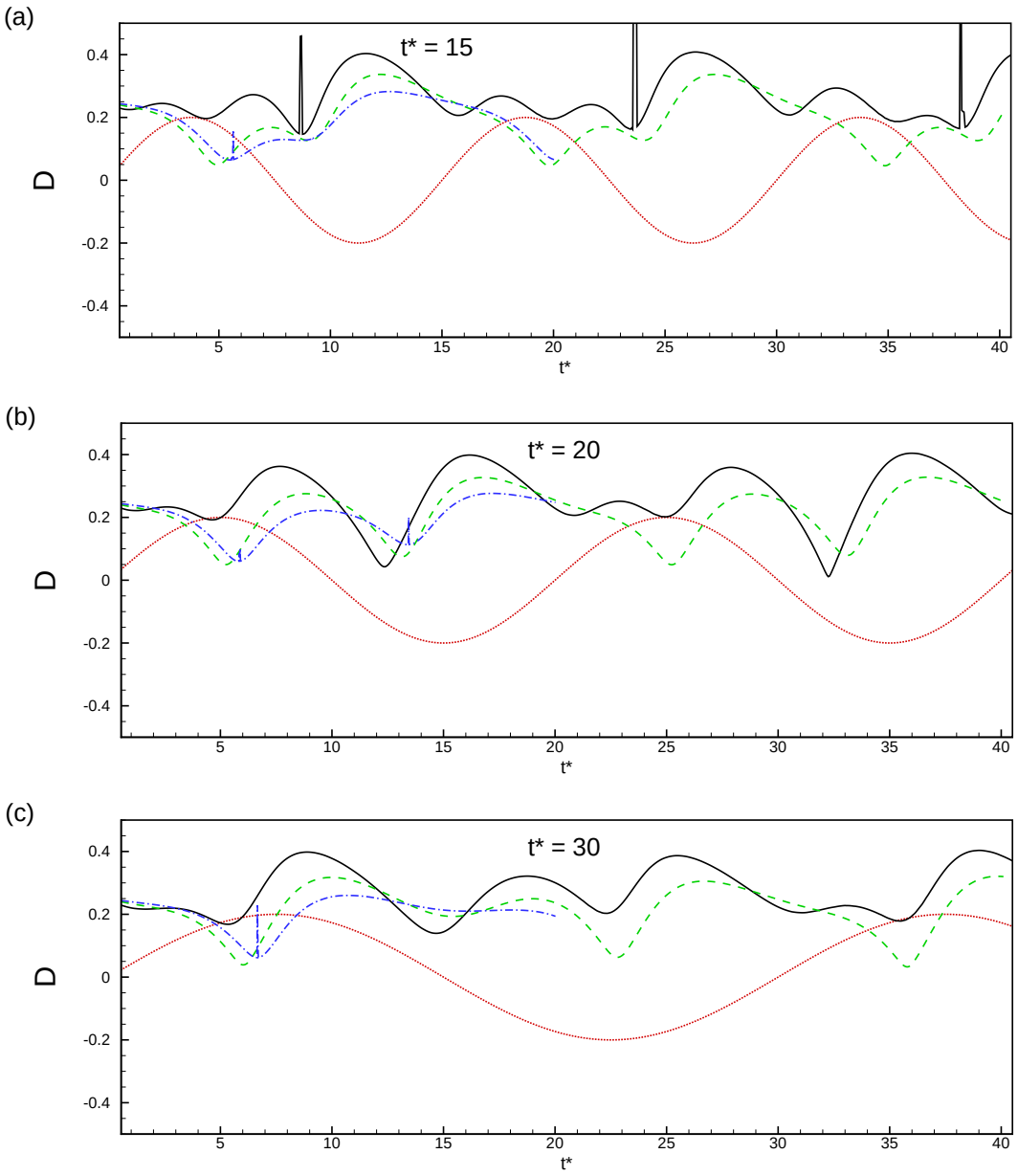

Figure 3.23: Dynamics of nonspherical capsule in oscillating shear flow: effect of the internal to external viscosity ratio λ is shown on the time dependent deformation. Here $\alpha = 0.6$, and $\mathrm{Ca} = 0.1$ are kept constant, and λ is varied as 1 (——), 5 (- - - - -), and 10 (-·-·-). Three different oscillation periods are considered. The instantaneous shear rate is shown by the dotted line in arbitrary scale.

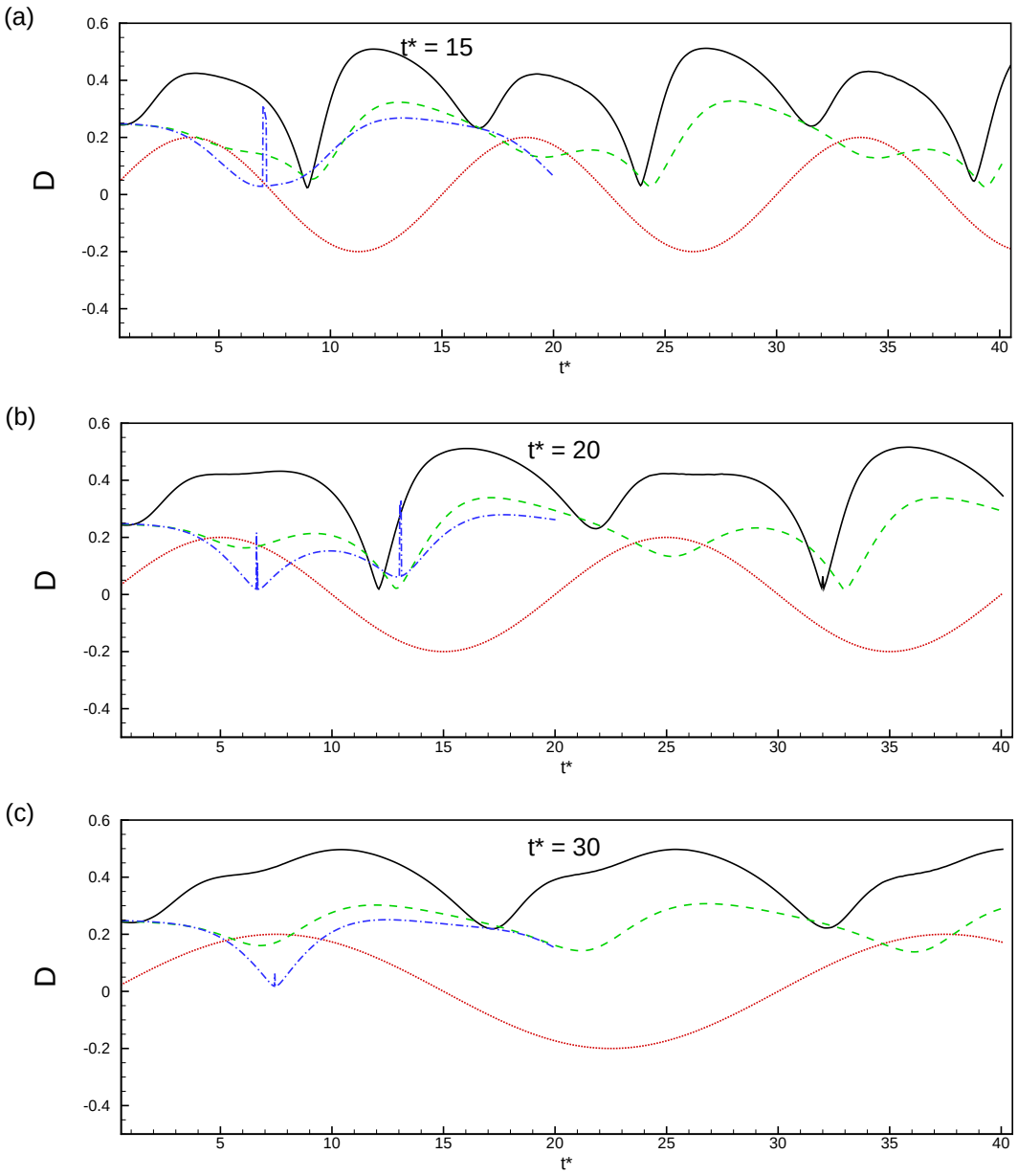

Figure 3.24: Dynamics of nonspherical capsule in oscillating shear flow: effect of the internal to external viscosity ratio λ is shown on the time dependent deformation. Here $\alpha = 0.6$, and $\mathrm{Ca} = 0.4$ are kept constant, and λ is varied as 1 (——), 5 (- - - - -), and 10 (-·-·-). Three different oscillation periods are considered. The instantaneous shear rate is shown by the dotted line in arbitrary scale.

3.4 Dynamics of Initially Spherical Capsules at Finite Mean Oscillating Shear

The imposed shear flow considered in the previous sections has a zero mean when averaged over an oscillation period. In this section we will consider an oscillating shear flow for which the time-average is non-zero. That is, we impose a shear flow as

$$\dot{\gamma} = \dot{\gamma}_o \left[1 + \epsilon \sin\left(\frac{2\pi t}{T_{sh}} \right) \right] \tag{3.3}$$

where $\dot{\gamma}_o$ is the finite mean shear rate, ϵ is the dimensionless amplitude of the time-dependent perturbation and is positive, and T_{sh} is the oscillation period. Note that unlike in the previous sections on zero-mean shear flow in which the imposed flow reverses its direction at every half period, in the present case no flow reversal can occur if $0 < \epsilon < 1$. Thus the zero-mean shear is a special case of the present situation when $\epsilon \to \infty$ but $\epsilon\dot{\gamma}_o$ is finite. Here we restrict our attention to $0 < \epsilon < 1$. Further, the capillary number here is defined slightly differently using the mean shear rate as Ca $=\mu_o a\dot{\gamma}_o/E_s$, and the dimensionless oscillation period as $T^*_{sh} = \dot{\gamma}_o T_{sh}$. Thus, the relevant dimensionless parameters here are: the capillary number Ca, the perturbation amplitude ϵ, the viscosity ratio λ, the oscillation period T^*_{sh}, and the aspect ratio α of the initial shape of the capsule.

Let us first restrict our attention the initially spherical capsules only. The

time dependent Taylor deformation parameter D and the inclination angle of the capsule major axis θ are shown in Fig. 3.25 and 3.26 for $\lambda = 5$ and 10, respectively. In each figure, we consider four different values of Ca as 0.05, 0.1, 0.4 and 1.0. For each case, we vary the perturbation amplitude ϵ as 0.1, 0.5 and 1.0. The oscillation frequency T^*_{sh} is kept constant at 10. Time dependent capsule shapes are show in Fig. 3.27 for two representative cases. The deformation and inclination angle oscillate with time in response to the oscillating perturbation, and the amplitudes of their oscillation increase with increasing ϵ. The maximum elongation occurs when the instantaneous shear rate $\dot{\gamma}$ reaches its maximum. But the minimum deformation lags behind the minimum shear rate. This is because the elongation occurs at a faster time scale than the compression of the capsule. This is also evident from the deformation curves which show non-harmonic behavior: the elongation phase of the curves are much steeper than the compression phase. Also interesting to note is the time average deformation that appears to decrease with increasing perturbation amplitude. Note that the rate of flow acceleration and retardation defines another time scale which is much smaller at higher perturbation amplitude, and smaller than the capsule response time. Thus the capsule is unable to responds to the flow at higher perturbation amplitudes leading to a reduced mean deformation. Also interesting is the amplitude of the deformation response and inclination angle which appear to decrease with increasing Ca. This is due to the increased response time for highly deformable capsules.

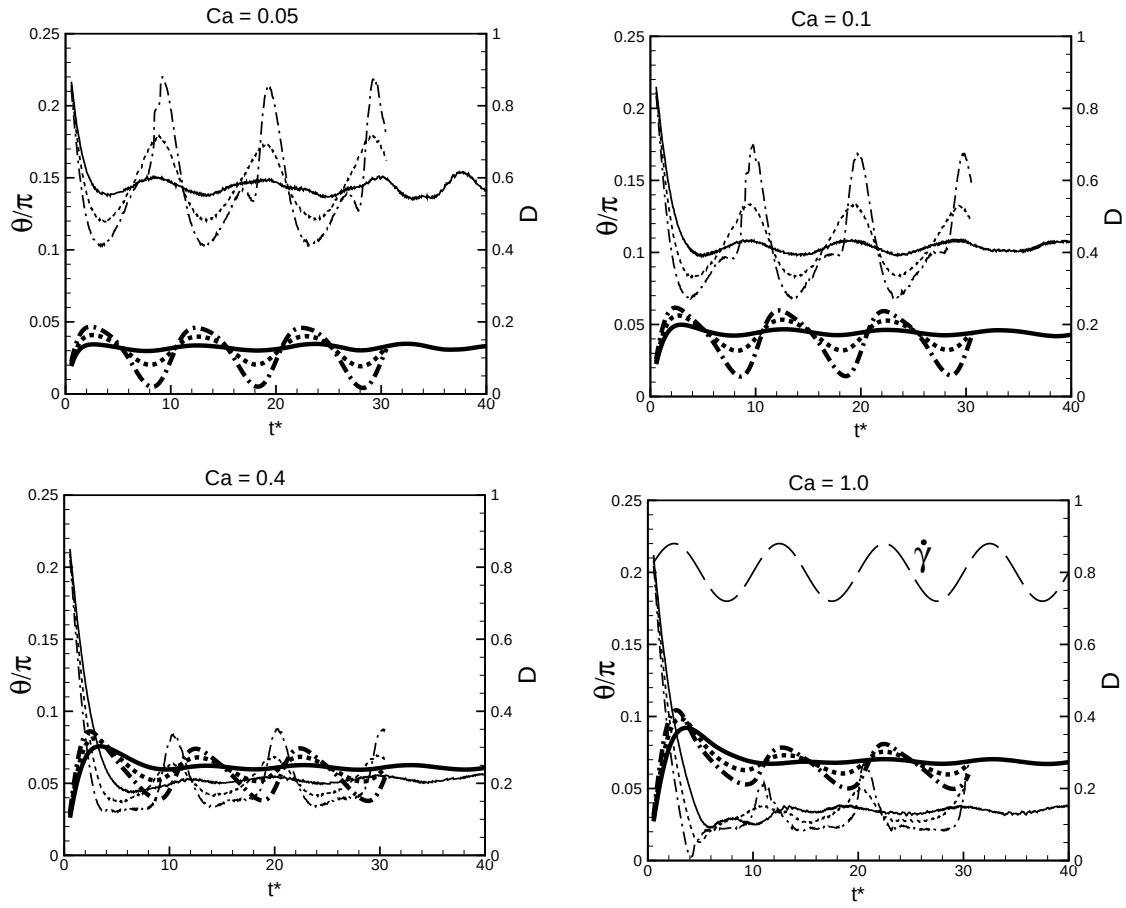

Figure 3.25: Dynamics of initially spherical capsule in finite-mean oscillating shear flow: effect of the shear amplitude ϵ is shown at different capillary numbers. Here the viscosity ratio is kept constant at $\lambda = 5$ and the oscillation period at $T^*_{sh} = 10$. Time dependence of the deformation parameter (right scale, thick lines) and the inclination angle (left scale, thin lines) is shown. $\epsilon = 0.1$ (——), 0.5 (- - - - -), 1.0 (-·-·-). The instantaneous shear rate is also shown using arbitrary scale.

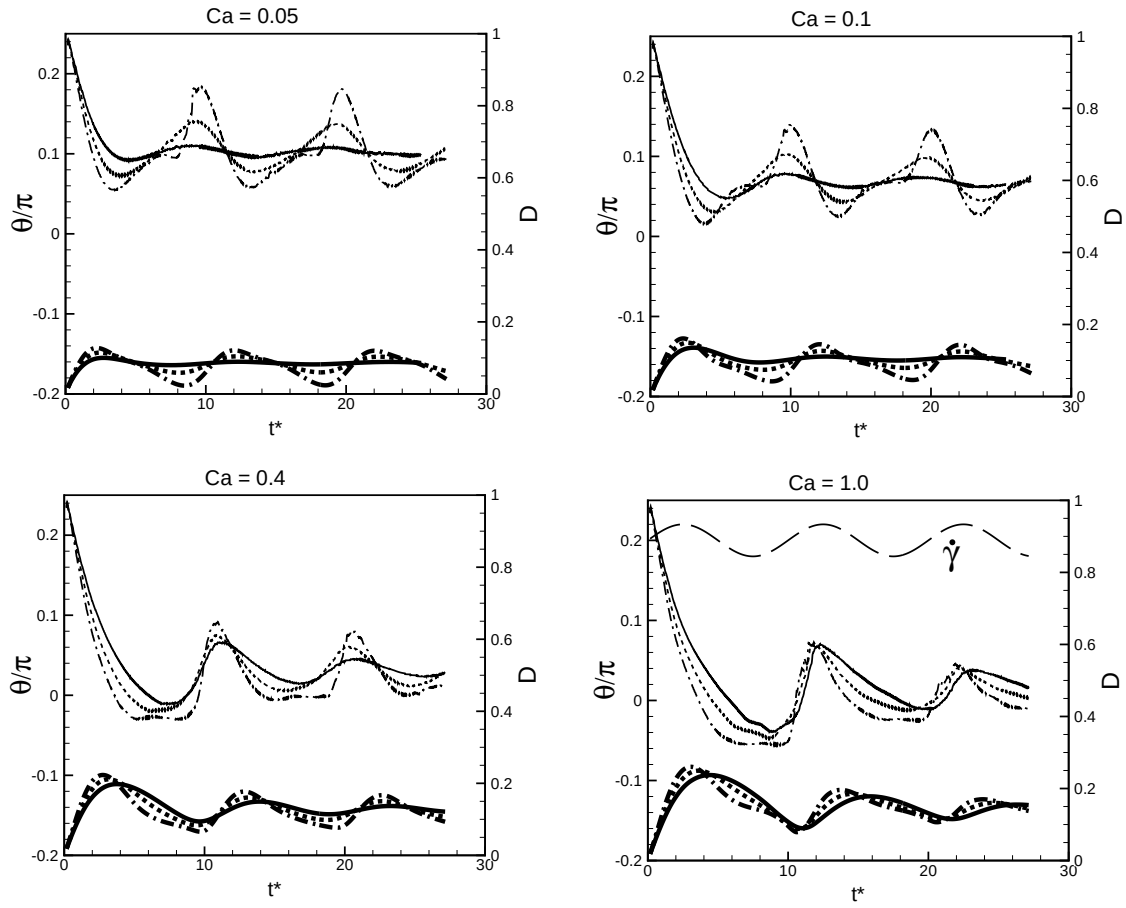

Figure 3.26: Dynamics of initially spherical capsule in finite-mean oscillating shear flow: effect of the shear amplitude ϵ is shown at different capillary numbers. Here the viscosity ratio is kept constant at $\lambda = 10$ and the oscillation period at $T^*_{sh} = 10$. Time dependence of the deformation parameter (right scale, thick lines) and the inclination angle (left scale, thin lines) is shown. $\epsilon = 0.1$ (——), 0.5 (- - - - -), 1.0 (-·-·-). The instantaneous shear rate is also shown using arbitrary scale.

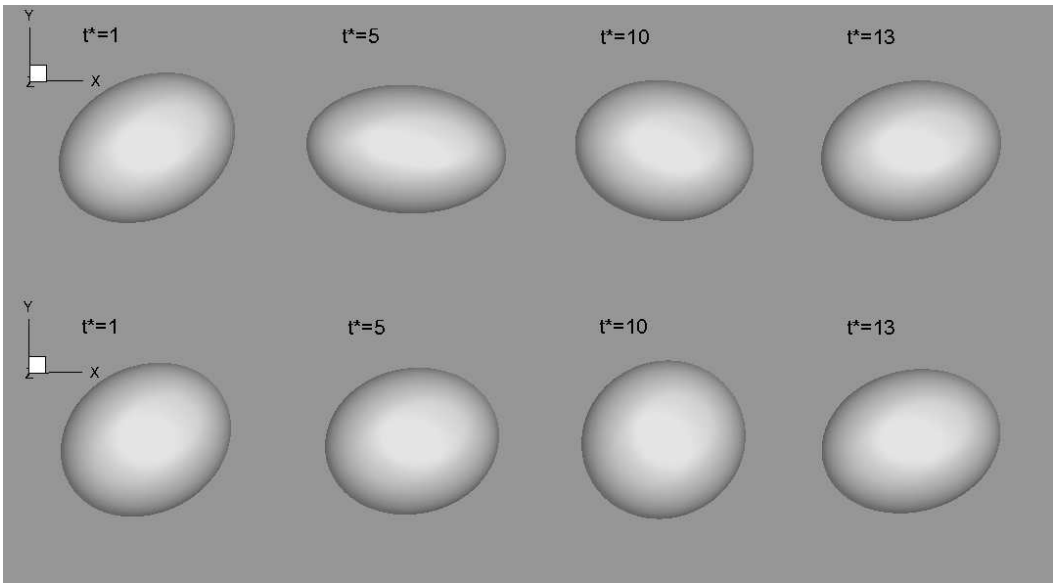

Figure 3.27: Dynamics of initially spherical capsule in finite-mean oscillating shear flow: instantaneous capsule shapes are shown for Ca = 1.0 (top) and 0.05 (bottom) for $\lambda = 10$ and $T^*_{sh} = 10$.

3.5 Sensitivity to the Direction of Shear Start-up

Fig. 3.28 shows the sensitivity of the dynamics when the direction of the starting flow is reversed. We will consider only a zero-mean shear flow. Equivalently, we consider the effect of positive and negative values of the shear amplitude $\dot{\gamma}$. The results are shown for a spherical capsule and for a non-spherical capsule released at $\theta_o = 0$. As seen in the figure, the deformation responses are identical in the two cases, and the inclination angles are just the mirror image about $\theta = 0$. Note that for the spherical capsule case, the initial release angle is immaterial. Thus, it is expected that the results would be independent of positive or negative shear amplitude. For the non-spherical capsules, the release angle is important. In the latter case, if $\theta_o = 0$, the reversing direction has no effect on the results. However, for $\theta_o \neq 0$, the reversing direction does have a significant effect on the dynamics as discussed in earlier section giving rise to chaotic behavior.

3.6 Non-periodic Dynamics at Finite-mean Oscillating Shear Flow

Our study on zero-mean oscillatory shear flow shows only the presence of a periodic motion, in contrast to the non-periodic motion experimentally observed and theoretically predicted by Dupire et al. using red blood cells. Here we present some preliminary results for nonspherical capsules in finite-mean oscillating shear flow as shown in Fig. 3.29. We also consider the effect of altering the direction of the flow start-up while the capsule release angle is maintained the same. As

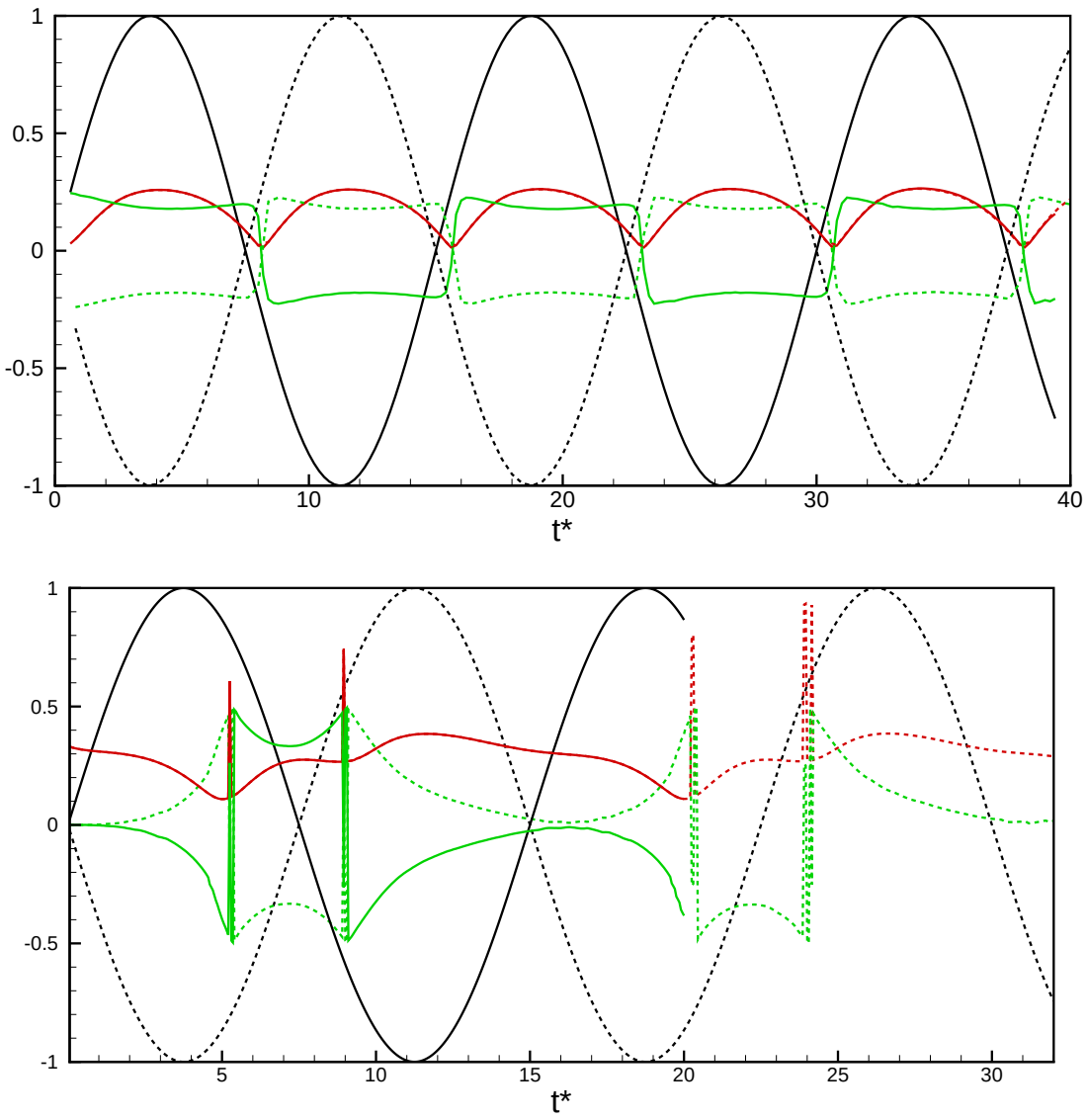

Figure 3.28: Sensitivity of the dynamics to the reversal of the starting flow direction. Black solid and dashed lines are positive and negative shear rates, respectively, green solid and dashed lines are the corresponding inclination angles, and red line is the Taylor deformation parameter for which solid and dashed lines are identical. Top figure is for initially spherical capsules at Ca = 0.1, $\lambda = 1$, $T^*_{sh} = 15$, and the bottom figure for an oblate capsule at $\alpha = 0.5$, Ca = 0.05, $\lambda = 5$, $T^*_{sh} = 15$, and $\theta_o = 0$.

expected, the response is not identical in the two cases. More interestingly, we see that over a longer time, a non-periodic motion characterized by a combination of swinging and occassional tumbling is present. It should be mentioned though that the identification of swinging and tumbling for this case is difficult as we consider $\alpha = 0.5$ for which the capsule momentraily becomes spherical in the shear plane (as indicated by $D \to 0$). Further study along this line is left for the future.

3.7 Dynamics of Red Blood Cells in Zero-mean Oscillating Flow

In previous sections, we studied capsules of initial spherical and oblate spheroid shapes. These resting shapes are usually encountered for artificially made capsules. For a healthy human red blood cells, spherical and oblate resting shapes are possible when at reduced osmolarity (or, tonicity) of the suspending medium. For example, at a tonocity of about 131 mosmol, a human red bood cell attains a spherical resting shape, due to an increased transmural pressure. Spherical and oblate resting shapes are also possible under disease conditions, or at some times during the life cycle of the cell, or under non-hydrodynamic external fields. Under normal physiological conditions, however, the resting shape of a red blood cell is the well-known *biconcave discoid* shape. Such a shape provides a high value of surface area to volume ratio for enhanced diffusion of gasses across the cell membrane. This 'excess area', however, provides a huge numerical difficulty as the simulated cell shapes often exhibit sharp kinks if not properly resolved. Further,

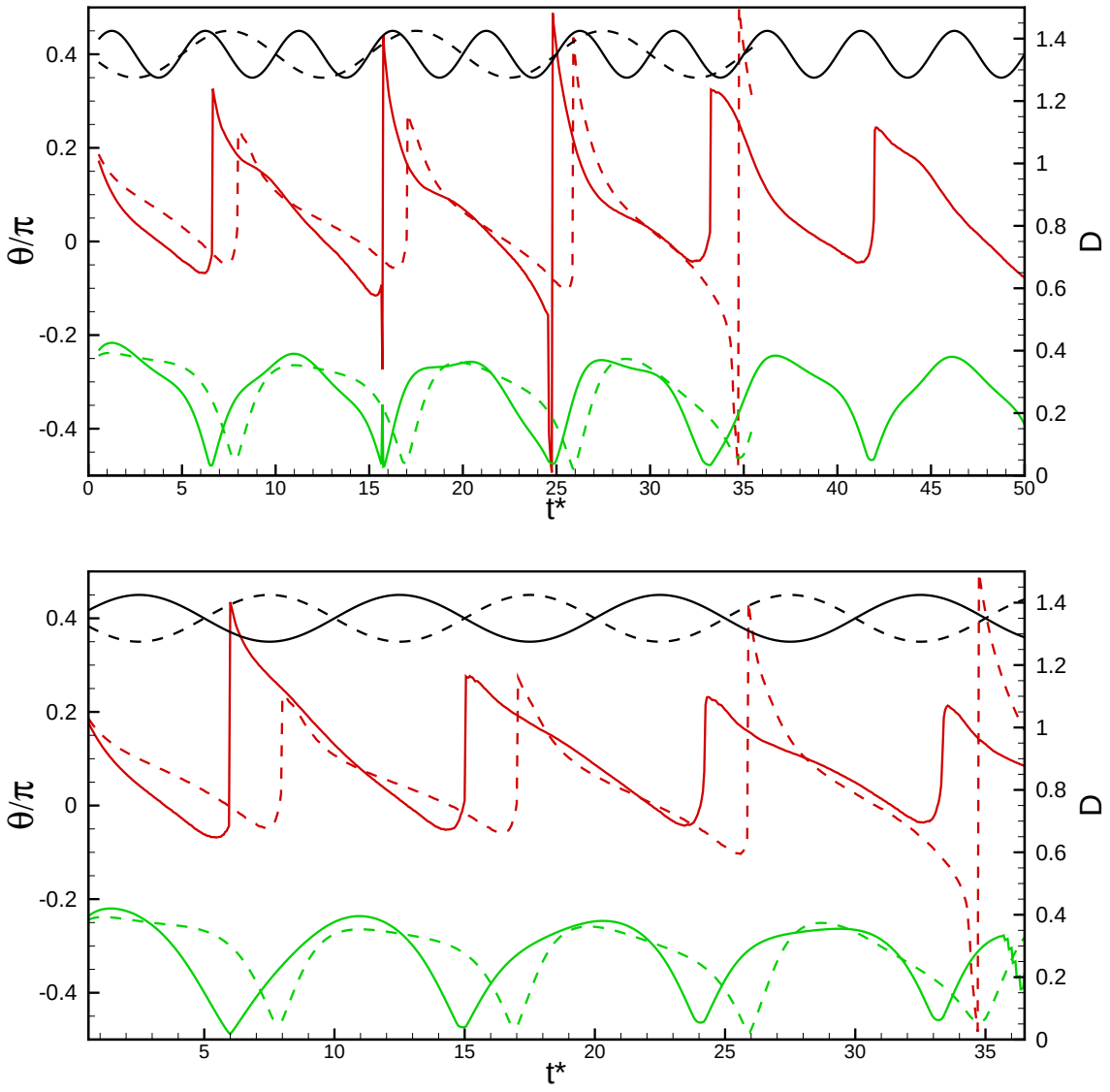

Figure 3.29: Non-periodic dynamics at finite-mean oscillating shear flow. Here $\alpha = 0.5$, Ca $= 0.1$, $\lambda = 5$, $\epsilon = 0.5$, and $\theta_o = \pi/4$ are fixed, and T^*_{sh} is varied as 5 and 10 in top and bottom figures. Black lines are the shear rates, green lines represent the Taylor deformation parameter, and the red lines are the instantaneous inclination angle. Solid and dashed lines are the positive and negative perturbation amplitude.

unlike in the previous sections, where the capsule surface area is allowed to dilate, the red blood cell surface area is nearly preserved during deformation. This also proves to be numerically challenging within the framework of the front-tracking method as the immersed boundary forces tend to become singular in the limit that the area is perfectly incompressible. Nevertheless, the present effort is motivated by the experimental works of Dupire et al. using the human red blood cells. Note that unlike in Dupire et al., we do not observe non-periodic dynamics for capsules, and we argued that the lack of non-periodicity is due to the presence of the deformability in our simulations. Further, the aspect ratio considered so far is $\alpha \geq 0.6$. In contrast, for a resting red blood cell, it is about 0.25. The different aspect ratio considered in the two studies could also be the reason for the discrepancy. Thus, it is our objective in this section to extend our simulations to actual red blood cells to see if non-periodic motion is possible.

Description of the numerical method is the same as in Chapter 2. The biconcave resting shape is prescribed as

$$x = R\eta, \qquad y = \frac{R}{2}\sqrt{1-r^2}(C_0 + C_2 r^2 + C_4 r^4), \qquad z = R\zeta, \tag{3.4}$$

where $\eta^2 + \zeta^2 = r^2$, and R is adjusted to control the cell volume. The surface area and the volume of the red blood cell are taken to be $134.1\mu\text{m}^2$ and $94.1\mu\text{m}^3$, respectively. The initial shape is stress-free. The coefficients C_0, C_2, and C_4

depend on the osmolarity, and are taken to be 0.207, 2.003, and -1.123, respectively. We use $a = (3V/4\pi)^{1/3}$ as the length scale where V is the cell volume. The flow field is discretized using 120^3 Eulerian mesh points, whereas the cell surface is discretized using 20480 triangular elements. The spontaneous curvature is set to $c_o a_o = -2.09$. The area dilatation parameter C is varied from 50 to 400 to ensure that the global and local area dilatation is less than 0.5%. Note that for a real cell the parameter $C \approx 10^5$; however, using such a high value results in numerical instability. It appears that numerical instability occurs at progressively lower values of C as Ca decreases. The range of C used here is found using a series of numerical tests so that the area can be conserved as far as possible without creating numerical instability. Hence, the RBC surface is nearly, not entirely, area-incompressible in our model.

3.7.1 RBC dynamics in steady shear flow

For the purpose of completeness, we present some salient features of the RBC dynamics in a steady shear flow in Fig. 3.31. The details of this work can be found in Yazdani and Bagchi, Phys Rev E 84, 026314 (2011) [69]. In general, an isolated red blood cell exhibits tank-treading, swinging and tumbling motion, similar to the nonspherical capsule dynamics described earlier. However, due to its 'excess area', the deformation and inclination dynamics of the red blood cell is more complex. Fig. 3.31a shows the dynamics at high capillary number in which the biconcave shape is completely absent, and the cell assumes rather a convex shape.

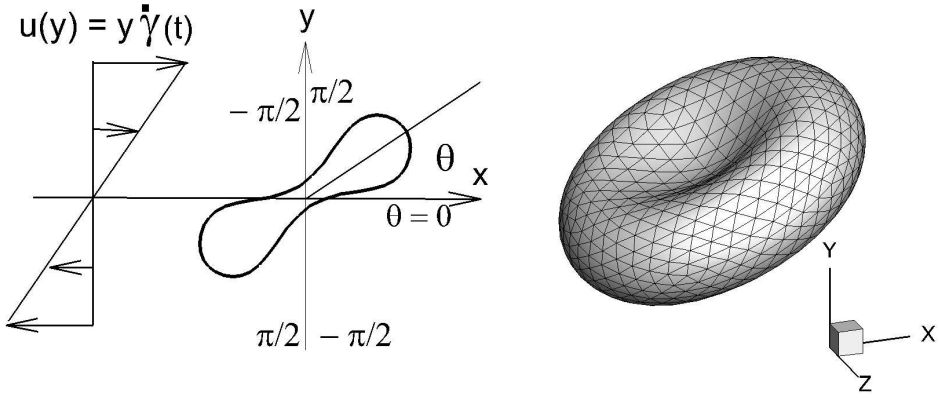

Figure 3.30: Schematic of a red blood cell in oscillating shear flow.

No significant shape or angular oscillation is visible here. The cell membrane and the interior fluid undergo a tank-treading motion. When the capillary number is decreased, a swinging motion is observed in which the cell oscillates about a mean inclination while the membrane and the interior fluid make a oscillating tank-treading motion. Upon further decrease in capillary number, a tumbling motion is observed as shown in Fig. 3.31c. In many situations, however, more complex dynamics is observed in which the cell undergoes a significant shape oscillation, and a clear swinging or tumbling cannot be established as shown for one case in Fig. 3.31b, Here we term them as a 'breathing' dynamics, as the animations resemble a similar process. For the dimensionless bending rigidity $E_B^* = 0.01$, the tank-treading biconvex shape is obtained for Ca > 0.6, the swinging dynamics for

$0.05 < \text{Ca} < 0.6$, and the tumbling dynamics for $\text{Ca} < 0.05$. The transition from the tank-treading to the tumbling motion also occurs with increasing viscosity ratio when the capillary number is held constant. For $\lambda > 5$, mostly the tumbling motion occurs for a capillary number as high as 1.

3.7.2 RBC dynamics in zero-mean oscillating shear flow

We have performed simulations with RBC over a wide range of the three relevant parameters: capillary number Ca varying from 0.02 to 0.6, the viscosity ratio λ varied as 0.5, 1 and 5, and the dimensionless oscillation period T^*_{sh} ranging from 10 to 100. First we will present the results for $\lambda = 1$, followed by that for $\lambda = 5$. We find that the results for $\lambda = 0.5$ are qualitatively similar to those at $\lambda = 1$, and hence, not presented.

First we consider $\text{Ca} = 0.05$ for which the RBC tumbles in a steady shear flow. Hence, in the oscillating shear for $\text{Ca} = 0.05$, the RBC dynamics is similar to a rigid ellipsoid. Fig. 3.32 shows the snapshots for $T^*_{sh} = 20$. Nearly no significant shape deformation can be observed here. The marker point shown on the cell surface exhibits no relative motion. Thus the tank-treading is absent. Instead, the cell swings CW and CCW like a rigid ellipsoid in resposne to the altering shear flow. The oscillation is harmonic, as expected for a rigid ellipsoid.

Fig. 3.32 also shows the time dependence of the inclination angle for various shear oscillation periods. In a steady shear, the tumbling period at $\text{Ca} = 0.05$ is $T^*_n \approx 21$. Hence, at low oscillating period, a full swinging motion is not possible

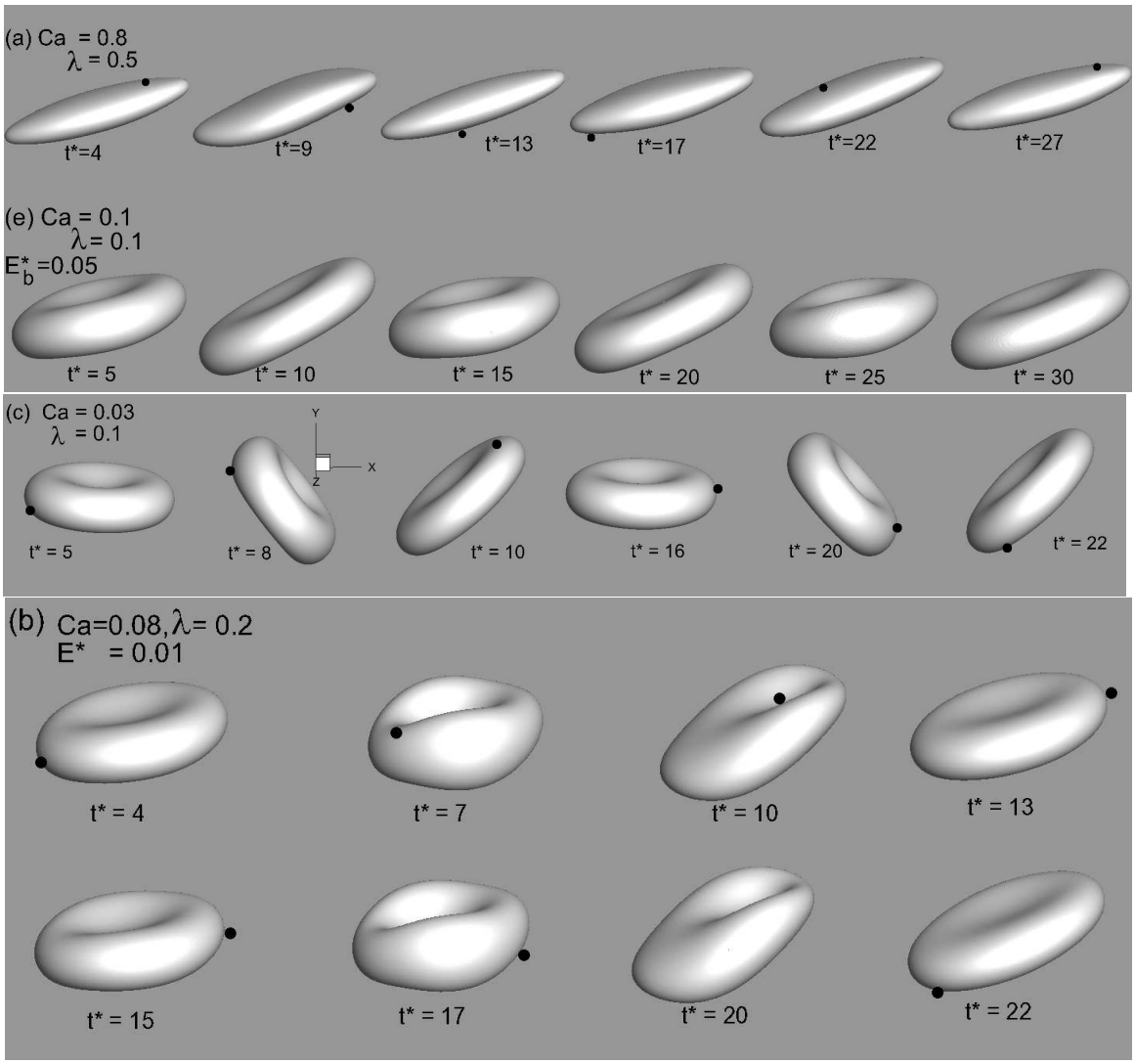

Figure 3.31: Dynamics of red blood cells in a steady shear flow. First row: tank-treading without any significant cell shape and angular oscillation (Ca = 0.8, $\lambda = 0.5$, $E_b^* = 0.01$), second row: swinging (Ca=0.1, $\lambda = 0.1$, $E_b^* = 0.05$), third row: tumbling (Ca = 0.03, $\lambda = 0.1$, $E_b^* = 0.01$), last two rows: breathing (Ca = 0.08, $\lambda = 0.2$, $E_b^* = 0.01$). Yazdani & Bagchi, Phys Rev E 84, 026314 (2011).

as the flow reversal happens earlier. Evidently, for $T^*_{sh} = 10$ and 20, a CW/CCW swinging occurs. A full tumbling motion is observed for the oscillating periods that are greter than $T^*_n = 21$, e.g. for $T^*_{sh} = 60$.

Next we show a representative run at a high shear rate given by Ca = 0.6, and low oscillation period of $T^*_{sh} = 10$. Under a steady shear flow, the cell at this Ca undergoes a tank-treading motion with a small angular and shape oscillation. Qualitatively similar dynamics is observed in the oscillating shear flow. Also important to note that the deformation and inclination are nearly periodic, and that the marker point moves back-and-forth on the cell membrane. At the end of one cycle, the marker point comes back to its starting location. The inclination angle lags behind the shear, since the cell response time is larger at this high shear rate. The deformation is characterized by the maximum instantaneous cell length L measured on the shear plane, and Z measured along the vorticity direction. Both L and Z oscillate in time. While the incination angle varies harmonically, the deformation response shows subharmonic oscillations arising from the natural cell oscillation. The deformation response also shows asymmetry. The maximum elongation (L) is noted when $\dot{\gamma}$ becomes zero while going from negative to positive value, but not the otherway. In other words, the maximum elongation occurs during the accelerating phase. The maximum elongation leads to a compression in the vorticity direction since the cell volume and surface area are preserved. We conclude that at high Ca and low oscillation period, the dynamics is periodic as the capsule response time is much larger than the flow time scale. Only a

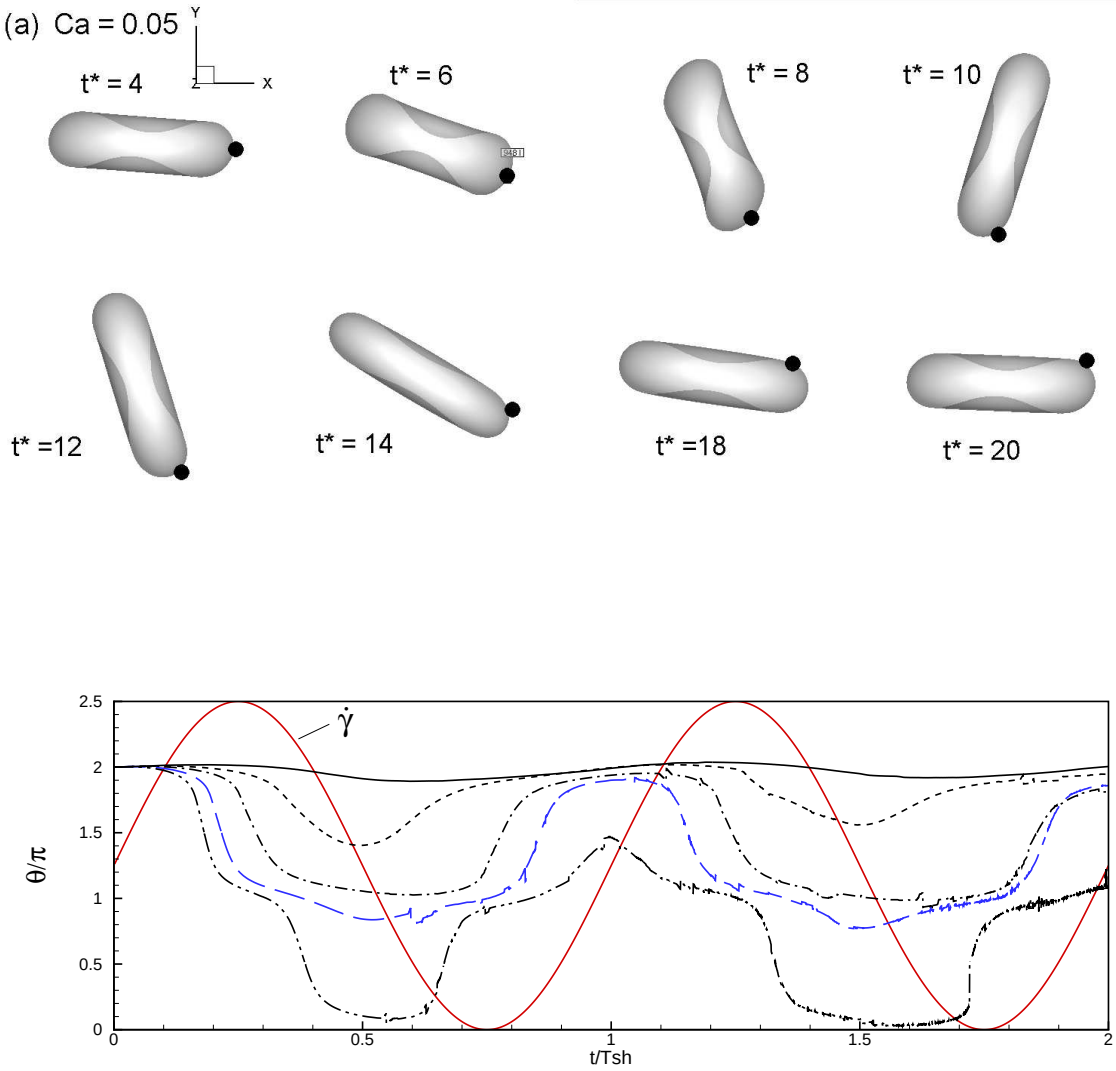

Figure 3.32: RBC dynamics in zero-mean oscillating shear flow at low shear rates. Snapshots for Ca = 0.05, $\lambda = 1$, $T^*_{sh} = 20$. Orientation angle θ/π for Ca = 0.05, $\lambda = 1$ under varying oscillation period $T^*_{sh} = 10$ (——), 20 (- - - - -), 30 (-·-·-), 45 (– – –), 60 (–··–). The red line is the instantansous shear rate shown on arbitrary scale.

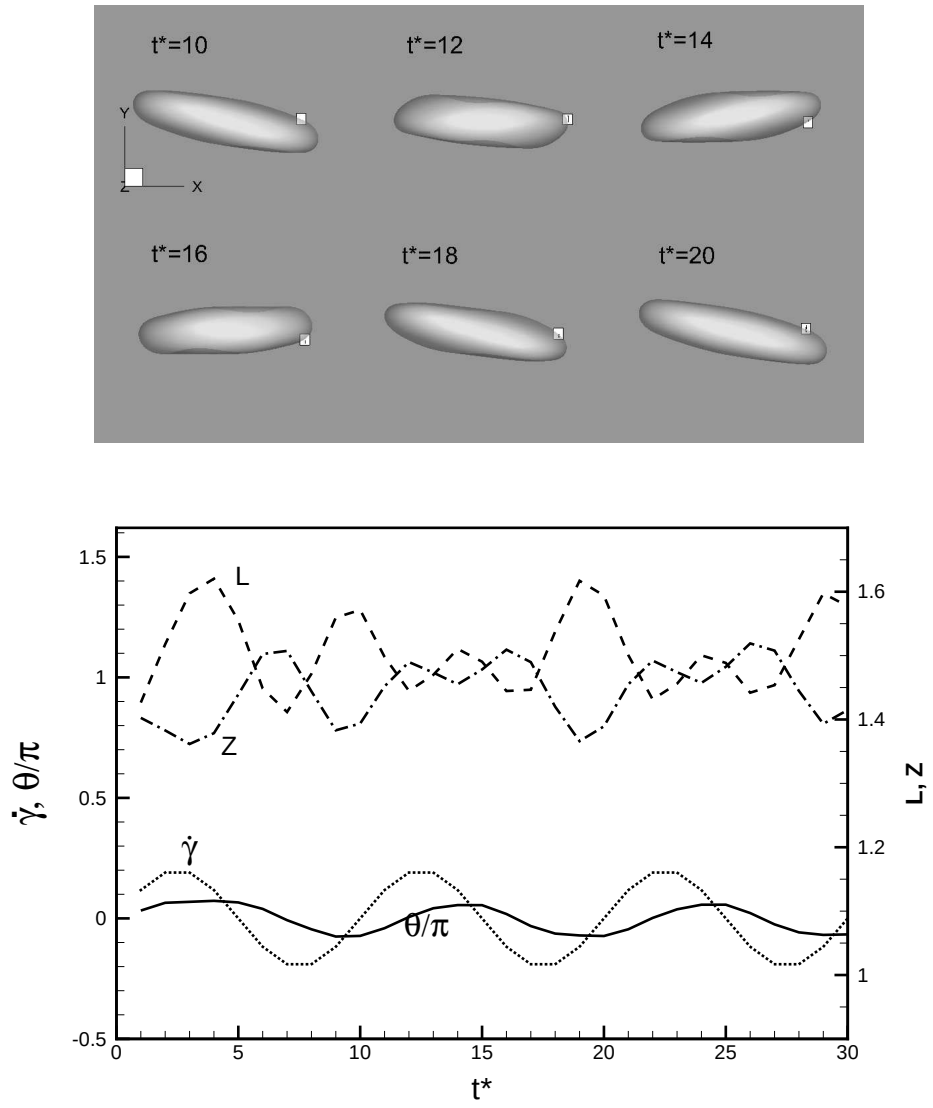

Figure 3.33: RBC dynamics in zero-mean oscillating shear flow at high shear rate and low oscillation period. Top: snapshots for Ca = 0.6, $T^*_{sh} = 10$. Bottom: instantaneous inclination, shear rate, maximum cell length in the shear plane (L) and in the vorticity direction (Z).

CW/CCW swinging motion is possible in this range of Ca and T^*_{sh}.

At intermediate capillary numbers and oscillation poriods, the dynamics is more complex than that described above. One such example is shown in Fig. 3.7.2 for Ca = 0.1, $T^*_{sh} = 45$. For $1 < t^* < 25$, the cell motion resembles a tumbling-like dynamics – the marker point shows no apparent movement. The cell rotates about 210 degree clockwise. For $25 < t^* < 45$, the dynamics resembles a tank-treading motion: the cell oreintation remains nearly fixed and along the negative quadrant while the marker point moves counter-clockwise. During this time the cell undergoes a significant deformation. Comparing figures at $t^* = 1$ and 45, no net displacement of the marker point is seen. So durng the forward phase, no motion of marker point, only the cell tumbles. The reverse phase: no cell motion, the marker point moves back to its original location. Second cycle is also shown. Here a tumbling-like motion occurs for $45 < t^* < 60$ during which the cell rotates clockwise about 120 degree. During this time, deformation is very small and the marker point shows no movement. Then for $60 < t^* < 73$, a significant deformation occurs by which the cell aligns in the negative quadrant. Even during this time, the marker point does not move implying that this phase is a tumbling-like motion combined with deformation. For $75 < t^* < 90$, a tank-treading-like motion is seen during which the cell orientation remains nearly the same while the marker point moves CCW back to its original location. The minimum in L occurs when $\theta = 0$, and the maximum and minimum in Z occur at zero shear and maximum shear, respectively.

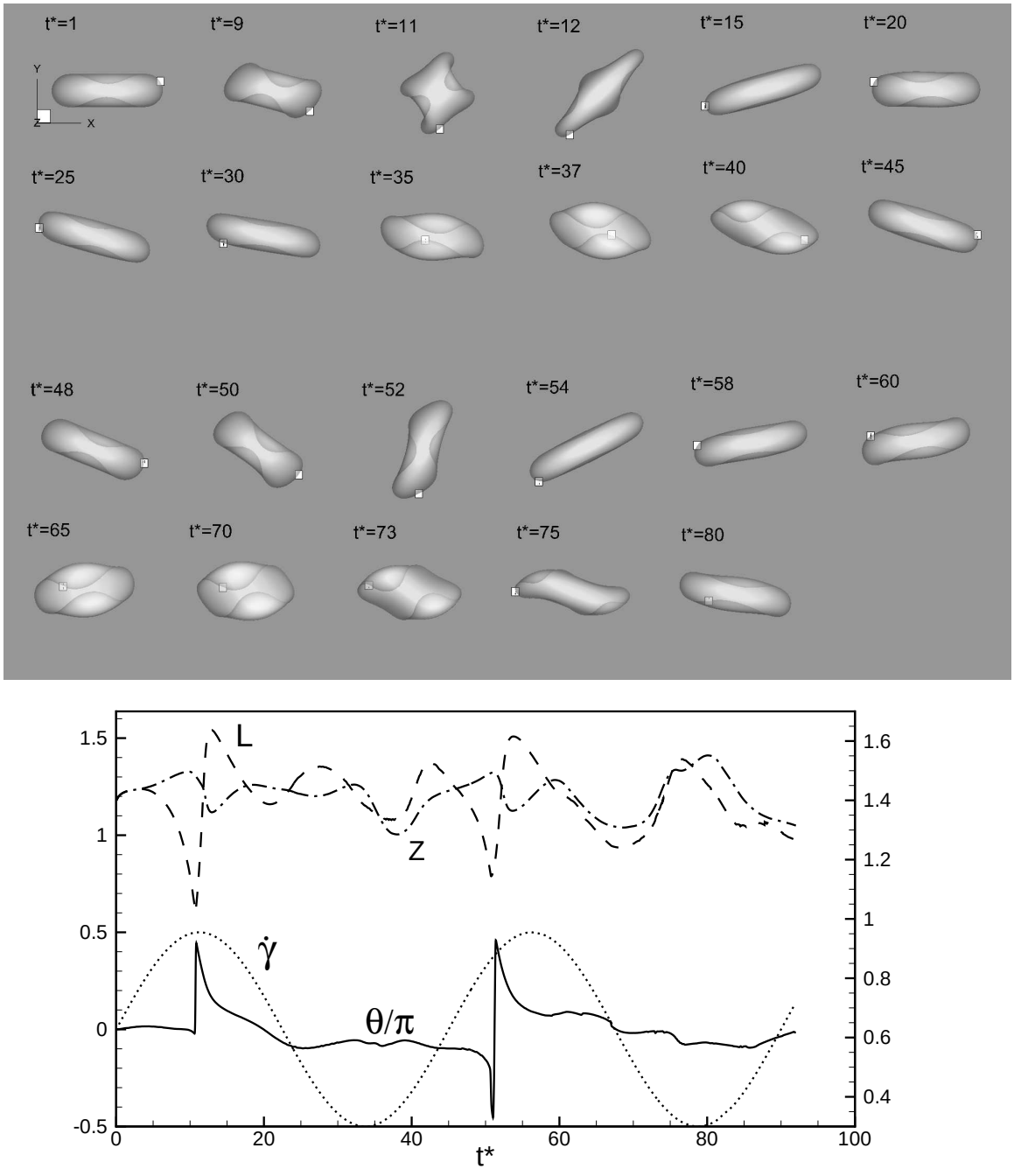

Figure 3.34: RBC dynamics in zero-mean oscillating shear flow at intermediate shear rate and oscillation period. Top: snapshots for Ca = 0.1, $T^*_{sh} = 45$. Bottom: instantaneous inclination, shear rate, maximum cell length in the shear plane (L) and in the vorticity direction (Z).

A similar dynamics is observed for Ca = 0.4, $T^*_{sh} = 20$ as shown in Fig. 3.7.2 that is characterized by a swinging motion accompanied by a large deformation for $t^* < 45$, followed by a tumbling, and then swinging. Thus, we conclude that at the intermediate shear ampliutudes and oscillation periods, the dynamics is characterized by a non-periodic motion similar to the experimental findings of Dupire et al.. However, in the present case, the cell deformaiton is the reason behind such non-periodic dynamics. We recall that at the intermediate shear rates, the RBC undergoes a significant shape oscillation. The natural shape oscillation when superimposed on the imposed shear oscillation yields the non-periodic dynamics. If deformation is inhibited, such non-periodic motion would not be possible in our deterministic simulations.

Finally we consider the physiological value of $\lambda = 5$ for which a smaple case is shown in Fig. 3.36. At the physiological value, only a periodic motion is observed similar to CW/CCW oscillation of a rigid ellipsoid. We have extended the simulations to consider high shear amplitudes as Ca = 1.0 for a time window of two shear periods. Periodic motion is observed even at this value of Ca. Thus, we conclude that the loss of deformation at the physiological value of the viscosity ratio prohibits the occurance of the non-periodic motion.

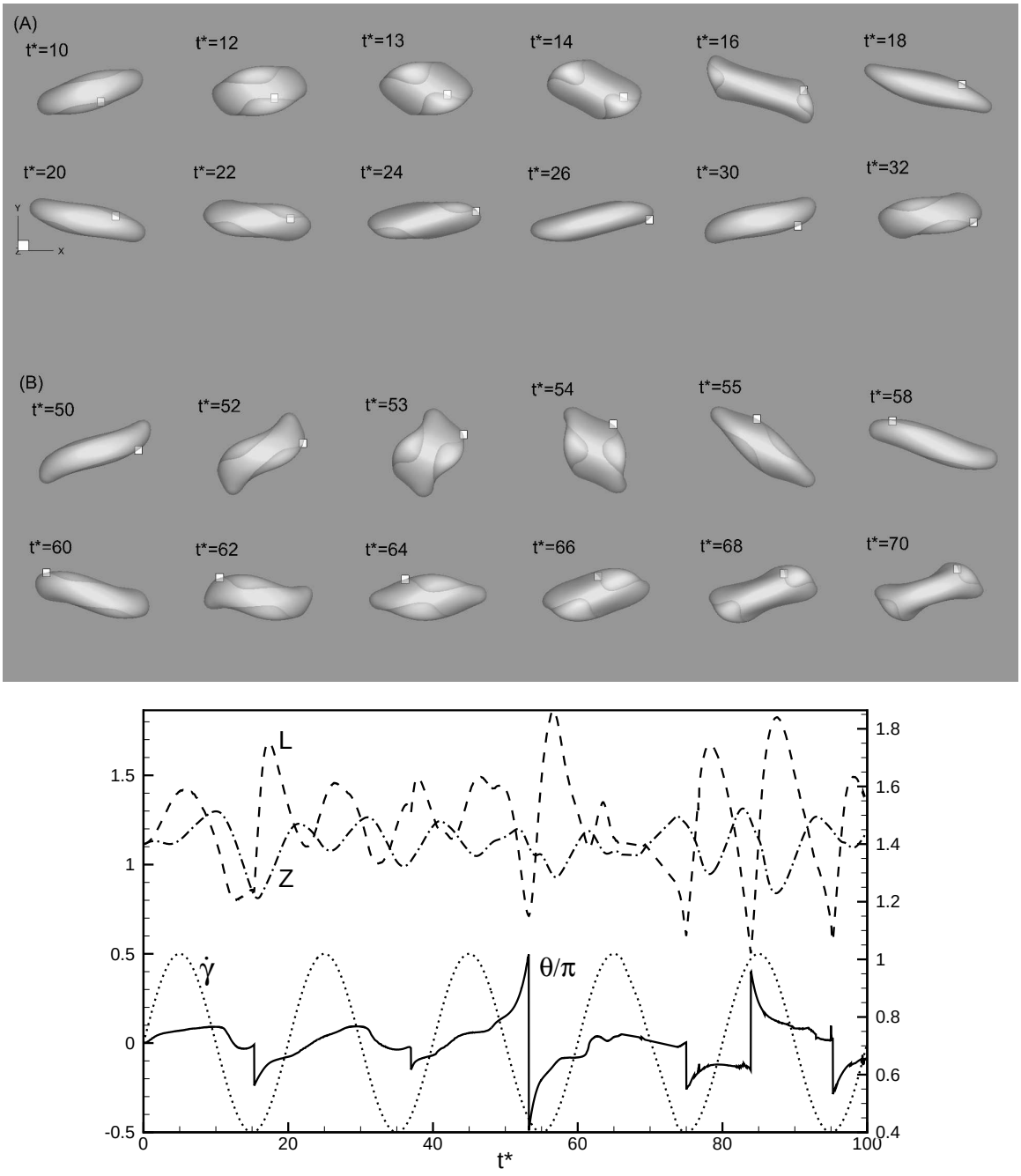

Figure 3.35: RBC dynamics in zero-mean oscillating shear flow at intermediate shear rate and oscillation period. Top: snapshots for Ca = 0.4, $T^*_{sh} = 20$. Bottom: instantaneous inclination, shear rate, maximum cell length in the shear plane (L) and in the vorticity direction (Z).

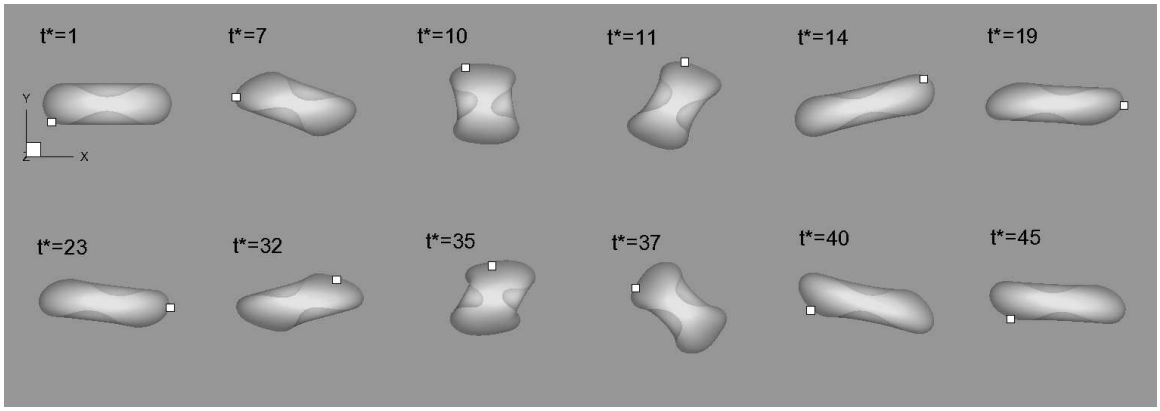

Figure 3.36: Cell dynamics at physiological value of $\lambda = 5$. Ca $= 0.4$, $T^*sh = 45$.

Chapter 4

Summary

4.1 Summary

We presented a 3D numerical study on the dynamics of deformable capsules in oscillating shear flow. In the present work, we mainly focused on the scenario when the internal and external fluids have the same dynamic viscosity, and the amplitude of the shear flow is zero. A detailed analysis of the capsule dynamics obtained from our direct simulaiton is presented under this condition. For the purpose of completeness, we also presented some preliminary results on the dynamics of a red blood cells in zero-mean shear flow. It appears that the analysis of the red blood cell dynamics is more complex due to its biconcave resting shape. Further, we presented some preliminary results on the effect of internal to external viscosity ratio, and the finite-mean shear flow. Detailed investigations of these topics are left for the future.

On the dynamics of capsules under zero-mean shear, and identical internal and external fluid viscosities, which is the main focus of this thesis, our findings can be summarized as follows.

1. For spherical resting shapes, we find identical deformation response during

positive and negative vorticity. We also find that the average deformation increases with increasing flow oscillation period reaching an asymptote that is less than the deformation that would occur in a steady shear flow corresponding to the mean shear rate. The phase lag increases with increasing Ca and increasing shear frequency as in [48].

2. The deformation response becomes unequal and shows complex behavior for nonspherical capsules due to the coupling with the natural shape oscillation. The average elongation is higher in the retarding phase than in the accelerating phase although the membrane viscosity is neglected.

3. Unlike in a steady shear flow, we find that the capsules swing clockwise and counter-clockwise in response to the altering flow direction at both high and low values of shear rate amplitude, but tumble continuously in one direction at intermediate values although the time-average vorticity is zero. Such a tumbling dynamics is accompanied by a continuous tank-treading motion of the membrane in the opposite direction.

4. We obtained phase diagram that shows existence of two critical shear rates and two oscillation frequencies. The continuous/unidirectional tumbling motion occurs in the intermediate range, and the clockwise/counter-clockwise swinging motion occurs otherwise. The swinging motion at low Ca is TB-based, while that at high Ca is TT-based [48].

5. As an evidence of 'chaotic' motion, we find that the dynamics is highly sensitive to the initial condition. A swinging is generally observed when the

capsule is released aligned with the extensional or compressional axis, and a tumbling is observed otherwise. However, since our simulations are deterministic, we have provided explanations of the dependence on the initial condition by analyzing the synchronized shape and angular oscillation which also illustrate the role of deformation. There are both qualitative agreement and discrepancy between the present study and that of Dupire et al. [1], and Noguchi [48] as discussed before. We are unable to confirm a nonperiodic motion observed by Dupire et al.. One possible reason is that the physical time simulated is much shorter than that required to confirm such a behavior. The second possible reason is that large deformation may suppress the nonperiodic motion [68]. On the other hand, similar to the findings of [1] and [48], we find that only the CW/CCW oscillatory motion occurs at low shear amplitude, and at low and high shear frequencies, and that the dynamics is sensitive to the initial condition, as an indirect evidence to the chaotic behavior.

For the red blood cells with biconcave resting shapes, the dynamics is, however, more complex. Under the condition of the same internal and external fluid viscosity, we find that the cell always undergoes periodic motion at low shear rates for which deformation is negligible. A periodic motion is also observed for high shear rates and low oscillation periods. However, a non-periodic motion characterized by a combination of swinging and tumbling occurs at intermediate shear rates. In this respect, there is some qualitaitve similarity to the experimental findings of Dupire et al.. When the physiological value of the viscosity

ratio is considered, the periodic motion is recovered due to loss of deformation. Thus, we can conclude that the non-periodic motion observed here is driven by the deformation dynamics of the cell, and would not be present if cell deformation is inhibited.

4.2 Future Work

It is clear from the present thesis that the dynamics of capsules and red blood cells in an oscillating shear flow is significantly complex than its counterpart in a steady shear flow. While a significant progress has been made in the past decades by the cell/vesicle/capsule research community on the understanding of single particle dynamics in steady shear flow, we only started to address the dynamics in oscillating shear flow. Understanding this topic in its fullest depth is beyond the scope of one Master's thesis. In the following we discuss some of the issues that can be further addressed with the present numerical method to improve our understanding of this complex but immensely important branch of science.

First, our model for the cell membrane neglects the membrane viscosity. The presence of viscosity of the membrane introduces a 'memory' effect by which the cell responds on a slower time scale to any change in the flow. Experimental measurment of the membrane viscosity is notoriously difficult, and as such, there is a significant debate in the literature as to the range of values of the membrane viscosity. While artificial capsules and vesicles often lack the membrane viscosity, the red blood cells are known to possess this property. It is important in future

to repeat the direct simulations results presented here with the inclusion of the membrane viscosity in the numerical model, and regenerate the phase diagrams. The membrane viscosity may also suppress the deformation, and hence some of the complex dynamics observed and the chaotic motion suggested here may be absent when the membrane viscosity is included.

Secondly, the dynamics of the red blood cells is not fully addressed here. It appears that the nonperiodic motion similar to that observed in the experiments may be reproducible in the simulations provided that we are able to run for a much longer time. This requires a more robust numerical methodology. Presently, numerical instabilities often develop if simulations are continued beyond a dimensionless time of 100 or so. One way of mitigate the instability is to re-mesh the capsule/cell surface. Our future efforts should be directed along this line.

Thirdly, we addressed the dynamics of only isolated capsule and red blood cell. In other words, we considered a dilute suspension. In reality, the blood is a dense suspension. It is would important, and a very interesting problem, to consider a dense suspension in an oscillating flow, and to extract the viscoelastic behavior of the suspension. The current methodology can be readily extended to consider this problem.

Finally, the physiological blood flow is not a linear shear flow as considered here, rather it is pressure-driven and often deviates from the well-known parabolic Poiseuille flow. In small vessels, flow remains unidirectional but oscillates with time. In large vessels, the oscillations are significant, and the flow reversal can

take place. Future research can investigate how the individual red blood cell, as well as cell suspension behaves under such complex background flow.

References

[1] M. Abkarian J. Dupire and A. Viallat. Chaotic dynamics of red blood cells in a sinusoidal flow", hear induced deformation of microcapsules: shape oscillations and membrane folding.

[2] R.J. Asaro P. Sche Q. Zhu, C. Vera and L.A. Sung. A hybrid model for erythrocyte membrane: A single unit of protein network coupled with lipid bilayer. *Biophysical J.*, **93**:386, 2007.

[3] N. Mohandas and E. Evans. Mechanical properties of the red cell membrane in relation to molecular structure and genetic defects. *Annu. Rev. Biophys. Biomolec. Struct.*, **23**:787, 1994.

[4] H.L. Goldsmith. *Federation Proceedings*, 30:1578, 1971.

[5] H. Goldsmith and J. Marlow. Flow behavior of erythrocytes. i. rotation and deformation in dilute suspensions. *Proc. R. Soc. B*, **182**:351, 1972.

[6] M. Stohr-Liesen T.M. Fischer and H. Schmid-Schonbein. The red cell as a fluid droplet: tank-tread like motion of the human erythrocyte membrane in shear flow. *Science.*, **202**:894, 1978.

[7] R. Tran-Son-Tay. *PhD Thesis.*, 1983. Washington University, St. Louis, MO.

[8] M. Faivre M. Abkarian and A. Viallat. Swinging of red blood cells under shear flow. *Phys. Rev. Lett*, **98**:188302, 2007.

[9] T.M. Fischer. *Biophys. J.*, **93**:2553, 2007.

[10] U. Seifert M. Kraus, W. Wintz and R. Lipowsky. Fluid vesicles in shear flow. *Phys. Rev. Lett.*, **77**(17):3685, 1996.

[11] S. Ramanujan and C. Pozrikidis. Deformation of liquid capsules enclosed by elastic membranes in simple shear flow: large deformations and the ect of fluid viscosities. *J. Fluid Mech.*, **361**:117–143, 1998.

[12] M. Husmann H. Rehage and A. Walter. From two-dimensional model networks to microcapsules. *Rheol. Acta*, **41**:292, 2002.

[13] K. Kassner T. Biben and C. Misbah. Phase-field approach to three-dimensional vesicle dynamics. *Phys. Rev. E*, **72**:041921, 2005.

[14] V. Kantsler and V. Steinberg. Orientation and dynamics of a vesicle in tank-treading motion in shear flow. *Phys. Rev. Lett.*, **95**:258101, 2005.

[15] V. Kantsler and V. Steinberg. Transition to tumbling and two regimes of tumbling motion of a vesicle in shear flow. *Phys. Rev. Lett.*, **96**:036001, 2006.

[16] M. Abkarian A. Viallat M.-A. Mader, V. Vitkova and T. Podgorski. Dynamics of viscous vesicles in shear flow. *Eur. Phys. J. E*, **19**:389–397, 2006.

[17] A. Morel E. Lac and D. Barthes-Biesel. Hydrodynamic interaction between two identical capsules in simple shear flow. *J. Fluid Mech.*, **573**:149, 2007.

[18] R. Finken S. Kessler and U. Seifert. Swinging and tumbling of elastic capsules in shear flow. *J. Fluid Mech*, **605**:207, 2008.

[19] S.R. Keller and R. Skalak. Motion of a tank-treading ellipsoidal particle in a shear flow. *J. Fluid Mech.*, **120**:27, 1982.

[20] J.M. Skotheim and T.W. Secomb. Oscillatory dynamics and the tank-treading-to-tumbling transition. *Phys. Rev. Lett.*, **98**:078301, 2007.

[21] D. Barthes-Biesel and J.M. Rallison. The time-dependent deformation of a capsule freely suspended in a linear shear flow. *J. Fluid Mech.*, **113**:251–267, 1981.

[22] T. Podgorski C. Verdier G. Danker, T. Biben and C. Misbah. Dynamics and rheology of a dilute suspension of vesicles: Higher-order theory. *Phys. Rev. E.*, **76**:041905, 2007.

[23] K.S. Turitsyn V.V. Lebedev and S.S. Vergeles. Nearly spherical vesicles in an external flow. *New J. Phys.*, **10**:043044, 2008.

[24] Y.T. Chew Y. Sui, H.T. Low and P. Roy. Tank-treading, swinging, and tumbling of liquid-filled elastic capsules in shear flow. *Phys. Rev. E*, **77**:016310, 2008.

[25] P. Bagchi and R.M. Kalluri. Dynamics of nonspherical capsules in shear flow. *Phys. Rev. E*, **80**:016397, 2009.

[26] P. Roy Y.P. Cheng Y. Sui, Y.T. Chew and H.T. Low. Dynamic motion of red blood cells in simple shear flow. *Phys. Fluids*, **20**:112106, 2008.

[27] H. Noguchi and G. Gompper. Swinging and tumbling of fluid vesicles in shear flow. *Phys. Rev. Lett.*, **98**:128103, 2007.

[28] K.S. Chang and W.L. Olbricht. Experimental studies of the deformation of a synthetic capsule in extensional flow. *J. Fluid Mech.*, **250**:587–608, 1993.

[29] Colle-Paillot F. Risso, F. and M. Zagzoule. Experimental investigation of a bioartificial capsule flowing in a narrow tube. *J. Fluid Mech.*, **547**:149–174, 2006.

[30] D. Barthes-Biesel. Motion of a spherial microcapsule freely suspended in a linear shear flow. *J. Fluid Mech.*, **100**:831–853, 1980.

[31] D. Barthes-Biesel and H. Sgaier. Role of membrane viscosity in the orientation and deformation of a spherical capsule suspended in shear flow. *J. Fluid Mech.*, **160**:119–135, 1985.

[32] D. Barthes-Biesel. Role of interfacial properties on the motion and deformation of capsules in shear flow. *Physica A*, **172**:103–124, 1991.

[33] D. Barthes-Biesel X. Li and A. Helmy. Large deformations and burst of a capsule freely suspended in an elongational flow. *J. Fluid Mech.*, **187**:179–196, 1988.

[34] A. Leyrat-Maurin and D. Barthes-Biesel. Motion of a deformable capsule through a hyperbolic constriction. *J. Fluid Mech.*, **279**:135–163, 1994.

[35] C. Queguiner and D. Barthes-Biesel. Axisymmetric motion of capsules through cylindrical channels. *J. Fluid Mech.*, **348**:349–379, 1997.

[36] C. Pozrikidis. Finite deformation of liquid capsules enclosed by elastic membranes in simple shear flow. *Journal of Fluid Mechanics*, **297**:123–152, 1995.

[37] C. Pozrikidis. Effect of membrane bending stiffness on the deformation of capsules in simple shear flow. *J. Fluid Mech.*, **440**:269–291, 2001.

[38] S. Kwak and C. Pozrikidis. Effect of membrane bending stiffness on the axisymmetric deformation of capsules in uniaxial extensional flow. *Physics of Fluids*, **13**:1234–1244, 2001.

[39] N Pelekasis A. Diaz and D. Barthes-Biesel. Transient response of a capsule subjected to verying flow conditions: Effect of internal fluid viscosity and membrane elasticity. *Physics of Fluids*, **12**:948–958, 2000.

[40] D. Barthes-Biesel A. Diaz and N Pelekasis. Effect of membrane viscosity on the dynamic response of an axisymmetric capsule. *Physics of Fluids*, **13**:3835–3839, 2001.

[41] A. Diaz D. Barthes-Biesel and E. Dhenin. Effect of constitutive laws for two-dimensional membranes on flow-induced capsule deformation. *J. Fluid Mech.*, **460**:211–222, 2002.

[42] N.A. Pelekasis & J. Tsamopoulos E. Lac, D. Barthes-Biesel. Spherical capsules in three-dimensional unbounded stokes flows: effect of the membrane constitutive law and onset of buckling. *J. Fluid Mech.*, **516**:303, 2004.

[43] E. Lac and D. Barthes-Biesel. Deformation of a capsule in simple shear flow: Effect of membrane prestress. *Physics of Fluids*, **17**:072105, 2005.

[44] C. D. Eggleton and A. S. Popel. Large deformation of red blood cell ghosts in a simple shear flow. *Physics of Fluids*, **10**(8):1834–1845, 1998.

[45] R.M. Berne and M.N. Levy. Cardiovascular physiology. *Mosby*, 8th ed., 2001.

[46] N. Maeda K. Tsunekawa T. Nakajima, K. Kon and T. Shiga. Deformation response of red blood cells in oscillatory shear flow. *Am. J. Physiol. Heart Circ. Physiol.*, **259**:H1071, 1990.

[47] R. Finken S. Kessler and U. Seifert. Elastic capsules in shear flow: Analytical solutions for constant and time-dependent shear rates. *Euro. Phys. J. E*, **29**:399, 2009.

[48] H. Noguchi. Dynamic modes of red blood cells in oscillatory shear flow. *Phys. Rev. E*, **81**:061920, 2010.

[49] P. Bagchi and R.M. Kalluri. Dynamic rheology of a dilute suspension of elastic capsules: Effect of capsule tank-treading, swinging, and tumbling. *J. Fluid Mech*, **669**:498, 2011.

[50] S. Kessler R. Finken and U. Seifert. Micro-capsules in shear flow. *J.Phys.: Condens. Matter*, **23**:184113, 2011.

[51] A. Esmaeeli N. Al-Rawahi W. Tauber J. Han S. Nas G. Tryggvason, B. Bunner and Y. Jan. A front tracking method for the computations of multiphase flow. *J. Comp. Phys*, **169**:708, 2001.

[52] P.R. Zarda R. Skalak, A. Tozeren and S. Chien. Strain energy function of red blood cell membrane. *Biophys J.*, **13**:245, 1973.

[53] O.-Y. Zhong-can and W. Helfrich. Bending energy of vesicle membranes: General expressions for the first, second, and third variation of the shape energy and applications to spheres and cylinders. *Phys. Rev. A.*, **39**:5280, 1989.

[54] C.S. Peskin. Numerical analysis of blood flow in the heart. *J. Comput. Phys.*, **25**:220–233, 1977.

[55] S.O. Unverdi and G. Tryggvason. A front-tracking method for viscous, incompressible, multi-fluid flows. *Journal of Computational Physics*, **100**:25–37, 1992.

[56] S. Shrivastava and J. Tang. Large deformation finite element analysis of non-linear viscoelastic membranes with reference to thermoforming. *J. Strain Anal*, **28**:31, 1993.

[57] D. Giorgi G. Patane-& M. Spagnuolo M. Reuter, S. Biasotti. Discrete laplace-beltrami operators for shape analysis and segmentation. *Comput. Graphics*, **33**:381, 2009.

[58] E.A. Evans. Bending elastic modulus of red blood cell membrane derived from buckling instability in micropipette aspiration tests. *Biophys J.*, **43**:27, 1983.

[59] E. Sackmann M. Peterson, H. Strey. Theoretical and phase contrast microscopic eigenmode analysis of erythrocyte flicker: Amplitudes. *J. Phys II France*, **2**:1273, 1992.

[60] & R.E. Waugh W.C. Hwang. Energy of dissociation of lipid bilayer from the membrane skeleton of red blood cells. *Biophys J.*, **72**:2669, 1997.

[61] E. Ben-Jacob R. Korenstein L. Scheffer, A. Bitler. Atomic force pulling: probing the local elasticity of the cell membrane. *Eur Biophys J.*, **30**:83, 2001.

[62] N. Mohandas-K. Parker J. Sleep J. Evans, W. Gratzer. Fluctuations of the red blood cell membrane: relation to mechanical properties and lack of atp dependence. *Biophys J.*, **94**:4134, 2008.

[63] A. Richert-F. Gallet S. Henon, G. Lenormand. A new determination of the shear modulus of the human erythrocyte membrane using optical tweezers. *Biophys J.*, **76**:1145, 1999.

[64] Y.C. Fung. Biomechanics: Mechanical properties of living tissues. *Springer-Verlag, NY*, 1993.

[65] S.K. Doddi and P. Bagchi. Three-dimensional computational modeling of multiple deformable cells flowing in microvessels. *Phys. Rev. E*, **79**:046318, 2009.

[66] S.K. Doddi and P. Bagchi. Lateral migration of a capsule in a plane poiseuille flow in a channel. *Intl. J. Multiphase Flow*, **34**:966, 2008.

[67] & K. Sarkar X. Li. Front-tracking simulation of deformation and buckling instability of a liquid capsule enclosed by an elastic membrane. *J. Comp. Phys.*, **227**:4998, 2008.

[68] G. Danker P. M. Vlahovska, Y.-n.Young and C. Misbah. Dynamics of a non-spherical microcapsule with incompressible interface in a shear flow. *J. Fluid Mech.*, 2011. to appear.

[69] Alireza Z.K. Yazdani and P. Bagchi. Phase diagram and breathing dynamics of a single red blood cell and a biconcave capsule in dilute shear flow. *Physical Review E*, **84**:026314, 2011.